NASA/CR - 97 - 207500

U. S. PARTICIPATION IN THE GOME AND SCIAMACHY PROJECTS

NASA Grant NAGW-2541

Final Report

For the period 1 April 1991 through 30 September 1997

Principal Investigator:

K.V. Chance

Smithsonian Astrophysical Observatory

March 1998

Prepared for
National Aeronautics and Space Administration

Smithsonian Institution
Astrophysical Observatory
Cambridge, Massachusetts 02138

The Smithsonian Astrophysical Observatory
is a member of the
Harvard-Smithsonian Center for Astrophysics

The NASA Technical Officer for this grant is Dr. Jack Kaye
Code SED, NASA/HDQ

Final Report

NASA Grant NAGW-2541
U. S. Participation in the GOME and SCIAMACHY Projects

Principal Investigator:
K.V. Chance
Smithsonian Astrophysical Observatory
Cambridge, MA 02138

Co-Investigators:
J.C. Geary, R.J.D. Spurr
Smithsonian Astrophysical Observatory
Cambridge, MA 02138

Introduction

This report summarizes research done under NASA Grant NAGW-2541 through September 30, 1997. The research performed under this grant includes development and maintenance of scientific software for the GOME retrieval algorithms, consultation on operational software development for GOME, sensitivity and instrument studies to define GOME and SCIAMACHY instruments, consultation on optical and detector issues for both GOME and SCIAMACHY, consultation and development for SCIAMACHY near-real-time (NRT) and off-line (OL) data products, and development of infrared line-by-line atmospheric modeling and retrieval capability for SCIAMACHY. The European Space Agency selected the SAO to participate in GOME validation and science studies, part of the overall ERS AO. This provided access to all GOME data; The SAO activities that are carried out as a result of selection by ESA were funded by the present grant. The Global Ozone Monitoring Experiment was successfully launched on the ERS-2 satellite on April 20, 1995, and remains working in normal fashion. SCIAMACHY is currently scheduled for launch in early 2000. The first two European ozone monitoring instruments (OMI), to fly on the Metop series of operational meteorological satellites being planned by Eumetsat, have been selected to be GOME-type instruments (the first, in fact, will be the refurbished GOME flight spare). K. Chance is the U.S. member of the OMI Users Advisory Group.

SAO performed the initial sensitivity studies for GOME and SCIAMACHY that determined their capability to measure gases including:

- From GOME - O_3 (including profiles and tropospheric ozone from the GOME nadir measurements), O_2, O_2-O_2 (the collision complex), NO_2, H_2CO, H_2O, SO_2, NO_3, ClO, OClO, and BrO (global distributions).
- From SCIAMACHY - the species measured by GOME plus, at least, CO, CO_2, N_2O, and CH_4. Additional profiles will be available from limb and occultation viewing geometries.

All of the measurements we proposed for GOME based on the SAO sensitivity studies have now been measured except for NO_3 (due to the limited amount of eclipse mode data). The ClO measurements are currently at a rudimentary state, but will be improved substantially as radiative transfer studies improve (detectability of ClO under ozone hole conditions has been demonstrated and the instrument signal-to-noise is adequate for quite precise measurements). Thus we are quite confident that SCIAMACHY will provide the measurements as we have predicted, including the important tropospheric species CO, N_2O, and CH_4.

The results of the various radiative transfer-related studies funded by this grant, coupled with development of advanced fitting procedures, currently permit SAO to make the most precise and accurate determinations yet of trace gas concentrations from GOME data. Figure 1 shows an example of a single BrO measurement from GOME, coincident with the SAO FIRS-2 balloon-based measurements (which include HBr and HOBr, as well as some 20 additional atmospheric gases). Such measurements are determinable from all GOME spectra, some 30,000 per day since mid-1995 through the present. Figure 2 shows an example of BrO determined from one complete orbit, on September 15, 1996. This orbit, which includes an episode of substantial enhancement of BrO in the Antarctic spring, has been selected for the BrO intercomparison being carried out by the various GOME researchers.

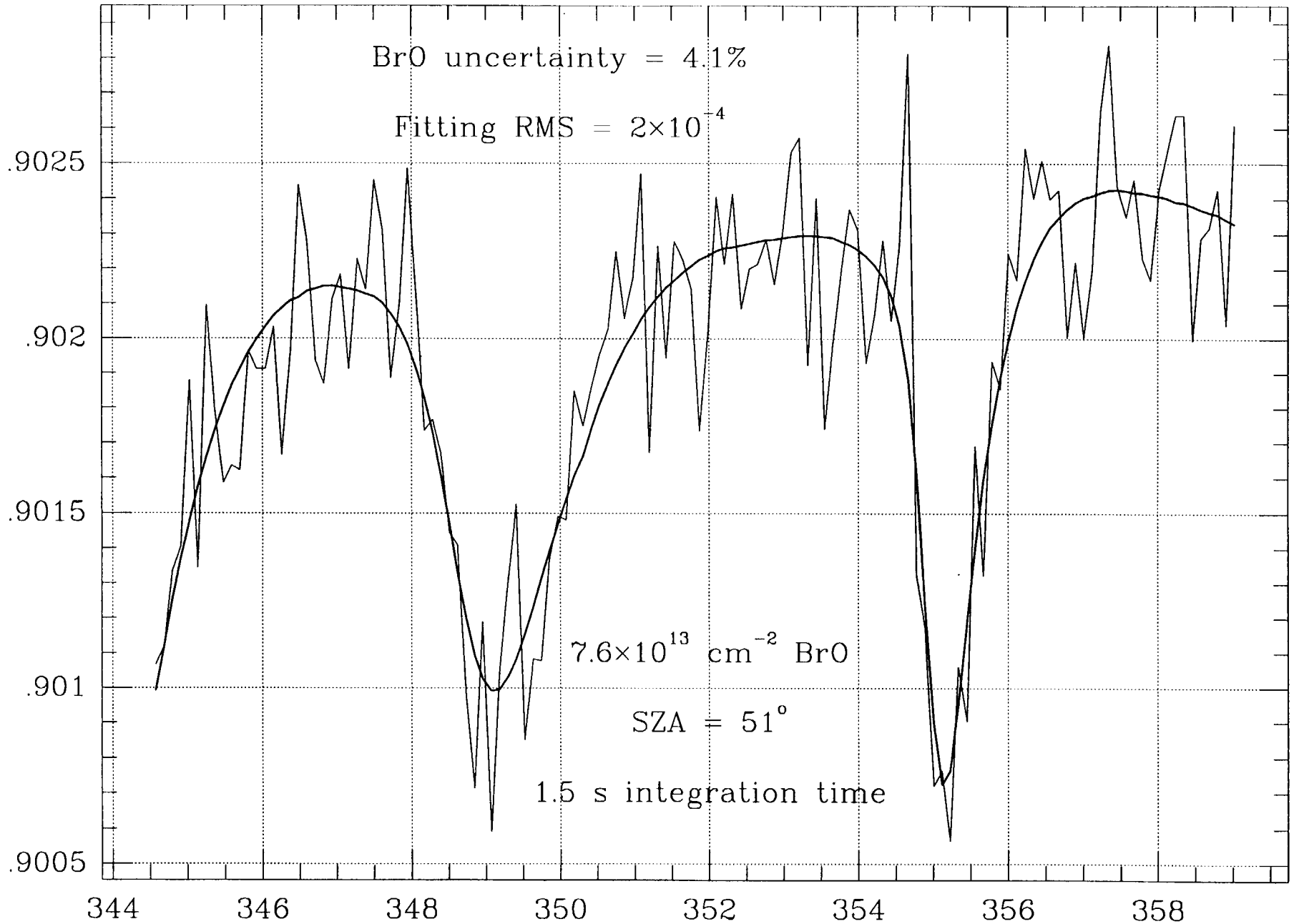

Figure 1. GOME BrO for overflight of FIRS-2 1997 Alaska flight

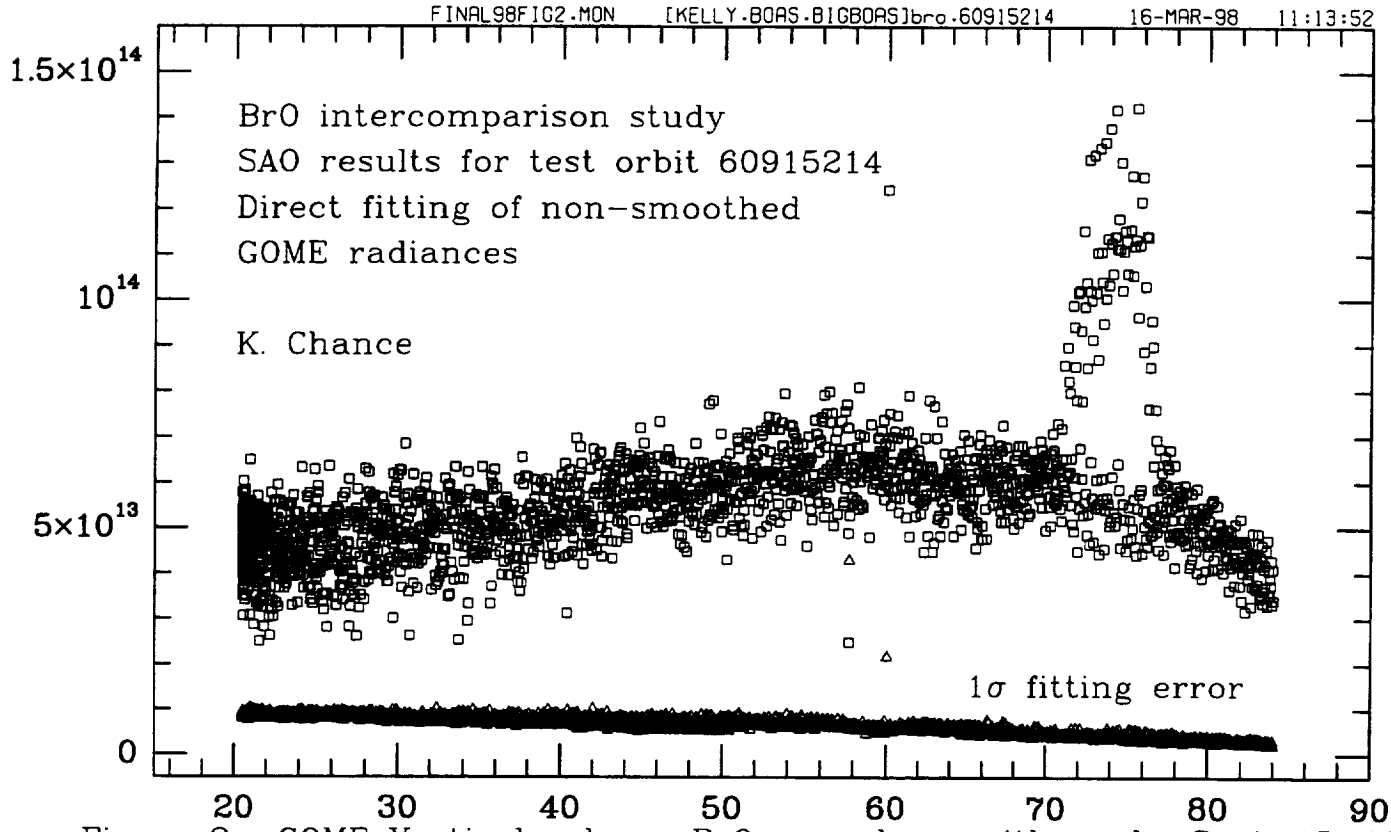

Figure 2a. GOME Vertical column BrO vs. solar zenith angle: Sept. 15, 1996

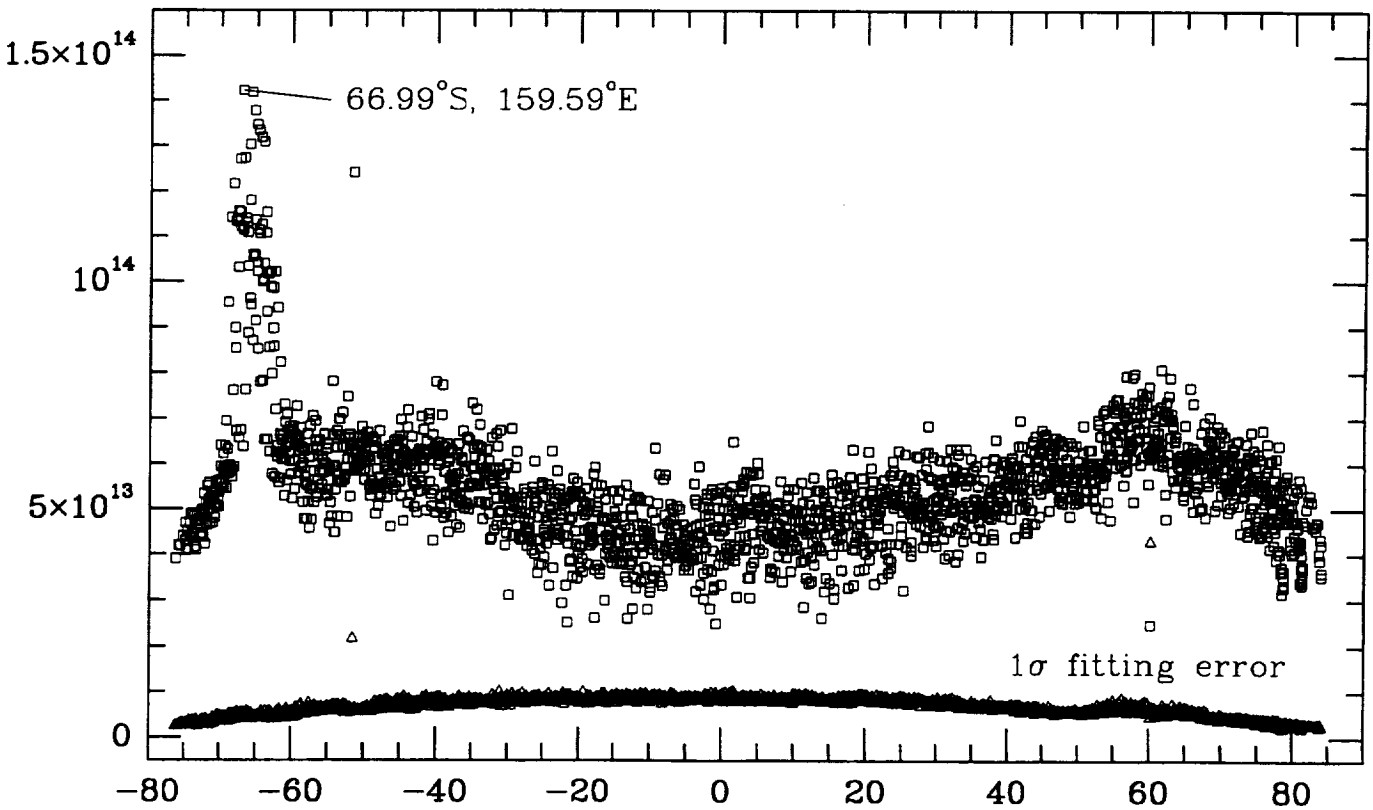

Figure 2b. GOME Vertical column BrO vs. latitude: Sept. 15, 1996

GOME and SCIAMACHY Studies Through September 1997

The research at the SAO for the GOME and SCIAMACHY projects has included development and maintenance of scientific software for the GOME retrieval algorithms, advising and assisting in the development of GOME operational software, participation in GOME validation and science studies, sensitivity and instrument studies to help finalize the definition of both instruments, completion of the SCIAMACHY study to produce the Scientific Requirements Document for Data and Algorithm Development, development of scientific software for GOME and SCIAMACHY retrievals, and consultation on the development NRT and OL operational data processing and data products.

GOME

The development of the scientific code that implements the GOME retrieval algorithms and their realization as the first release of operational processing code was finished. Following the end of the GOME commissioning phase (March 1996) and the initial validation of the operational retrieval algorithms, the first official release of GOME level 2 products (total ozone columns) took place in July 1996. GOME level 1 data products (radiance spectra) were released in late 1997. SAO GOME studies include the following items:

- Guiding the development of GOME level 0-1 and 1-2 operational software through extensive collaboration with the DLR.
- Cloud studies, including investigation of fitting schemes and analysis of uncertainties due to various error sources, including line parameters of O_2. These resulted in production of the prototype operational algorithm for GOME cloud correction which has now been implemented in the level 1 operational software.
- Development and incremental improvement of the GOMEware scientific software for thorough scientific testing of GOME algorithms, including those that have been implemented initially in the operational framework at DLR. The activity was centered at SAO, but included collaboration with a number of the European institutions involved in GOME.
- Participation in GOME validation and scientific studies. Note that the validation studies include ozone profiles and tropospheric ozone abundances, which are being produced as off-line scientific products.

- Development of fitting methods for direct (non-DOAS) fitting of GOME radiances. This now provides the best available global measurements of BrO from GOME (by an order of magnitude) and will provide substantially enhanced SO_2 measurements (pollution and, possibly, background levels) in the near future. It has also permitted SAO to make the first and, to date, only detections of ClO from GOME measurements. This method allows single, non-smoothed GOME radiance spectra to be fitted to RMS levels of, typically, 5×10^{-4}, in optical depth units.

- Collaboration on the development of the DOAS method as the operational procedure for GOME level 1-2 processing to produce O_3 columns from GOME. This collaboration includes code development, measurement window selection, and a number of related issues.

- Changes to operational code for GOME level 0-2 processing, to adjust for post launch conditions and to correct initial deficiencies.

- Participation in GOMEtran finite-difference forward model development, in collaboration with the University of Bremen.

- Spectroscopic and aerosol database development, including the production of an improved database of molecular parameters for the visible O_2 *A* band, and improved wavelength calibration of the BrO spectrum.

- Radiative transfer studies related to wavelength calibration and spatial and spectral aliasing, including development of an improved solar reference spectrum for wavelength-specific applications.

- Improved determination of the wavelength-dependent Rayleigh scattering cross section.

- Improved molecular parameters for the Ring effect through molecular physics studies employing the best currently available molecular data; improved atmospheric cross sections describing the Ring effect (the last three items are included in "Ring Effect Studies: Rayleigh Scattering, Including Molecular Parameters for Rotational Raman Scattering, and the Fraunhofer Spectrum," Chance and Spurr, 1997.

- Improved wavelength calibration of GOME irradiance and radiance spectra, through cross-correlation and nonlinear least-squares techniques. For example, in the BrO fitting region, we routinely perform wavelength calibrations of GOME data to substantially better than 0.001 nm in absolute vacuum wavelength.

- Participation in the ESA cloud and aerosol *ad hoc* study group to produce cloud and aerosol data products from GOME.

- Guiding and advising work on operational processor updates and reprocessing of GOME data. This includes, for example, the future use of the TOMS Version 7 ozone climatology in GOME data processing.
- Participation in the GOME Scientific Advisory Group (GSAG) and chairing the data and algorithm subgroup (GDAG).

SCIAMACHY

SCIAMACHY is a joint German/Netherlands/Belgian program, with scientific participation from other European countries and, in the U.S., the SAO. It is included for launch aboard the ESA Envisat-1, currently planned for early 2000.

The SCIAMACHY Science Advisory Group (SSAG) was formed, including K. Chance of the SAO as a U.S. member and chair of the scientific working subgroup for Algorithm Development and Data Usage (SADDU), J. Geary of the SAO as a U.S. member and advisor on instrument and detector issues, and R. Spurr as the third U.S. member and organizer and chair of the GOME/SCIAMACHY Scientific Working Sessions. SAO SCIAMACHY studies under the present grant include the following items:

- Participation in the definition of SCIAMACHY instrument, including: consultation on SCIAMACHY detector, cooling and instrumentation issues; finalization of the SCIAMACHY band definitions and detector selection criteria; synthetic retrieval studies for atmospheric spectroscopy in the infrared contributing to these definitions.
- Chairing the scientific working subgroup for Algorithm Development and Data Usage; Organizing and chairing the joint GOME/SCIAMACHY Scientific Working Sessions. There have been six of the to date. The seventh will be held in April 1998, and in early 1999 there will be an ESA-sponsored atmospheric measurements conference that is an outgrowth of these sessions.
- Heading the development, compilation, and production of the Scientific Requirements Document for SCIAMACHY Data and Algorithm Development.
- Contributions to the SCIAMACHY Instrument Requirements Document
- Contributions to the SCIAMACHY Scientific Requirements Document

- Radiative transfer studies, including development of line-by-line modeling capability for the infrared and visible and ray tracing for the limb and occultation measurement geometries. The issue of properly combining limb and nadir measurements is being addressed by the SADDU, in conjunction with the development of the SCIAMACHY observational strategy.
- Development of the Basic Infrared Absorption Spectroscopy (BIAS) technique for application to the SCIAMACHY infrared channels.
- Extension of GOME software development to SCIAMACHY. Existing GOME databases are extended in wavelength where appropriate to near infra-red. Line-by-line spectroscopic data sets have been compiled for SCIAMACHY (infrared) channels 7 and 8.
- Participation in the definition of Near-Real-Time (NRT) and Off-line (OL) data products for SCIAMACHY, including close collaboration with the DLR in the generation of SCIAMACHY NRT specification documentation.

Publications from this Research Program

1990 SCIAMACHY Instrument Design, A.P.H. Goede, H.J.M. Aarts, C. van Baren, J.P. Burrows, K.V. Chance, R. Hoekstra, E. Hölzle, W. Pitz, W. Schneider, C. Smorenberg, H. Visser, and J. de Vries, *COSPAR XXVIII Plenary meeting,* paper S.1.6.12,

1990 GOME and SCIAMACHY: Remote Sensing of Stratospheric and Tropospheric Trace Gases, J.P. Burrows, W. Schneider and K.V. Chance, *CEC Air Pollution Report 34: Polar Stratospheric Ozone. Proceedings of the First European Workshop,* ed. J. A. Pyle and N. R. P. Harris, 99-102, ISBN2-87263-060-0.

1990 Database Needs for UV/Visible Spectroscopy, K.V. Chance, J.P. Burrows, R. Meller, G.K. Moortgat, D. Perner and W. Schneider, Paper 6.8, pp. 186-194, Proceedings of the 1990 Atmospheric Spectroscopy Applications Workshop, Moscow, U.S.S.R., ed. A. Barbe, Yu.N. Ponomarev and R. Zander, Published by Institute of Atmospheric Optics, Tomsk, U.S.S.R., Zak. 151-100-90.

1990 Space Borne Remote Sensing of Trace Gases by Passive DOAS Sounding, K.V. Chance, J.P. Burrows, W. Schneider, and D. Perner, Chemistry of the Global Atmosphere meeting, Chamrousse, France.

1990 Atmospheric Remote Sensing with SCIAMACHY, J.P. Burrows, W. Schneider, J.C. Geary, K.V. Chance, A.P.H. Goede, H.J.M. Aarts, J. de Vries, C. Smorenburg, and H. Visser,

Digest of Topical Meeting on Optical Remote Sensing of the Atmosphere, 1990 (Optical Society of America, Washington, D.C.), Vol. 4, pp 71-74.

1991 Retrieval and Molecule Sensitivity Studies for the Global Ozone Monitoring Experiment and the SCanning Imaging Absorption spectroMeter for Atmospheric CHartographY, K.V. Chance, J.P. Burrows, and W. Schneider, *Proc. S.P.I.E., Remote Sensing of Atmospheric Chemistry, 1491,* 151-165.

1991 Scanning Imaging Absorption Spectrometer for Atmospheric ChartographY, J.P. Burrows and K.V. Chance, *Proc. S.P.I.E., Future European and Japanese Remote Sensing Sensors and Programs, 1490* 146-154.

1992 SCIAMACHY and GOME: The Scientific Objectives, J.P. Burrows and K.V. Chance, *S.P.I.E. Meeting on Optical Methods in Atmospheric Chemistry,* Berlin, Germany.

1992 GOME Instrument Simulation, A.P.H. Goede, C.J.Th. Gunsing, T.M. Kamperman, J. de Vries, R.J. Spurr, J.P. Burrows and K. Chance, *S.P.I.E. Meeting on Optical Methods in Atmospheric Chemistry,* Berlin, Germany.

1992 Ozone Profile Retrievals from the ESA GOME Instrument, R. Munro, B.J. Kerridge, J.P. Burrows, and K. Chance, *1992 Quadrennial Ozone Symposium.*

1992 A Study of the Accuracy of Atmospheric Trace Gas Vertical Profile Retrieval from Satellite-based Occultation Measurements, J.P. Burrows, V.V. Rozanov, Yu.M. Timofeyev, A.V. Polyakov, R.J.D. Spurr and K.V. Chance, *Proceedings of the 1992 International Radiation Symposium*, Tallinn, Estonia.

1993 *Global Ozone Monitoring Experiment Interim Science Report*, J.P. Burrows, K.V. Chance, A.P.H. Goede, R. Guzzi, B.J. Kerridge, C. Muller, D. Perner, U. Platt, J.-P. Pommereau, W. Schneider, R.J. Spurr, and H. van der Woerd, ed. T. D. Guyenne and C. Readings, Report ESA SP-1151, ESA Publications Division, ESTEC, Noordwijk, The Netherlands, ISBN 92-9092-041-6.

1994 Analysis of Cloud-Top Height and Cloud Coverage from Satellites Using the O_2 *A* and *B* Bands, A. Kuze and K.V. Chance, *Journal of Geophysical Research 99,* 14,481-14,491.

1996 O_2 *A* Band Studies for Cloud Detection and Algorithm Improvement, K. Chance, *Proceedings of the GOME Geophysical Validation Campaign*, 65-68, European Space Agency Publication WPP-108.

1996 Ring Effect Studies: Rayleigh Scattering, Including Molecular Parameters for Rotational Raman Scattering, and the Fraunhofer Spectrum, K. Chance and R.J.D. Spurr, *Pro-*

ceedings of the GOME Geophysical Validation Campaign, 69-74, European Space Agency Publication WPP-108.

1996 GOME Calibration and Validation Using Backscatter UV Techniques, E. Hilsenrath, J. Gleason, S. Janz, X-y Gu, R.P. Cebula, K. Chance, and R. Hoekstra, *Proceedings of the GOME Geophysical Validation Campaign*, 85-91, European Space Agency Publication WPP-108.

1996 Global Ozone Monitoring Experiment (GOME): Comparison of Back Scattered Measurements and O_3 DOAS/BUV Retrievals, J.P. Burrows, M. Weber, E. Hilsenrath, J. Gleason, S. Janz, R.P. Cebula, X-Y Gu, and K. Chance, *Proc. XVIII Quadrennial Ozone Symposium.*

1996 Satellite Measurements of Halogen Oxides by the Global Ozone Monitoring Experiment, GOME, on ERS2: Distribution of BrO and Comparison with Groundbased Observations, E. Hegels, P.J. Crutzen, T. Klüpfel, D. Perner, J.P. Burrows, A. Ladstätter-Weißenmayer, M. Eisinger, J. Callies, A. Hahne, K. Chance, U. Platt, and W. Balzer, *Proc. XVIII Quadrennial Ozone Symposium.*

1997 Quantitative Spectroscopy for the Analysis of GOME Data, K. Chance, *Proceedings of the 3rd ERS-2 Symposium, "Space at the Service of Our Environment."*

1997 GOME Wavelength Calibration using Solar and Atmospheric Spectra, C. Caspar and K. Chance, *Proceedings of the 3rd ERS-2 Symposium, "Space at the Service of Our Environment."*

1997 Development of a Prototype Algorithm for the Operational Retrieval of Height-resolved Products from GOME, R. Spurr, *Proceedings of the 3rd ERS-2 Symposium, "Space at the Service of Our Environment."*

1997 GOME Data Processor: The First Operational DOAS-Based Algorithm Applied to Data from a Space-Borne Sensor, E. Hegels, B. Aberle, W. Balzer, K. Kretschel, D. Loyola, E. Mikusch, T. Ruppert, C. Schmid, S. Slijkhuis, R. Spurr, W. Thomas, T. Wieland, and M. Wolfmueller, *Proc. EUROPTO-S.P.I.E. LASER '97, Spectroscopic Atmospheric Monitoring Techniques.*

1997 GOMETRAN: A Radiative Transfer model for the Satellite Project GOME, the Plane-Parallel Version, V. Rozanov, D. Diebel, R.J.D. Spurr, and J.P. Burrows, *Journal of Geophysical Research 102,* 16,683-16,695.

1997 Satellite Measurements of Atmospheric Ozone Profiles, Including Tropospheric Ozone, from UV/Visible Measurements in the Nadir Geometry: A Potential Method to Retrieve

Tropospheric Ozone, K.V. Chance, J.P. Burrows, D. Perner, and W. Schneider, *Journal of Quantitative Spectroscopy and Radiative Transfer 57*, 467-476.

1997 Improvement of the O_2 *A* Band Spectroscopic Database for Satellite-Based Cloud Detection, K. Chance, *Journal of Quantitative Spectroscopy and Radiative Transfer*, 58. 375-378.

1997 Ring Effect Studies: Rayleigh Scattering, Including Molecular Parameters for Rotational Raman Scattering, and the Fraunhofer Spectrum, K. Chance and R.J.D. Spurr, *Applied Optics 36*, 5224-5230.

A Selected Publications from NASA Grant NAGW-2541

Retrieval and Molecule Sensitivity Studies for the Global Ozone Monitoring Experiment and the SCanning Imaging Absorption spectroMeter for Atmospheric CHartographY

Kelly V. Chance

Harvard-Smithsonian Center for Astrophysics
Cambridge, MA 02138

John P. Burrows

Max Planck Institute for Chemistry
Mainz, Germany

Wolfgang Schneider

German Aerospace Research Establishment
Oberpfaffenhofen, Germany

ABSTRACT

The Global Ozone Monitoring Experiment (GOME) and the SCanning Imaging Absorption spectroMeter for Atmospheric CHartographY (SCIAMACHY) are diode array-based spectrometers that will make atmospheric constituent and aerosol measurements from European satellite platforms beginning in the mid 1990's. GOME measures the atmosphere in the UV and visible in nadir scanning, while SCIAMACHY performs a combination of nadir, limb, and occultation measurements in the UV, visible and infrared. We present a summary of the sensitivity studies that have been performed for SCIAMACHY measurements. As the GOME measurement capability is a subset of the SCIAMACHY measurement capability, the nadir, UV and visible portion of the studies shown here apply to GOME as well.

1. INTRODUCTION

SCIAMACHY sensitivity studies include its three measurement geometries: nadir observing, viewing the earth's limb in scattered light, and solar and lunar occultations. In nadir observation alone, profile information is determinable in some cases by differential penetration of backscattered light at different wavelengths (as in TOMS/SBUV), and by the variable temperature structure of some molecular absorptions. Height resolution from nadir measurements is limited to 8-10 km from differential penetration and 3 km in favorable cases using temperature structure. Height resolution in limb viewing is 3 km, limited by the weighting functions for limb scattering and by the spacecraft stability. Height resolution is also 3 km for occultations, limited primarily by the telemetry data rate; 1 km resolution would otherwise be possible. The quantities retrieved from SCIAMACHY measurements include:

Nadir observations: Total column amounts of O_3, O_4, O_2, CO, H_2O, CH_4, CO_2, NO_2, N_2O, HCHO, SO_2, ClO, OClO, and BrO; stratospheric profiles of O_3, CO, H_2O, CH_4, CO_2, N_2O; the column of NO above the ozone layer; tropospheric profiles or columns of O_3, CO, H_2O, CH_4, CO_2, N_2O. Stratospheric profile information, discrimination between stratospheric and tropospheric columns, and, in some cases, tropospheric profile information is derived from the temperature dependences of the absorption features.

0-8194-0600-7/91/$4.00

Limb viewing observations: Stratospheric profiles of O_3 (20-50 km), $O_2(^1\Delta)$ (50 km-90 km), O_2 (20-50+ km), CO (20-35 km), H_2O (20-53 km), CH_4 (20-40 km), CO_2 (20-50+ km), NO (40-140 km), NO_2 (20-40 km), N_2O (20-35 km), BrO (20-25 km under normal conditions; 20-30 km under ozone hole conditions).

Solar/lunar occultations: Stratospheric profiles of O_3 (15-50 km), O_2 (15-50+ km), CO (15-35 km), H_2O (15-53 km), CH_4 (15-40+ km), CO_2 (15-50+ km), NO_2 (15-40 km), N_2O (15-35 km), BrO (15-35 km under normal concentrations). Occultations are more infrequent than limb scattering observations, and are limited to latitudes of 50-80°, but provide the most sensitive and precise profile retrievals.

Tropospheric amounts from limb-nadir subtraction: Tropospheric columns of O_3, CO, H_2O, CH_4, CO_2, NO_2, N_2O.

Clouds and aerosols: SCIAMACHY will obtain aerosol data in occultation, limb-scattering and nadir measurements. Stratospheric aerosol measurements include background aerosol, Junge layer, and polar stratospheric clouds (PSCs); tropospheric aerosols, including clouds, sand winds, and soot from forest fires.

2. MOLECULE SENSITIVITY STUDIES

The sensitivities for retrievals of molecular species concentrations as functions of altitude have been extensively studied, under a wide variety of geographic conditions, in order to accurately gauge the capabilities of the SCIAMACHY instrument. Calculations are performed for all of the SCIAMACHY modes of measurement, including nadir viewing, viewing of the earth's limb in scattered light, and solar and lunar occultations. Note that simultaneous nadir and limb measurements are the normal mode of operation for the majority of dayside portion of each orbit. The calculations include realistic expectations of detector quantum efficiency and noise performance, and the instrument etendue and optical throughput that are derived from the Phase A instrument study.

Retrieval studies for atmospheric molecules are performed using atmospheric concentration profiles from the MPI Mainz global 1-D and 2-D models (C. Brühl, R. Hennig and P. Crutzen, private communication), calculated with clean and polluted air, daytime, conditions. Additional information on nighttime NO_3 comes from Norton and Noxon, 1986.[1] Constant mixing ratios are assumed for CO_2 (340 ppm) and O_2 (20.95%). The simulations assume exposure times of 2 seconds in nadir spectra, 1.5 second in limb spectra and lunar occultations (appropriate to 3 km vertical resolution), and short exposure times in solar occultation, with the constraint that exposures are limited to 10^8 photons/pixel in the most highly illuminated portion of each detector array. Interferences from other absorbing species are included in the studies for each individual molecule. Current studies are limited to a maximum pressure altitude of 60 km because of the limitation of the model calculations to the stratosphere. In practice, profiles for at least O_2, O_3, and CO_2 will extend to higher altitudes.

Spectra for the simulations are taken from the best available sources, including digitally acquired electronic spectra obtained in the laboratory at MPI Mainz. Spectra in the infrared portion are simulated using the 1986 HITRAN line parameter listing.[2]

Calculations of geometries are performed with multilayer, curved-shell models, including refraction, to provide line of sight column densities as functions of temperature, pressure, and altitude. Calculations in the UV and visible parts of the spectrum are made using the AFGL LOWTRAN7 code, including multiple scattering in the nadir and limb geometries. Calculations in the infrared are performed with LOWTRAN7 and with the Smithsonian Astrophysical Observatory line-by-line radiance code.[3] Most calculations are made with the earth's average albedo of 0.3. The effect of surface spectral reflectance on nadir measurements was investigated in more detail, as discussed further below. Lunar occultations are considered for the measurement of NO_3, as discussed in the section for that molecule.

The 2-D model results used in the calculations are for January 1, with global coverage extending from 85°S to 85°N, which samples a very representative set of the earth's atmospheric conditions. Most calculations are done at 35°N, which corresponds to a solar zenith angle of 63.4° for the EPOP 10:00 crossing time. The effect of other solar zenith angles on measurements in the nadir and limb geometries, including measurements in polar regions, was investigated in some detail, as discussed below.

The solar illumination used in these studies is the LOWTRAN7 solar source function. Aerosol and molecular scattering are also from LOWTRAN7. 20 km is taken as a practical lower limit for limb scattering measurements due to confusion by multiple scattering at lower tangent heights. 15 km is taken as the lower limit for occultation measurements because of atmospheric refraction and extinction by aerosols. It is hoped that, in practice, both of these limits can be extended downward. The anticipated EPOP spacecraft jitter of 0.01° corresponds to 0.57 km at the limb, or 8% in airmass. We combine this with the effect of multiple scattering on limb retrievals: Mount *et al.*, measured NO_2 in limb scattering with "negligible" effects due to multiple scattering down to 28 km, with the Solar Mesosphere Explorer satellite, using wavelengths from 430 to 450 nm.[4] SCIAMACHY obtains significant information on NO_2 and O_3 out to 500 nm implying, for Rayleigh scattering varying as $1/\lambda^4$, negligible confusion due to multiple scattering down to 25 km. Thus, we estimate limb measurement errors in precision for profile determinations, discussed further below for individual molecules, of 10% above 25 km and 20% from 20-25 km, unless further limited by the signal to noise ratios of the measurements for such molecules. Determination of stratospheric columns from limb measurements in this wavelength range, particularly for species with concentrations which peak in the stratosphere, will be somewhat more precise, since the multiple scattering predominantly causes smearing of profile information over a scale height about the tangent altitude. Species measurements in the stratosphere using limb scattering at significantly shorter wavelengths will provide only limited profile information due to the larger effects of multiple scattering. Limb measurements at longer wavelengths, particularly in the infrared, are less affected by multiple scattering. Nadir and solar occultation measurement capabilities are calculated using a lower limit of 1% for measurement precision due to the difficulty of making more precise measurements and calibrations. We hope, of course, to be able to achieve higher precision in practice so that this technique will be capable of determining long-term trends in global O_3.

Sensitivity and interference studies for some species to be measured in the infrared are checked by examining a high resolution (0.007 cm^{-1}) solar spectrum from Kitt Peak National Observatory (KPNO), obtained courtesy of D. W. Johnson and G. Stokes. The spectrum was taken as part of the BIC campaign, under clean tropospheric conditions, at 1.1 airmass. Confirmation of O_4 is from a 1.0 airmass high resolution visible solar spectrum from KPNO (courtesy of R. Kurucz).

Figure 1 shows the solar spectrum as measured by SCIAMACHY, including the etendue, optical throughput, detector quantum efficiency (normalized to photons $pixel^{-1}$ s^{-1} for the various detector channels), and the beam dilution (18% of the instrument field of view is filled by the sun when SCIAMACHY views the central part of the solar disk).

A molecule by molecule discussion of the retrieval studies follows. The results are summarized in Figure 2, which shows altitude ranges for profile retrievals, and Table 1. The altitude limits shown here are for retrieval to a 3 km vertical resolution with $\leq$10% uncertainty in the concentrations, excluding uncertainties in cross-sections, for the stratosphere, plus the altitudes over which any tropospheric information can be obtained. These limits are derived from the January 1, 35°N studies, implying a solar zenith angle of 63.4°, as mentioned previously. For most molecules they are valid for solar zenith angles of up to at least 80°. Molecules which may possibly be measured by SCIAMACHY but are not included in the the studies due to the lack of suitable available laboratory spectra include $O(^3P)$, HO_2, and HONO.

2.1 Molecules in the normal atmosphere

O_3 concentrations are retrieved from SCIAMACHY measurements using the ultraviolet (Hartley and

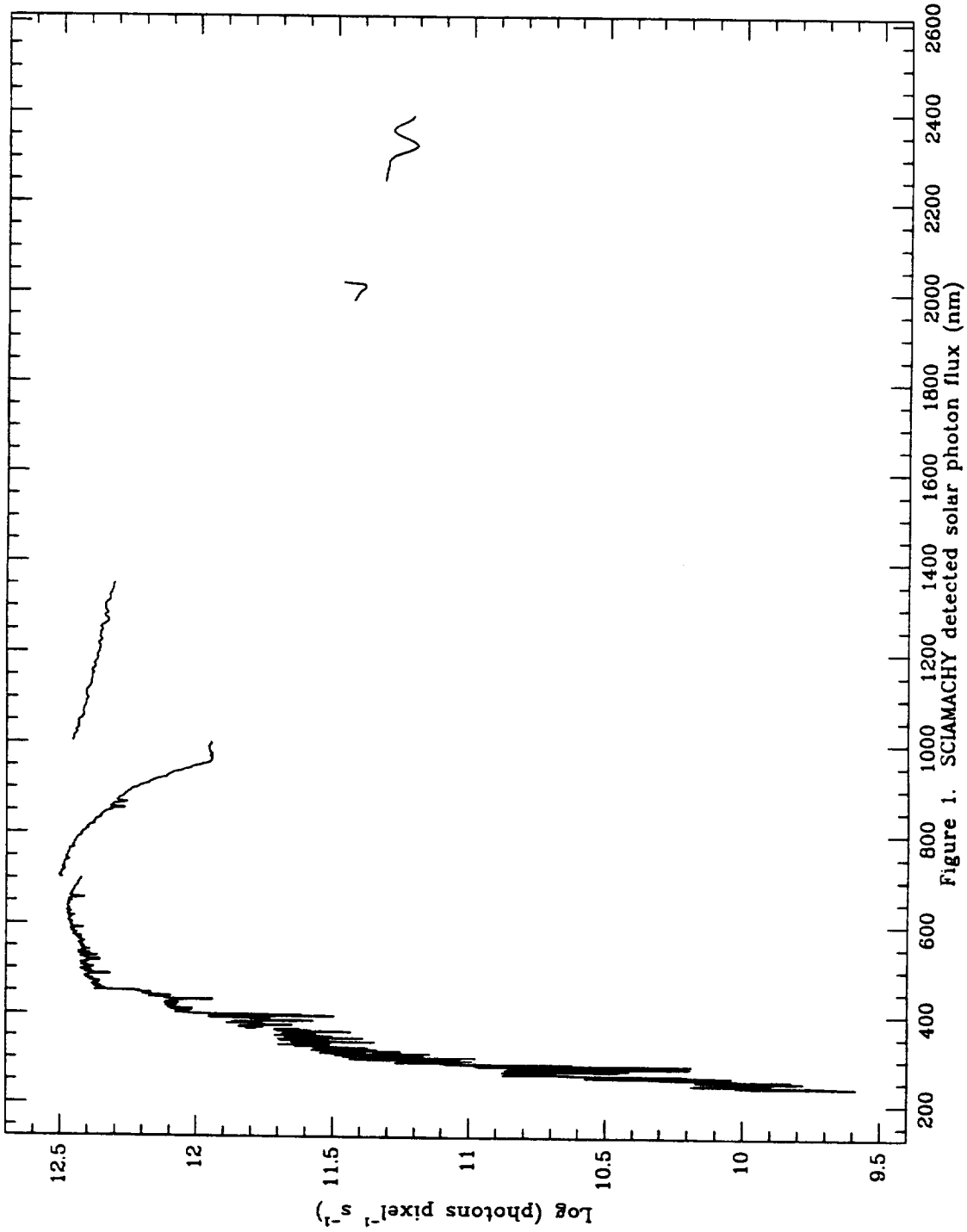

Figure 1. SCIAMACHY detected solar photon flux (nm)

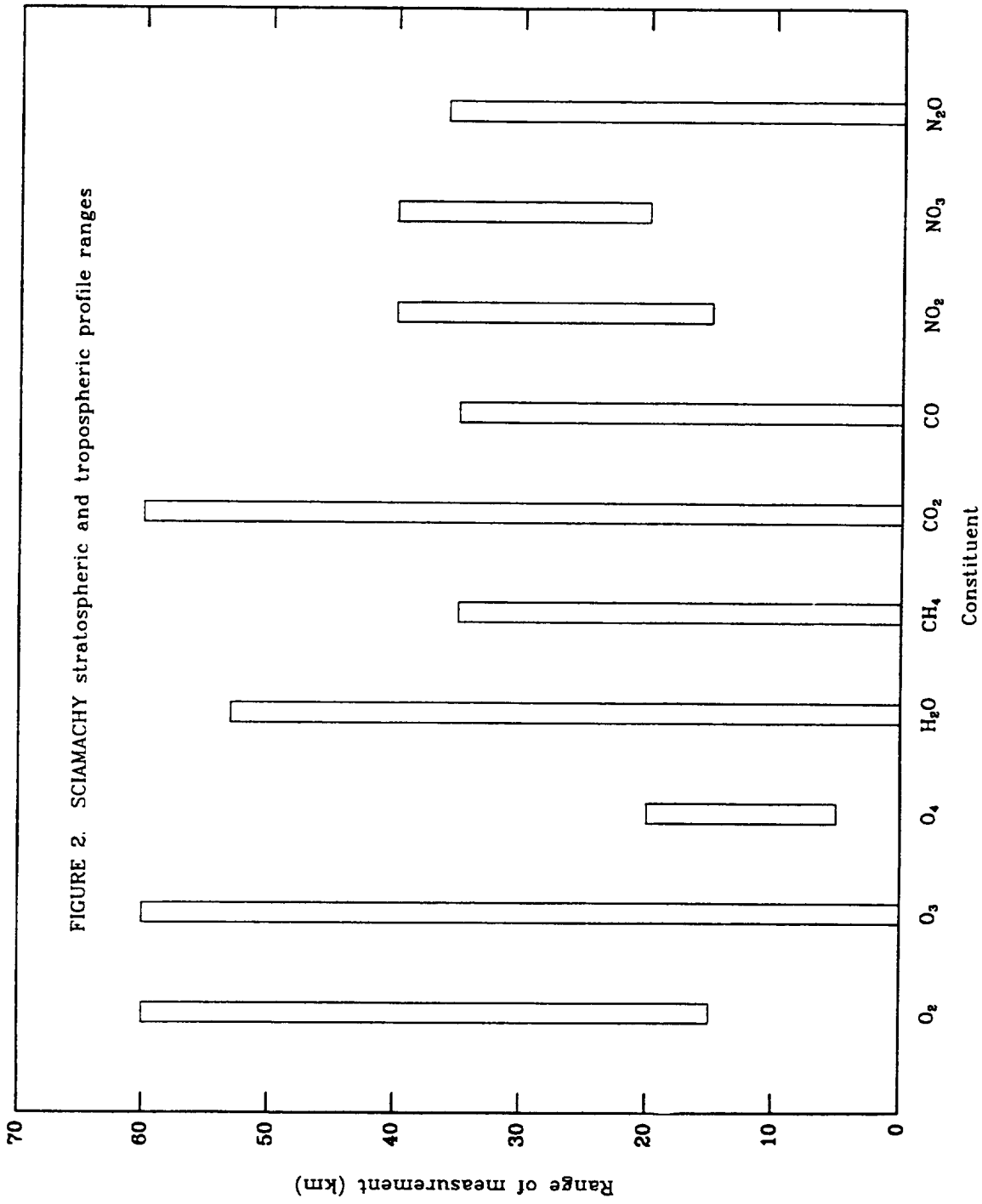

FIGURE 2. SCIAMACHY stratospheric and tropospheric profile ranges

Table 1

Quantities Retrieved from SCIAMACHY Nadir/Limb Observations

Species	Retrievable Quantity*	Wavelength (nm)	Notes/Applications
O_3	Profile (S, T)	255-350, 480-680	
O_2	Profile (S, T)	690, 760	Cloud tops/ boundary layer
$O_2(^1\Delta)$	Profile (S)	1260-1275	Mesospheric O_3
O_4	Column (T)	475, 530, 560, 630	Cloud tops/ boundary layer
H_2O	Profile (S, T)	700-1000, 2250-2390	
CO	Profile (S), Column (T)	2300-2390	Limited tropospheric profile information
CO_2	Profile (S, T)	1980-2020	P, T retrievals
CH_4	Profile (S, T)	2250-2390	
HCHO	Column (T)†	310-360	Biomass burning, tropical vegetation
SO_2	Column (T)†	290-310	Industrial pollution, volcanos
NO	Profile (S)	255-280	Above 40 km in emission
NO_2	Profile (S), Column (T)†	300-600	Lightning, combustion
NO_3	Profile (S)	660-665	Lunar occultation
N_2O	Profile (S), Column (T)	2250-2300	Limited tropospheric profile information
ClO	Column (S)‡	300-310	Polar regions in spring
OClO	Column (S)‡	320-420	Polar regions in spring
BrO	Profile (S)	310-345	

* S = stratosphere; T = troposphere. Mesosphere not included in this table.
†Observable in regions with relatively high concentrations.
‡Observable in perturbed "O_3 hole" regions.

Huggins) bands and the visible (Chappuis) bands. Precise determinations of column O_3 are obtainable from Chappuis band measurements. Measurements of the UV bands, using knowledge of penetration depth as a function of wavelength to obtain stratospheric profile information, has become a standard technique for satellite ozone measurements. This differential penetration is measured using a number of discrete wavelength channels that are much broader than the SCIAMACHY resolution elements. Thus, SCIAMACHY includes this type of measurement as a subset of its O_3 measurements.

SCIAMACHY can also measure ozone profiles in the limb scattering geometry, up to at least 50 km in most geographic locations. Although the signal to noise ratio in these measurements is quite high, the precision of concentration profiles from limb measurements will be limited to ca. 10% above 25 km and 20% from 20-25 km due to the mixing of light from various sources in the multiple scattering process. Stratospheric column O_3 from limb measurements can be determined to 10% since limb measurements extend down to at least 1/2 scale height below the O_3 peak.

A strength of the SCIAMACHY instrument is that it can provide extensive maps of tropospheric ozone. Some determinations of tropospheric O_3 in tropical regions have been made in recent studies by subtracting stratospheric O_3, measured by the SAGE instrument, from TOMS total ozone measurements.[5] SCIAMACHY includes the UV bands used in past and present satellite instruments for measuring O_3, but affords continuous coverage of the region above 240 nm, and at significantly higher resolution. This allows us tremendous leverage in retrieval of tropospheric ozone profiles due to the temperature dependent structure of the Huggins bands.[6,7] The Huggins bands have discrete vibrational structure between 300 and 370 nm, with features having widths significantly less than 1 nm. This is the sharpest vibrational structure of any electronic band of O_3 that has been studied. This structure has strong temperature dependence due to the onset of thermal population of excited vibrational levels in the electronic ground state. It is this temperature dependent structure that provides a spectral signature for tropospheric ozone; its differential character derives from the onset of weaker band absorption between the stronger absorption peaks, which are due to absorption from O_3 (000). One may think of the differential of the O_3 spectrum with temperature as part of a basis set used to match the observed spectrum. Note that tropospheric ozone is significantly warmer than stratospheric ozone at any altitude in the stratosphere where there is significant O_3. Thus, the tropospheric O_3 column is simply obtainable from an instrument with the resolution and sensitivity of SCIAMACHY. Determination of the complete altitude profile, including the troposphere, requires the development of a more sophisticated algorithm, which will include differential penetration and the Chappuis band column measurements. Figure 3 shows the sensitivity of the nadir spectrum as measured by SCIAMACHY, at the SCIAMACHY resolution, for 1% changes in total ozone column at various levels in the atmosphere. The sensitivity is shown as signal to noise ratio per pixel that can be achieved in 2 seconds of averaging time by SCIAMACHY in measuring these 1% differences at different altitudes. Figure 3 was performed using the full multiple scattering formalism of LOWTRAN7, to show the larger characteristics of the radiance changes due to ozone distribution. This does not, however, fully model the temperature dependence of the bands. Our sensitivity studies indicate that SCIAMACHY can achieve a precision corresponding to at least 1% of the total column ozone for retrieval of O_3 to 3 km vertical resolution throughout the stratosphere and troposphere.

We have calculated the ability of SCIAMACHY to measure polar ozone depletion. Calculations are performed using a solar zenith angle of 80°, appropriate to 80° N-S at the equinox. Moderate ozone hole conditions are simulated by removing 20% of the total column ozone from atmospheric above the tropopause, symmetric about the ozone peak. The nadir measurements will be able to measure polar ozone depletion to the full geographic coverage of the orbit. SCIAMACHY should also be able measure polar ozone depletion in the limb geometry to even higher latitudes, down to quite low solar zenith angles. The geographic limits to high latitude for this type of measurement are difficult to estimate precisely at present due to the difficulty in estimating the light levels under these conditions.

As an additional check on the ability of SCIAMACHY to retrieve stratospheric ozone profiles, and to distinguish between stratospheric and tropospheric ozone, we have calculated the ability of SCIAMACHY

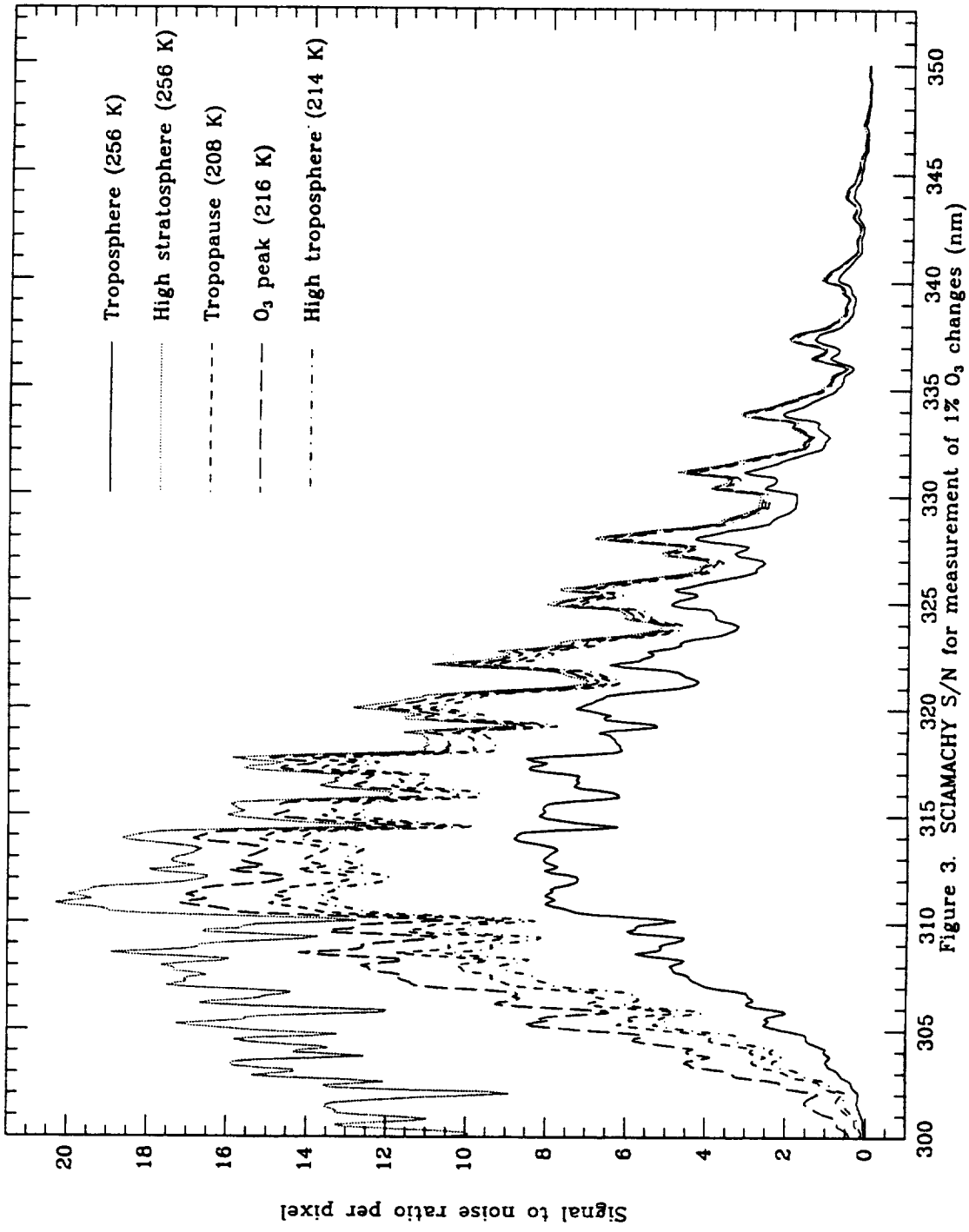

Figure 3. SCIAMACHY S/N for measurement of 1% O_3 changes (nm)

to measure stratospheric O_3 in solar occultation, chiefly using the Chappuis bands, so that the tropospheric residual may be obtained by subtraction. The signal to noise ratio per pixel for measurements of the Chappuis bands at their peak for these measurements, which correspond to a vertical resolution limited only by the slit size (1 km), is tremendous, and there are a large number of pixels covering the Chappuis bands. The implied measurement precisions are extremely high, and will be limited in practice by other factors, such as spacecraft pointing and intensity calibration. SCIAMACHY will be able to measure O_3 to better than 1% precision for each 3 km height interval from 20-40 km, assuming solar tracking to sufficient precision, and to better than 5% for the total stratospheric column. This is sufficient precision to quantitatively test the determination of tropospheric O_3 from the temperature dependence of the Huggins bands under conditions of relatively high tropospheric O_3, and to provide for some independent mapping of tropospheric O_3 at modest precision and geographic coverage. Stratospheric measurements in solar occultation extend at lower precision to at least the stratopause.

In summary, SCIAMACHY can determine the ozone column density quite accurately from the nadir measurements (to better than 1% precision); it can determine profiles to better than SBUV precision from the nadir measurements; it can cleanly distinguish between tropospheric O_3 and stratospheric O_3 from the nadir measurements and give moderate (1% of total column ozone) profile information in the troposphere; it can provide further stratospheric profile information at moderate precision from the limb scattered light; it can provide stratospheric profile information (and possibly upper tropospheric profile information) with very limited geographic coverage from solar occultation measurements, with sufficient precision to test the algorithm for determination of tropospheric O_3 from nadir measurements; it can make precise measurements of polar ozone depletion to at least 80° latitude, and probably further. The SCIAMACHY measurements of ozone are not subject to long-term degredation of the type suffered by SBUV/TOMS, as discussed in the instrumentation section of this report.

$O_2(^1\Delta)$. Quantitative laboratory spectra of $O_2(^1\Delta)$ are not available for a sensitivity limit study, but the positions are well known. Absorption by tropospheric ground state oxygen to the $^1\Delta$) state is quite prominent in the infrared spectrum. This absorption masks the emission by $O_2(^1\Delta)$ in the nadir observations. $O_2(^1\Delta)$ is used by the Solar Mesosphere Explorer satellite in limb scattering observations to determine the O_3 profile from 50-90 km;[8] SCIAMACHY will be able to measure it in limb scattering for the same purpose.

O_4. Quantitative laboratory O_4 spectra are not available for a sensitivity study. As it is quite prominent in the solar spectrum observed from the ground. As it is a van der Waals molecule, and thus has a concentration strongly dependent upon temperature and pressure, it is a useful diagnostic for cloud top and boundary layer height.

O_2 concentrations provide a cross-check of the pointing calibration in occultation and limb measurements. In the nadir view, penetration depth determinations from O_2 provide information about cloud and boundary layers heights. O_2 absorbs very strongly in the atmosphere, chiefly near 690 and 760 nm. O_2 column measurements will have a precision of 1%, our projected limit for strong absorbers. O_2 measurements in the limb and occultation geometries will also have the limiting sensitivity up to at least the stratopause.

CO. The $2 \leftarrow 0$ vibrational overtone band of CO lies between 2.3 and 2.4 μm. SCIAMACHY can be used in nadir view to measure the CO column abundance with a sensitivity limit of 2×10^{16} cm^{-2}, corresponding to 1% of background tropospheric CO, when the earth's reflectance at these wavelengths is as low as 0.1. The simulations have taken proper account of solar CO, which has lines of comparable size to the absorption from background terrestrial CO at about m = 9 and higher, but which is divided out by our solar calibrations and which, in any case, has very characteristic spectrum differences due to the much higher temperatures of solar CO. Since the tropospheric CO measurements are fundamental to the success of SCIAMACHY, the results of the simulation are checked by examining the KPNO infrared solar spectrum. The CO lines are quite prominent in the spectrum, as predicted, with most lines being sufficiently separated

from interfering H_2O and CH_4 to be cleanly measurable at the SCIAMACHY resolution. Additionally, we have calculated the ability of SCIAMACHY to measure CO in the limb geometry, by comparing the limb-scattered radiation strength with the MPI model CO concentration values and the CO line strengths. Stratospheric CO absorption can be measured with a precision ranging from 1.5% at 20 km to 15% at 30 km (by 35 km the precision has dropped to 50%). In practice, due to effects of multiple scattering, the determination of total stratospheric CO will be precise to 10-15%. Since only ca. 5% of the column CO is expected to be in the stratosphere, the limb measurements will provide for a correction to the column tropospheric CO to better than 1%. Limited CO profile information for the troposphere will be available from the differential temperature dependence of the various CO lines in nadir observing. CO is also measurable at very high signal to noise ratios in solar occultation spectra. ^{13}CO has line strengths down by a factor of 0.011 from ^{12}CO, due to the ^{13}C isotopic abundance. It will be readily measurable in the lower stratosphere in solar occultation. There is a marginal possibility that the column of ^{13}CO will be measurable from signal averaging of nadir spectra.

H_2O absorbs strongly between 700 and 1000 nm, and in the vibrational overtone bands near 2400 nm. The strong temperature dependence of these latter bands allows retrieval of the altitude profile of tropospheric H_2O in the nadir view. H_2O is retrievable in all SCIAMACHY measurement geometries to the limits of the SCIAMACHY technique - 1% in nadir, 10-20% in stratospheric profile from limb measurements, 1% in stratospheric profile from solar occultation, and 10% per 3 km interval in tropospheric profile from deconvolution of the temperature-dependent nadir spectrum.

CH_4 has strong vibration overtone absorption from 2200 to 2400 nm. As with H_2O, the temperature dependence allows retrieval of the tropospheric altitude profile from the nadir view. The limits for CH_4 profile measurements in limb-scattered light extend to 40 km in the stratosphere, due to the high concentration of CH_4 and the strength of the absorption. The column amount of $^{13}CH_4$ will almost certainly be measurable with SCIAMACHY to good precision, since 1.1% of $^{12}CH_4$ is readily measurable. However, line positions and strengths for $^{13}CH_4$ are not currently catalogued, so it is not possible to further quantify its measurement.

CO_2 has its strongest overtone absorption between 1900 and 2200 nm. As with H_2O and CH_4, the temperature dependence can be used to retrieve the tropospheric profile in the nadir view. The CO_2 absorption is so strong that the retrieval of CO_2 in all geometries is limited only by the SCIAMACHY baseline precision considerations. We note here that the SCIAMACHY CO_2 measurements are fully as capable of providing atmospheric pressure and temperature information as the standard 15 μm infrared technique, since the band used (the strongest overtone absorption of CO_2) originates from the ground state and thus supplies the same information about the distribution in energy levels of atmospheric CO_2. It may be possible to use this CO_2 information to partly correct for the effects of spacecraft jitter on limb measurements, but such corrections have not been included in the present calculations.

NO. The NO profile above the ozone layer (from 40-140 km) can be determined from SCIAMACHY limb and occultation measurements using the (1,4), (1,6), and (0,3) gamma bands which fluoresce from 255-280 nm, as determined in model sensitivity studies by Frederick and Abrams.[9] In nadir view, gamma band emission gives a column amount for NO above where O_3 absorbs strongly.

NO_2 concentrations are retrieved from the uv-visible absorption between 300 and 600 nm. In limb viewing NO_2 is readily observed in the stratosphere as already shown by SME, and by balloon measurements using this technique.[10] Stratospheric NO_2 is measurable to 10% precision from 25-40 km and 20% precision from 20-25 km in limb viewing, limited by the considerations discussed earlier. Stratospheric column determinations from limb viewing are good to 10%. In occultation, the profile will be measurable to 1% precision from 40 to below 20 km. In nadir viewing the total column is observed to the limiting 1% precision. From these two measurements tropospheric NO_2 amounts may be determined under some conditions. SME

measured NO_2 column amounts above 28 km in the range 1-3$\times 10^{15}$ molecule cm^{-2}.[4,11] This corresponds closely to the total NO_2 column abundances measured by SAGE.[12] A background tropospheric mixing ratio of 30 pptv yields a tropospheric column amount which is approximately an order of magnitude lower. In background clean air conditions deconvoluting the stratospheric and tropospheric amounts from SCIAMACHY data is marginal. In polluted air this task becomes much simpler. For 3×10^{15} cm^{-2} stratospheric NO_2, the column uncertainty is 3×10^{14} cm^{-2}, which corresponds to a tropospheric limiting concentration of 16 pptv for S/N = 1. Tropospheric NO_2 in even moderately polluted regions is substantially larger than this. In such regions, the limit for tropospheric column becomes the 1% precision of the total column NO_2. The tropospheric column can be determined to at least 10% precision for concentrations above 160 pptv. The NO_2 absorption features are known to be temperature dependent, which in nadir view may assist further in the differentiation of tropospheric and stratospheric amounts.

NO_3. The nighttime concentration of NO_3 has been measured successfully by absorption of lunar and stellar light.[13] The strongest NO_3 absorption, between 660 and 665 nm, is 2-3% deep in the occultation geometry for tangent heights of 28-38 km. Using lunar occultation we will be able to measure the profile of NO_3, when the lunar cycle permits, with potential long-term latitude coverage of 50-80° N and S.[14] The scan system can observe in both hemispheres, but the spacecraft accommodation will probably imply that the moon will only be observable in one hemisphere. Studies will be made in Phase B of the possible use of planets and stars (e.g., Venus) for nighttime occultation measurements. This is a significant portion of the region where enhanced NO_3 is expected in polar night conditions. The lunar occultation signal measured by SCIAMACHY is down from the solar occultation signal by a factor of 1.2 $\times 10^{-6}$ due to the geometric factors and the lunar albedo. For NO_3 at 30 km, using 1.5 second integration time, the numbers of photons per pixel at 660-665 nm is 4.2 $\times 10^6$ for a signal to noise ratio per pixel of 2.0 $\times 10^3$. For 2% absorption at band center, the NO_3 is measured with 2.4% precision.

N_2O. The $00^02 \leftarrow 00^00$ vibrational overtone band of N_2O lies between 2.25 and 2.30 μm. Lines of N_2O are quite prominent in the Kitt Peak solar spectra, with many individual lines well separated from interferences at the SCIAMACHY level. The N_2O column is measurable to the limiting nadir precision (1%) in all but the lowest surface reflectance and highest solar zenith angle conditions. In limb measurement, N_2O can be measured to a precision limited only by spacecraft jitter ($\leq$ 10%) up to 30 km, and to about 40% up to 35 km. The total stratospheric N_2O will be precise to 10%; tropospheric columns should be obtainable by subtraction to 5% or better. The temperature dependence of the multiple N_2O lines may provide some information on the vertical distribution of tropospheric N_2O.

2.2 Polluted troposphere molecules

HCHO absorbs between 250 and 360 nm, with its strongest absorption between 300 and 350. The short wavelength absorption is strongly obscured by O_3 absorption, leaving a contribution between about 300 and 350 nm. This window is highly dependent on the O_3 concentration and the viewing geometry and the temperature and concentration of tropospheric O_3 (increased absorption by warm tropospheric ozone will further obscure the HCHO). HCHO is measurable in the nadir view, chiefly at low latitudes. The sensitivity for HCHO measurements with this concentration is 5. Thus, moderately enhanced HCHO can be observed with modest precision and major pollution can be readily measured. Note that this signal to noise ratio is determined using only the portions of the HCHO spectrum close to 350 nm, which remain reasonably unobscured by O_3. The sensitivity increases by as much as a factor of 2 under conditions of low column O_3.

SO_2 absorbs between 290 and 315 nm. It is observable in the nadir view, and under conditions of low tropospheric ozone, in the polluted troposphere. For a tropospheric concentration of 20 ppbv (moderate pollution in the boundary layer) SCIAMACHY achieves a signal to noise ratio of 60 (i.e., better than 2% precision), but this is highly variable, depending on the O_3 concentration. SO_2 in normal background

concentrations is not observable.

2.3 Ozone hole molecules

ClO absorbs from 220 to 310 nm. It is strongly masked by ozone absorption. Our sensitivity limit for the nadir view varies from about 10^{13} to 10^{15} cm^{-2}, depending on the ozone concentration. We do not expect to be able to detect ClO under normal conditions. Unusually high ClO concentration coupled with low O_3 concentration (which will improve the detection limit substantially), as found in the Antarctic ozone "hole"[15] will make the ClO column observable. An absorption spectrum of ClO calculated using a representative O_3 hole concentration of 1.5×10^{15} cm^{-2}, compared with a synthesis of the nadir spectrum at an 80° solar zenith angle, under moderate ozone hole conditions, gives a precision for ClO column measurements of 10%.

OClO absorbs strongly between 280 and 440 nm. It is formed in the atmosphere from the reaction of BrO with ClO and destroyed by photolysis. OClO has been observed using its structured absorption between 320 and 420 nm at night over Antarctica in spring (column densities of 1×10^{14} molecule cm^{-2}.[16,17] Using our synthesized nadir spectrum for moderate ozone hole condition and the OClO absorption for 1×10^{14} cm^{-2}, corresponding to a twilight concentration, we obtain a 2% measurement precision for OClO. For a typical daytime concentration (2×10^{13} cm^{-2}) we can measure to 10% precision. It may be possible to obtain OClO profile information at ozone hole concentrations using lunar occultation; insufficient profile modeling is available to accurately estimate the profile limits.

BrO has been measured in the Antarctic spring using its UV absorption.[17] By comparing the absorption of BrO for a nadir concentration of 2.5×10^{13} for our ozone hole geometry, we determine that we can measure this column density of BrO with a precision of 10%. Under normal conditions, the BrO column density is 1.5×10^{13}, implying measurements to 15%. BrO profile ranges are estimated using MPI 2-D models calculations. With solar occultation, BrO in normal concentrations can be measured to 25% from 15-35 km. In limb measurements, BrO profiles can be determined to 50% precision from 20-25 km in normal concentrations and ca. 30% in ozone hole concentrations.

2.4 Surface reflectance and solar zenith angle studies

Absolute radiometric calibration of the SCIAMACHY instrument, combined with direct solar observations, will provide new global information about surface spectral reflectance in the range 300-2400 nm. Although the spatial resolution of SCIAMACHY is limited, this data will be very useful scientifically. Further studies of the retrieval of the reflectance measurements by SCIAMACHY will be made in Phase B.

Surface reflectance and solar zenith angle considerations for molecule measurements in nadir viewing are coupled together since the increased path due to larger solar zenith angle can offset decreased light due to lower reflectance for those molecules measured at wavelengths that penetrate fully to the ground. The increased path can also exacerbate measurements of tropospheric molecules made at shorter wavelengths due to increased loss of tropospheric information because of increased Rayleigh scattering in the stratosphere. Our standard conditions for sensitivity studies (35° N: 63° solar zenith angle; albedo =0.3) are fairly stringent in the sense that, for the suite of molecular measurements by SCIAMACHY, the deterioration in global coverage due to lower reflectance and other solar zenith angles is not severe. The losses that do occur are mainly in tropospheric measurements.

Surface reflectances and solar zenith angles other than our standard conditions have their greatest impacts on the following measurements: Tropospheric O_3. At 320 nm, 13% of the light measured by SCIAMACHY at our standard 35° N (63° solar zenith angle) is reflected from the ground. For albedo = 0.1, this decreases to 3.6%, and the precision for tropospheric O_3 is a factor of 2 lower. Losses in tropospheric O_3 information are partly compensated for by increased solar zenith angle, since the light at the red end of the Huggins bands has significant penetration to quite high solar zenith angle. Tropospheric NO_2 is measured at

modest precision in our standard conditions, in a wavelength range where Rayleigh scattering is not a major problem. Sensitivity to tropospheric NO_2 varies roughly as the square root of the reflectance. Measurements of the tropospheric columns of HCHO and SO_2 will suffer with decreased reflectance. HCHO sensitivity will increase almost linearly with the increased path due to higher zenith angle, up to quite high angle, because of the long wavelength extent of the spectrum. SO_2 sensitivity changes with zenith angle will be small. ClO, OClO, and BrO column measurements were calculated at a high solar zenith angle (80°), appropriate to measurements by SCIAMACHY in ozone hole conditions. ClO is measured at such short wavelengths that changes in surface reflectance are not a serious consideration in measurement sensitivity; variability in O_3 has a much more serious impact. ClO will generally be seen at high solar zenith angles, so that sensitivity vs. zenith angle is not an important issue. OClO is also generally seen at these high zenith angles. Its measurement is more sensitive to surface reflectance since the spectrum extends well beyond 400 nm. Fortunately, the climatology of OClO is such that measurements will generally occur in regions of high surface reflectance; exceptions occur when the ozone hole conditions extend over ice-free ocean waters. Even in these conditions, the strength of the absorption in the 300-350 nm range ensures useful measurement sensitivity. The spectrum of BrO has its major absorption in the 300-350 nm range, long enough that O_3 absorption is not a serious problem and short enough that lower surface reflectance also will not seriously hamper its measurement. BrO measurement under normal conditions (i.e., away from O_3-depleted polar regions) will be decrease as the path length decreases due to lower solar zenith angle.

3. AEROSOL STUDIES

The presence of aerosols in climatic models leads to a more important energy deposition in the stratosphere and to a cooling of the troposphere. More recently, the Antarctic ozone hole phenomenon has been explained by the conversion of HCl to ClO by heterogeneous reactions on the surfaces of polar stratospheric clouds.

The SCIAMACHY instrument will obtain aerosol data in occultation, limb-scattering and nadir measurements. The high resolution permits distinction between gases and aerosols and will allow altitude distributions and granulometry of the middle-atmospheric aerosols to be obtained. Proper treatment of aerosols in the inversion process also results in more accurate data on the vertical distribution of gases. Simulation and verification of the various types of spectral signatures from different aerosols are an integral part of the SCIAMACHY data system development plan.

3.1 Stratospheric Aerosols

Stratospheric aerosols have been extensively studied from balloon and space experiments over the last 30 years: The measurements show spherical particles in the stratosphere composed of a mixture of sulfuric acid and water. These are divided between layers of large particle size, the Junge layer (typical size 0.15 μm), and a background layer of aerosols of significantly smaller size (ca. 0.05 μm). However, in the polar stratospheric clouds associated with the Antarctic ozone hole, particle sizes larger than 1 μm have been conjectured. Other types of suspended particles exist in the upper atmosphere, from meteoric decay; little is known about them except that their metallic cores give them an important imaginary refractive index and that the resulting increase of Mie scattering efficiencies makes them more observable, as published in visual space observations and balloon data reports. SCIAMACHY, through measurements of these latter particles, may help solve the present controversy concerning the geophysical impacts of small meteorites and comets.

3.2 Tropospheric Aerosols

The high spectral resolution of the SCIAMACHY instrument combined with its spatial resolution can lead to study of image contrast, and to a characterization of the nature of tropospheric haze in terms of natural phenomena. For example, sand winds have never been monitored on a global scale. Since they occur by definition mostly in dry regions, the absence of clouds will make SCIAMACHY a perfect sensor for them. SCIAMACHY will also measure the high quantities of soot from forest fires to which, for decades, the blue moon phenomenon has been attributed. Identification of these "clouds" and their continuous observation will lead to an assessment of the effects of these largely local phenomena on the global atmospheric system.

4. REFERENCES

1. R. B. Norton and J. F. Noxon, "Dependence of Stratospheric NO_3 Upon Latitude and Season", *J. Geophys. Res. 91,* 5323-5330, 1986.

2. L. S. Rothman, R. R. Gamache, A. Goldman, L. R. Brown, R. A. Toth, H. M. Pickett, R. L. Poynter, J.-M. Flaud, C. Camy-Peyret, A. Barbe, N. Husson, C. P. Rinsland, and M. A. H. Smith, "The HITRAN Database: 1986 Edition", *Appl. Opt. 26,* 4058-4097, 1987.

3. K. V. Chance, D. G. Johnson, and W. A. Traub, "Measurement of Stratospheric HOCl: Concentration Profiles, Including Diurnal Variation", *Journal of Geophysical Research 94,* 11,059-11,069, 1989.

4. G. H. Mount, D. W. Rusch, J. F. Noxon, J. M. Zawodny, and C. A. Barth, "Measurements of Stratospheric NO_2 from the Solar Mesosphere Explorer Satellite", *J. Geophys. Res. 89,* 1327-1340, 1984.

5. J. Fishman, "Tropospheric Ozone from Satellite Total Ozone Measurements", in *Tropospheric Ozone* (Ed. I. S. A. Isaksen), 111-123, D. Reidel, Hingham, MA, 1988.

6. A. M. Bass, and R. J. Paur, "The Ultraviolet Cross-sections of Ozone: I. Measurements", in *Atmospheric Ozone, Proceedings of the Quadrennial Ozone Symposium* (Ed. C. Zerefos and A. Ghazi), 606-616, D. Reidel, Hingham, MA, 1985.

7. K. Yoshino, D. E. Freeman, J. R. Esmond, and W. H. Parkinson, "Absolute Absorption Cross-section Measurements of Ozone in the Wavelength Region 238-335 nm and the Temperature Dependence", *Planet. Space Sci. 36,* 395-398, 1988.

8. R. J. Thomas, C. A. Barth, D. W. Rusch, and R. W. Sanders, "Solar Mesosphere Explorer Near-infrared Spectrometer: Measurements of 1.27-μm Radiances and the Inference of Mesospheric Ozone", *J. Geophys. Res. 89,* 9569-9580, 1984.

9. J. E. Frederick and R. B. Abrams, "Model Studies of Nitric Oxide Fluorescence in the Earth's Backscattered Spectrum", *Planet. Space Sci. 30,* 137-145, 1982.

10. C. T. McElroy, "Stratospheric Nitrogen Dioxide Concentrations as Determined from Limb Brightness Measurements made on June 17, 1983", *J. Geophys. Res. 93,* 7075-7083, 1988.

11. G. H. Mount, D. W. Rusch, J. M. Zawodny, J. F. Noxon, C. A. Barth, G. J. Rottman, R. J. Thomas, G. E. Thomas, R. W. Sanders, and G. M. Lawrence, "Measurement of NO_2 in the Earth's Atmosphere using a Limb Scanning Visible Spectrometer", *Geophys. Res. Lett. 10,* 265-268, 1983.

12. World Meteorological Organization, Global Ozone Research and Monitoring Project Report No. 16, "Atmospheric ozone 1985: Assessment of our understanding of the processes controlling its present distribution and change", Geneva, 1986.

13. P. Rigaud, J. P. Naudet, and D. Huguenin, "Simultaneous Measurements of Vertical Distributions of Stratospheric NO_3 and O_3 at Different Periods of the Night", *J. Geophys. Res. 88,* 1463-1467, 1983.

14. J. Vercheval, "Latitude Coverage of Solar Absorption Spectrometry Observations of the Middle Atmosphere from a Heliosynchronous Orbit", *ESA Journal 11,* 233-238, 1987.

15. R. L. de Zafra, M. Jaramillo, A. Parrish, P. Solomon, B. Connor, and J. Barrett, "High Concentrations of Chlorine Monoxide at Low Altitudes in the Antarctic Spring Stratosphere: Diurnal Variation", *Nature 328,* 408-411, 1987

16. S. Solomon, G. H. Mount, R. W. Sanders, and A. L. Schmeltekopf, "Visible Spectroscopy at McMurdo Station, Antarctica 2. Observations of OClO", *J. Geophys. Res. 92,* 8329-8338, 1987.

17. S. Solomon, R. W. Sanders, M. A. Carroll, and A. L. Schmeltekopf, "Visible and Near-ultraviolet Spectroscopy at McMurdo Station Antarctica 5. Observations of the Diurnal Variations of BrO and OClO", *J. Geophys. Res. 94,* 11,393-11,403, 1989.

OZONE PROFILE RETRIEVALS FROM THE ESA GOME INSTRUMENT

R. Munro and B.J. Kerridge
Science and Engineering Research Council
Rutherford Appleton Laboratory
Chilton, Didcot, Oxon OX11 0QX, U.K.

J.P. Burrows
Universität Bremen, Fachbereich Physik
Institüt für Fernerkundung
Postfach 33 04 40 D-2800 Bremen 33, Germany

Dr. K. Chance
Harvard-Smithsonian Center for Astrophysics
60 Garden St., Cambridge
Massachusetts, 02138 U.S.A.

26th May, 1992

ABSTRACT

The potential of the ESA Global Ozone Monitoring Experiment (GOME) to produce ozone profile information, has been examined by carrying out two sample retrievals using simulated GOME data. The first retrieval examines the potential of the GOME instrument to produce stratospheric ozone profiles using the traditional *back-scatter ultraviolet* technique, while the second examines the possibility of obtaining tropospheric profile information, and improving the quality of the stratospheric profile retrievals, by exploiting the temperature dependence of the ozone Huggins bands.

INTRODUCTION

The GOME instrument is a nadir-viewing grating spectrometer, under development by the European Space Agency, for launch on the second European Research Satellite (ERS-2) in late 1994.

It will measure solar radiation back-scattered from the earth's atmosphere in the spectral region 240–790 nm, at moderate resolution (0.2–0.4 nm) throughout the range. The primary measurement technique to be exploited by the GOME is known as Differential Optical Absorption Spectroscopy (DOAS). Using this technique, the column abundance of a trace gas is derived from a back-scattered ultraviolet/visible spectrum by ratioing it to a solar spectrum, high pass filtering, cross-correlating with a laboratory measured spectrum to obtain the slant column density, and converting from slant to vertical columns by use of air-mass factors (Platt & Perner, 1985; Platt *et al.*, 1980a, 1980b, 1981; Hübler *et al.*, 1984).

In this capacity the GOME is expected to produce column abundances of a number of trace gases (e.g. O_3, NO, NO_2, BrO, H_2O, O_2 and O_4).

In addition, the GOME will produce ozone profiles using the back-scatter ultraviolet method which has been successfully exploited by NASA's Solar Backscatter UltraViolet (SBUV) instruments (Heath *et al.*, 1975). This technique requires an absolute radiometric calibration. For this purpose, the GOME will have the capability to observe the sun via a diffuser plate, and the moon directly.

As the GOME will have a much broader spectral coverage and higher spectral resolution than the SBUV instruments, which obtain useful measurements at only eleven wavelengths between 273 and 340 nm, it is hoped that improved vertical profile information will be obtained. Of particular interest is the possibility of retrieving tropospheric profile information. In order to obtain ozone profile information in the troposphere from the GOME measurements, it is necessary to take advantage of the temperature dependence of the ozone absorption features from 300–340 nm, known as the Huggins bands (fig. 1). Since the variation in absorption cross-section with temperature is small (around a few percent per 10K; Paur & Bass, 1985; Yoshino, 1988), it is necessary to obtain measurements with a high signal to noise ratio to allow the height information to be extracted.

Figure 1. The ozone absorption bands known as the Huggins bands (Nicolet, 1980).

It is expected that the GOME will be able to provide measurements with sufficiently high signal to noise ratios (~1000) in this spectral region to allow tropospheric profile information to be obtained. The remainder of this paper is devoted to a discussion of ozone profile retrievals carried out using simulated GOME data.

METHOD

Two sample ozone profile retrievals have been carried out using simulated GOME data at a spectral resolution of 0.2 nm; the first using measurements from the 255–300 nm region only, and the second using measurements from the 255–340 nm region including the temperature dependent Huggins bands.

The measurements were simulated using LOWTRAN7, a radiative transfer code including multiple scattering (Kneizys *et al.*, 1988). Representative GOME instrument noise was then added. The simulated back-scattered spectrum was subsequently divided by the solar source spectrum in order to remove the effect of the large variation in incident intensity. The solar spectrum was also calculated using LOWTRAN7.

To date, no attempt has been made to examine the effect of errors in wavelength registration between the measured back-scattered and solar spectrum. Neither has the effect of uncertainties in radiometric calibration been examined. Total ozone, assumed to be known to within ±1%, was also included as an additional measurement.

Figure 2. Ozone profile retrieval using simulated GOME data from 255–300 nm.

In both cases the retrieval method used was optimal estimation (Rodgers, 1976, 1990) and the forward model used in the retrieval process was once again LOWTRAN7 (Kneizys, *op. cit.*). The *a priori* information was assumed to be known to within ±30% (in volume mixing ratio) of the "true" profile used to simulate the measurements.

Both simulations were carried out under the following conditions: nadir viewing; no clouds; no aerosol; over-head sun; a surface albedo of 0.3; temperature profile known exactly and spectroscopic data known exactly. The background atmosphere used was the US Standard Atmosphere (NOAA, 1976). The results obtained under these conditions are discussed in the following section.

RESULTS AND DISCUSSION

As shown in fig. 2, the retrieval carried out using only measurements in the 255–300 nm region, produces good profile information over the altitude range 20–60 km. In this case, height information is obtained by exploiting the wavelength dependence of effective scattering altitude for radiation at wavelengths shorter than 300 nm. As noted, this technique has been successfully applied to the SBUV instrument data sets (Heath *et al.*, *op. cit.*). Since the Huggins bands have been excluded, and all radiation at wavelengths shorter than 300 nm is scattered above the tropopause (Brasseur & Solomon, 1986,

Figure 3. Ozone profile retrieval using simulated GOME data from 255–340 nm, including the temperature dependent Huggins bands.

Figure 4. Ratio of the measured back-scattered spectrum to the incident solar spectrum, both with and without tropospheric ozone.

fig. 4.3) no tropospheric profile information has been obtained. Conversely, when the Huggins bands are included in the retrieval the tropospheric profile is well determined (fig. 3). The relative contribution of tropospheric ozone to the total absorption in the Huggins bands may be seen in fig. 4. This shows the ratio of the measured backscattered spectrum to the incident solar spectrum, both with and without tropospheric ozone. It is possible to see that tropospheric ozone does make a notable contribution to the total absorption in the Huggins bands, thus providing sufficient information to discriminate between the stratospheric and tropospheric profiles. Inclusion of the Huggins bands also significantly improves the information content of the retrievals at stratospheric altitudes, up to 40 km. However, these simulations represent the best possible situation only. In practice, factors such as uncertainties in spectroscopic parameters, uncertainties in the temperature profile, poor *a priori* information, uncertainties in the radiometric calibration of the instument etc. will all serve to degrade the quality of the profile information.

CONCLUSION

The potential of the ESA GOME instrument, to produce both stratosheric and tropospheric profiles of ozone, has been demonstrated by carrying out two sample retrievals using simulated GOME data. The simulations have shown that it is possible to obtain good ozone profile information from the ground up to 60 km by taking advantage of the temperature dependence of the ozone Huggins bands. It must be recognized that these simulations represent the best possible situation only. In practice, there will be many other souces of error which will increase the uncertainties on the retrieved profiles. In addition, it has been shown that using the GOME data, it is possible to retrieve stratospheric ozone profiles using the traditional back-scatter ultraviolet technique exploited by NASA's SBUV instruments.

REFERENCES

Brasseur, G. and Solomon, S. (1986), *Aeronomy of the Middle Atmosphere*, D. Reidel Publishing Co., Dordrecht, The Netherlands, *p* 90.

Heath, D.F., Krueger, A,J., Roeder, H.A. and Henderson, B.D. (1975), The Solar Backscatter Ultraviolet and Total Mapping Spectrometer (SBUV/TOMS) for Nimbus G, *Opt. Eng.*, 14, *pp* 323–331.

Hübler, G., Perner, D., Platt, U., Toennissen, A., and Ehhalt, D.H. (1984), Ground level OH radical

concentrations: comparison of field data with model predictions, *J. Geophys. Res.*, **89**, *pp* 1309–1319.

Kneizys, F., Shettle, E.P., Abreu, L.W., Chetwynd, J.H., Anderson, G.P., Gellery, W.O., Selby J.E.A. and Clough S.A. (1988), *Users Guide to LOWTRAN 7*, Air Force Geophysics Laboratory, Report AFGL-TR-88-0177, Hanscom AFB, MA, U.S.A., *pp* 137.

Nicolet, M. (1980), The chemical equations of stratospheric and mesospheric ozone, *Proceedings of the NATO Advanced Study Institute on Atmospheric Ozone (Portugal)*, edited by U.S. Department of Transportation, FAA Washington, D.C., USA, Report No. FAA-EE-80-20.

NOAA (1976), *The U.S. Standard Atmosphere*, National Oceanic and Atmospheric Administration, National Aeronautics and Space Administration, United Stated Air Force, Washington D.C. 20402, Stock No. 003-017-00323-0.

Paur, R.J. and Bass, A.M. (1985), The ultraviolet cross-sections of ozone: II. Results and temperature dependence, in, *Atmospheric Ozone, Proceedings of the Quadrennial Ozone Symposium*, Halkidiki, Greece, September 3–7, 1984, edited by C.S. Zerefos and A. Ghazi, D. Reidel, Dordrecht, The Netherlands, *pp* 611–616.

Platt, U. and Perner, D. (1985), Direct measurements of atmospheric CH_2O, HNO_2, O_3, NO_2 and SO_2 by differential optical absorption in the near UV, *J. Geophys Res.*, **85**, *pp* 7453–7458.

Platt, U., Perner, D., Harris, G.W., Winer, A.M. and Pitts, J.N. (1980a), Observation of nitrous acid in an urban atmosphere by differential optical absorption, *Nature*, **285**, *pp* 312–314.

Platt, U., Perner, D., Harris, G.W., Pitts, J.N., and Winer, A.M. (1980b), Detection of NO_3 in the polluted troposphere by differential optical absorption spectroscopy, *Geophys. Res. Letts.*, **7**, *pp* 89–92.

Platt, U., Perner, D., Schroeder, J., Kessler, C. and Toennissen, A. (1981), The diurnal variation of NO_3, *J. Geophys. Res.*, **86**, *pp* 11965–11970.

Rodgers, C.D. (1976), Retrieval of atmospheric temperature and composition from remote measurements of thermal radiation, *Rev. Geophys. Space Phys.*, **14**, *pp* 609–624.

Rodgers, C.D. (1990), Characterisation and error analysis of profiles retrieved from remote sensing measurements, *J. Geophys. Res.*, **95**, D5, *pp* 5587–5595.

Yoshino, K., Freeman, D.E., Esmond, R. and Parkinson, W.H. (1988), Absolute absorption cross-section measurements of ozone in the wavelength region 238–335 nm and the temperature dependence, *Planet. Space Sci.*, **36**, *pp* 395–398.

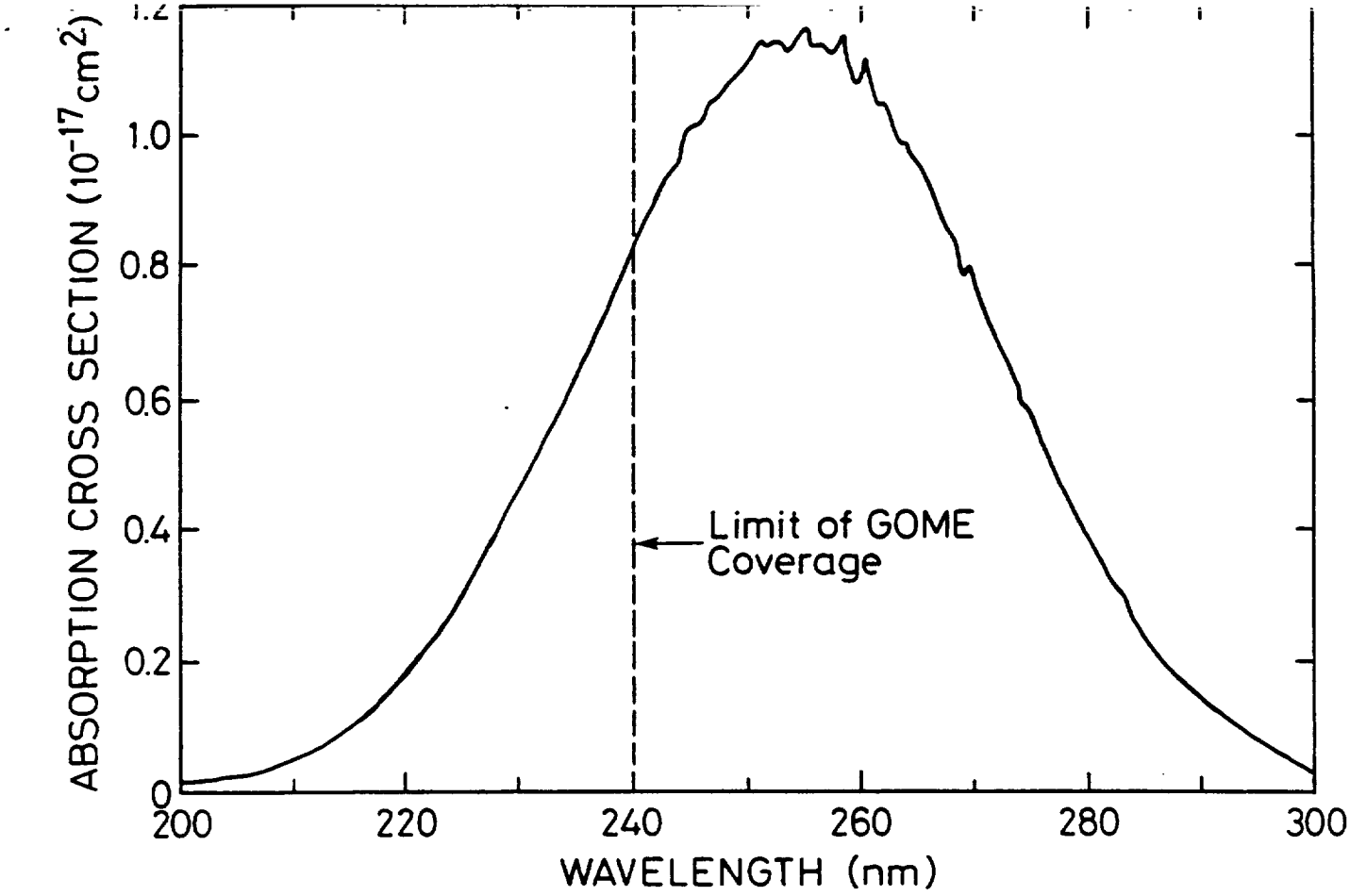

Ozone Huggins Bands

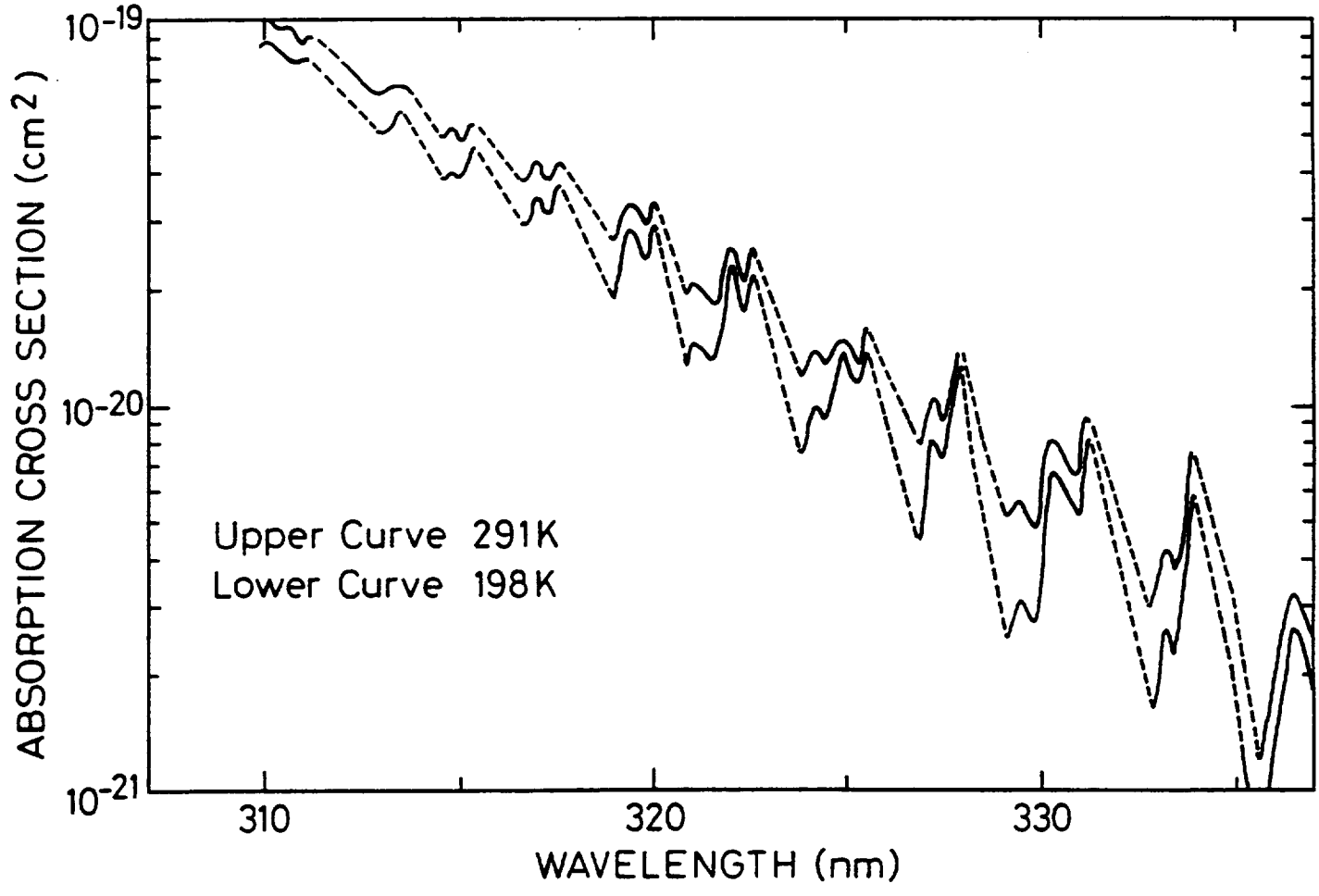

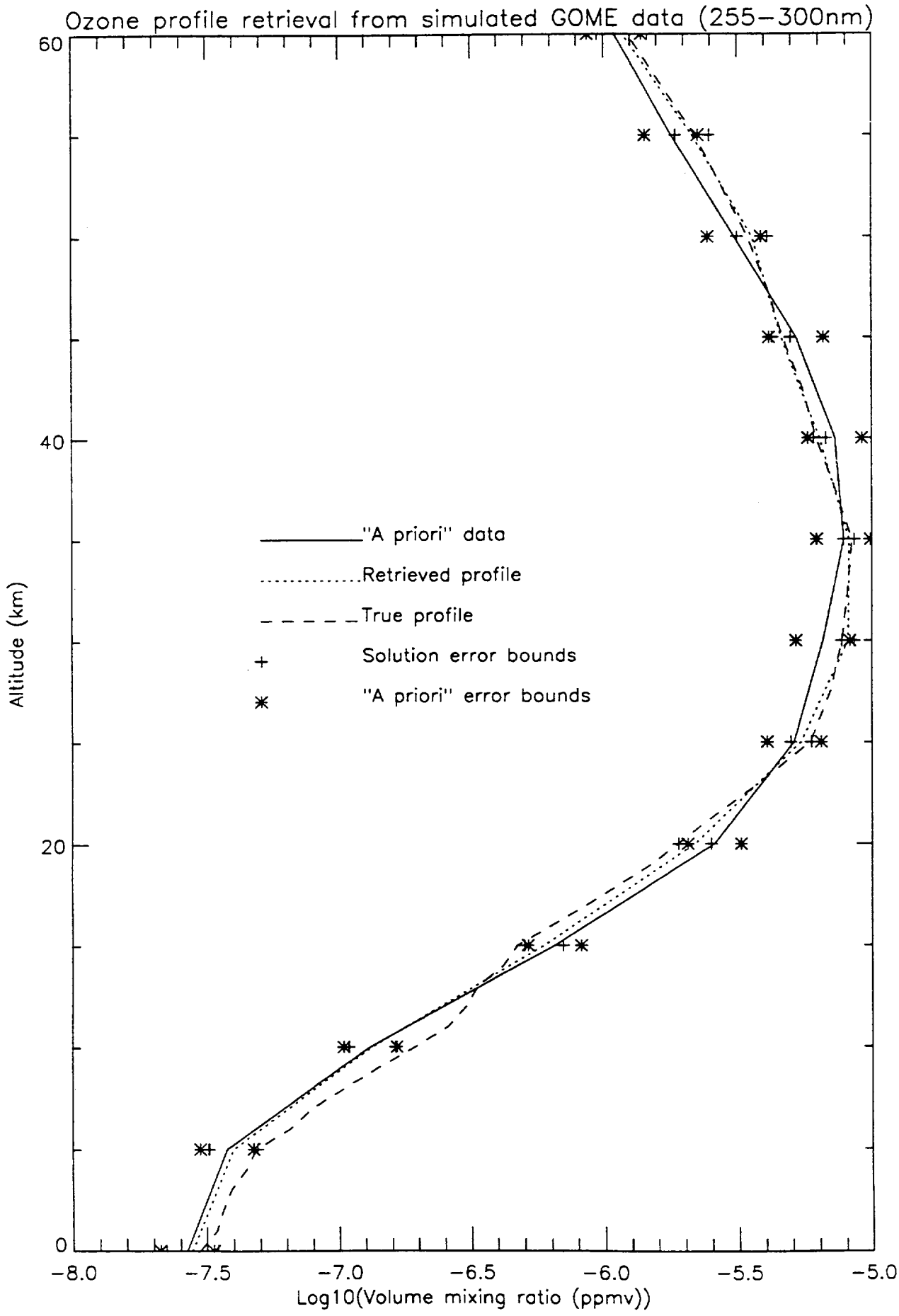
Ozone profile retrieval from simulated GOME data (255–300nm)
60
40
20
0
Altitude (km)
"A priori" data
Retrieved profile
True profile
Solution error bounds
"A priori" error bounds
−8.0
−7.5
−7.0
−6.5
−6.0
−5.5
−5.0
Log10(Volume mixing ratio (ppmv))

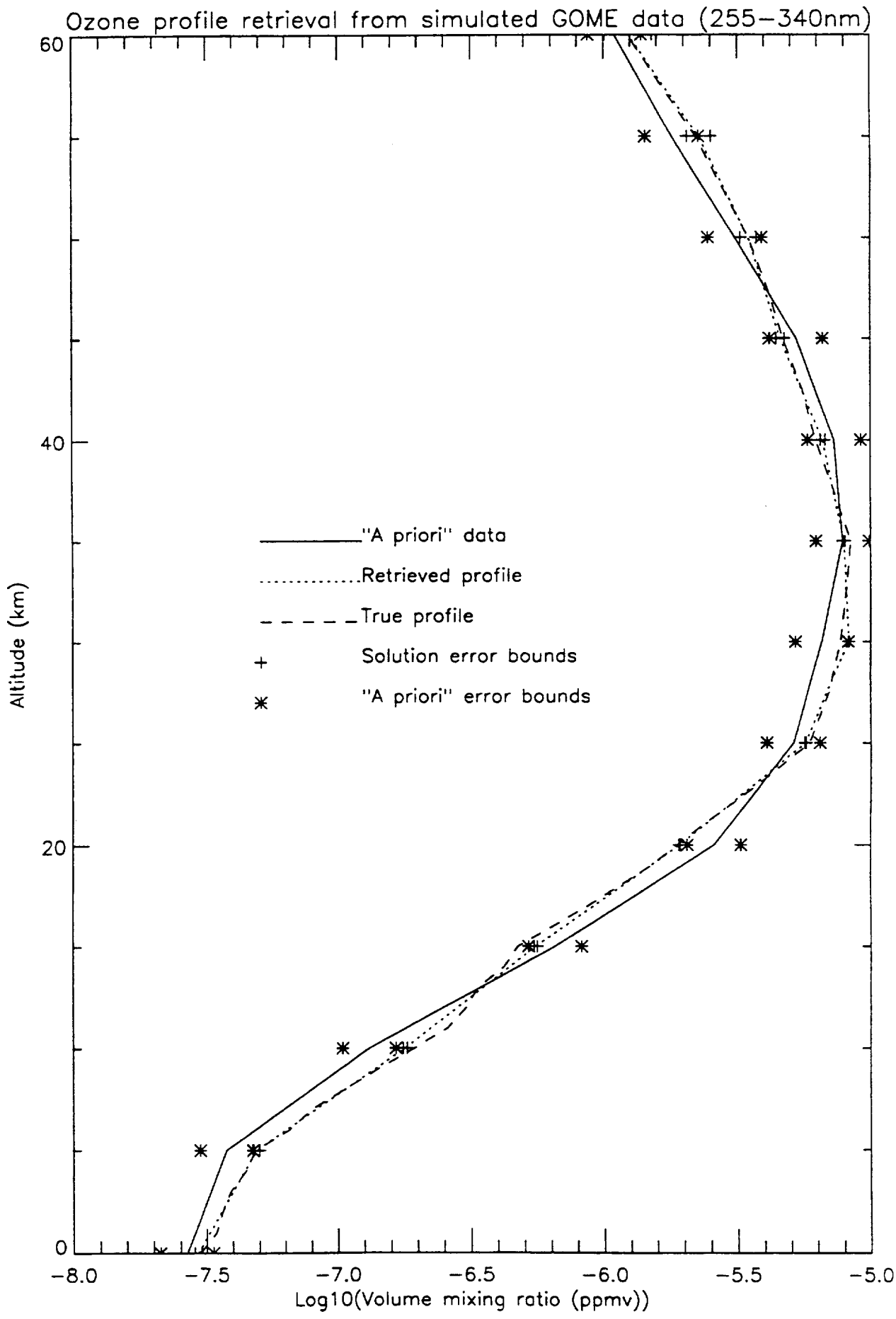
Ozone profile retrieval from simulated GOME data (255–340nm)
60
40
20
0
Altitude (km)
"A priori" data
Retrieved profile
True profile
Solution error bounds
"A priori" error bounds
−8.0
−7.5
−7.0
−6.5
−6.0
−5.5
−5.0
Log10(Volume mixing ratio (ppmv))

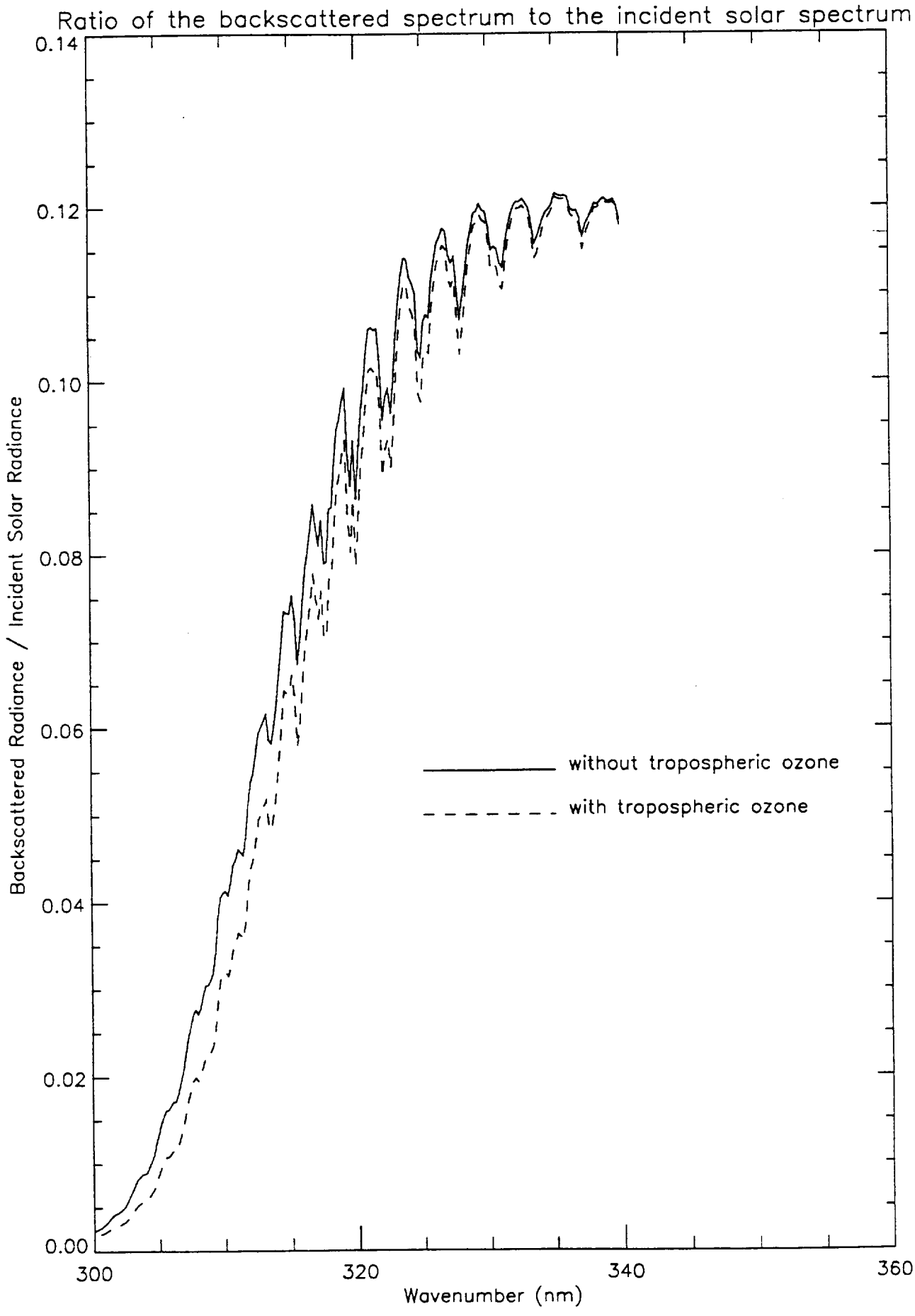
Ratio of the backscattered spectrum to the incident solar spectrum
Backscattered Radiance / Incident Solar Radiance
0.14
0.12
0.10
0.08
0.06
0.04
0.02
0.00
300
320
340
360
Wavenumber (nm)
without tropospheric ozone
with tropospheric ozone

JOURNAL OF GEOPHYSICAL RESEARCH, VOL. 99, NO. D7, PAGES 14,481–14,491, JULY 20, 1994

Analysis of cloud top height and cloud coverage from satellites using the O_2 *A* and *B* bands

Akihiko Kuze and Kelly V. Chance

Harvard-Smithsonian Center for Astrophysics, Cambridge, Massachusetts

Abstract. Cloud height and cloud coverage detection are important for total ozone retrieval using ultraviolet and visible scattered light. Use of the O_2 *A* and *B* bands, around 761 and 687 nm, by a satellite-borne instrument of moderately high spectral resolution viewing in the nadir makes it possible to detect cloud top height and related parameters, including fractional coverage. The measured values of a satellite-borne spectrometer are convolutions of the instrument slit function and the atmospheric transmittance between cloud top and satellite. Studies here determine the optical depth between a satellite orbit and the Earth or cloud top height to high accuracy using FASCODE 3. Cloud top height and a cloud coverage parameter are determined by least squares fitting to calculated radiance ratios in the oxygen bands. A grid search method is used to search the parameter space of cloud top height and the coverage parameter to minimize an appropriate sum of squares of deviations. For this search, nonlinearity of the atmospheric transmittance (i.e., leverage based on varying amounts of saturation in the absorption spectrum) is important for distinguishing between cloud top height and fractional coverage. Using the above-mentioned method, an operational cloud detection algorithm which uses minimal computation time can be implemented.

1. Introduction

More than 50% of the Earth's surface is covered with clouds. Cloud height and cloud coverage detection are important for a number of atmospheric measurement purposes, including total ozone retrieval and distinction between the stratospheric and tropospheric O_3 burdens using ultraviolet and visible scattered light. The Nimbus 7 total ozone mapping spectrometer and solar backscattered ultraviolet instruments use scattered solar ultraviolet light for ozone profile and total ozone retrieval [*Fleig et al.*, 1990]. They estimate cloud coverage from measured reflectivity at 340 nm, assuming that the cloud top exists uniformly at a pressure of 0.4 atm. For improvement in environmental monitoring, more detailed cloud detection is required.

To collect enough photons for the required signal-to-noise ratios in measurements, a spaceborne spectrometer usually has a larger instantaneous field of view (IFOV) than radiometers like the thematic mapper (LandSat-D) and Système Probatoire d'Observation de la Terre. The large IFOV of the spectrometer will often include both cloud-containing and cloud-free areas. High spatial resolution cloud distribution data are obtained by the spaceborne radiometers, but it is difficult for them to detect cloud height.

Figure 1 shows the calculated radiance in the O_2 visible region for complete coverage in a few cloud type cases using the radiative transfer model MODTRAN [*Berk et al.*, 1989] in the case of $\theta = 60°$ and $\varphi = 0°$, where θ is the solar zenith angle and φ is the nadir-viewing angle. The absolute level of the measured radiance depends on the cloud type. Also, it is difficult to distinguish cloud from Earth albedo variation. Thus a method providing direct information on the atmospheric structure, such as the measurement of relative radiances using absorption lines, is necessary for improved cloud parameter detection. Use of the O_2 *A* and *B* bands, around 761 and 687 nm, is such a method, one which we will demonstrate makes it possible to detect cloud height and coverage parameters simultaneously from a nadir-viewing instrument. Cloud altitude estimation using the O_2 *A* band was suggested by *Yamamoto and Wark* [1961], and a detailed study was done by *Wark and Mercer* [1965]. *Saiedy et al.* [1967] determined cloud top height on a Gemini mission using a spacecraft-borne spectrograph camera with 0.5-nm resolution. *Fisher and Grassl* [1991] and *Fisher et al.* [1991] measured the O_2 *A* band with an airborne 0.6-nm spectral resolution spectrometer having high spatial resolution and detected cloud top height with 50-m accuracy. However, it is rare that an entire IFOV for a satellite-based spectrometer (typically 100 × 100 km) is covered evenly by a cloud layer. Therefore cloud coverage detection is also important. We show that using a moderately high (approximately 4.0-cm^{-1} resolution) spectrometer and measuring in several absorption channels, both cloud top height and cloud coverage detection become possible.

The study done here is a prototype for the Global Ozone Monitoring Experiment (GOME) and the scanning imaging absorption spectrometer for atmospheric chartography (SCIAMACHY), which are European satellite instruments designed primarily for atmospheric trace gas measurements. GOME and SCIAMACHY are both diode array-based spectrometers, which measure the atmospheric spectrum with continuous coverage from 240 to 790 nm at a resolution of about 0.1 nm in the ultraviolet and 0.2 nm in the visible. Measurements in this region are expected to provide determinations of the atmospheric trace species O_3, NO_2, and BrO, and the more abundant species O_2, $(O_2)_2$, and H_2O, and have prospects for measuring H_2CO, SO_2, ClO, and

Paper number 94JD01152.
0148-0227/94/94JD-01152$05.00

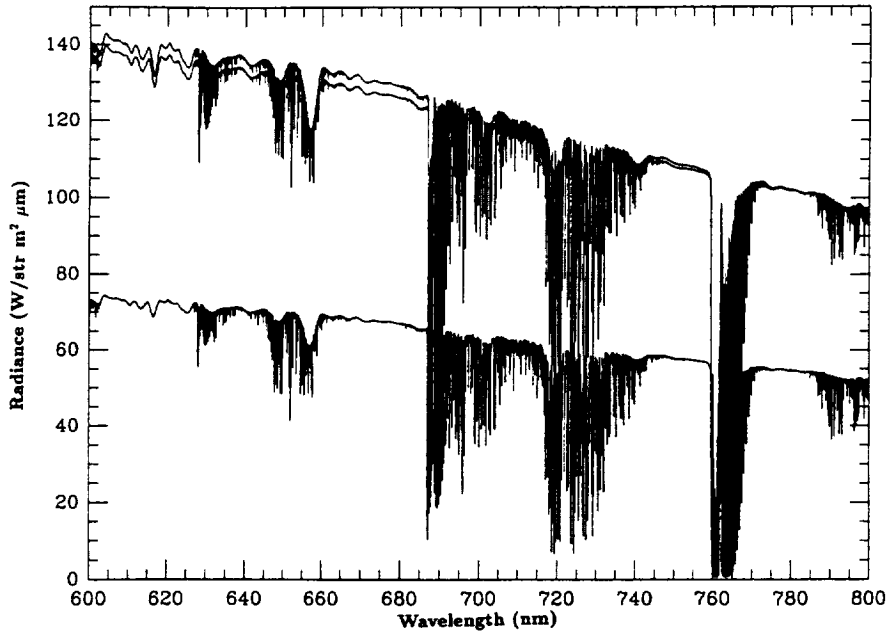

Figure 1. Calculated radiance in the visible region, including the O_2 *A* and *B* bands, for complete coverage of selected cloud types. From the top, altostratus, stratus, and cloud free.

OClO under special conditions. The wavelength coverage of both instruments includes the ultraviolet Hartley and Huggins bands and the visible Chappuis bands of O_3. The continuous spectral coverage of SCIAMACHY continues into the infrared, to 1700 nm, with additional detector arrays at 2.0 and 2.3 μm. GOME is a nadir-viewing instrument, while SCIAMACHY includes a nadir-viewing mode. Both have the capability to make measurements at the resolution and accuracy needed for application of the principles investigated in the present study. GOME is scheduled for launch on the European Space Agency's ERS 2 satellite in late 1994/early 1995, while SCIAMACHY will be a part of the Envisat 1 payload in the late 1990s. The simultaneous detection of cloud parameters will help considerably in trace gas retrievals for these instruments. For ozone in particular, the concentration peaks in the stratosphere (nominally at ~23 km), well above normal cloud altitudes. However, ozone in the troposphere makes a nonnegligible contribution to the total column density, one which may be growing as a result of anthropogenic activities. A major impetus for this study is the correction of ozone measurements in order to permit both better statistical evaluation of global ozone column measurements and determination of the climatology of tropospheric ozone.

In the ultraviolet and visible regions, incident light at different wavelengths penetrates to almost the same distance inside of clouds; the effective cloud top height does not depend strongly on wavelength. Thus measurements of the O_2 *A* and *B* bands are useful for 300- to 400-nm cloud top height detection, appropriate to measurements in Hartley and Huggins bands of O_3, as well as in the visible Chappuis bands. Both GOME and SCIAMACHY will be capable of detecting both cloud top height and cloud coverage with moderate accuracy when combined with appropriate atmospheric modeling capability. The remainder of this paper will discuss the cloud detection capability specifically in terms of GOME, but the discussion is equally applicable to SCIAMACHY nadir-viewing measurements.

In this study we calculate the dependence of the measured spectrum on the cloud top height and a cloud coverage parameter (specifically, the product of the fractional coverage times the cloud reflectivity, αr, divided by the scene-averaged albedo, γ) for several cases of instrument resolution, wavelength coverage, and cloud conditions. A minimization technique is applied in order to determine the range of values which correspond most closely to the measurement. The scene-averaged albedo can be determined independently by measurements out of the O_2 bands in order to determine αr. Complete determination of the fractional coverage currently depends on independent knowledge of either the cloud reflectivity or the ground albedo. In future work we hope to be able to demonstrate techniques for simultaneous retrieval of cloud reflectivity and ground albedo as well as cloud top height and cloud coverage with instruments of sufficient resolution and sensitivity. Such retrieval would remove the ambiguity in the coverage parameter and its dependence on climatological values of cloud top reflectivity and Earth albedo.

2. Radiative Transfer in the O_2 Absorption Region

Figure 2 shows the O_2 *A* and *B* spectral bands, calculated using the 1992 HITRAN database [*Rothman et al.*, 1992]. O_2 *A* and *B* have strong absorption around 13,143 cm^{-1} (761 nm) and 14,546 cm^{-1} (687 nm). (Note that wavelength, in nanometers, is the unit of choice for measurements by the satellite instruments, which are dispersive spectrometers. Line parameter listings are normally in cm^{-1}, since line shapes are appropriately described in a scale linear in energy.) A spectrometer with a spectral resolution of about 4.0 cm^{-1} (e.g., GOME) will have several spectral measure-

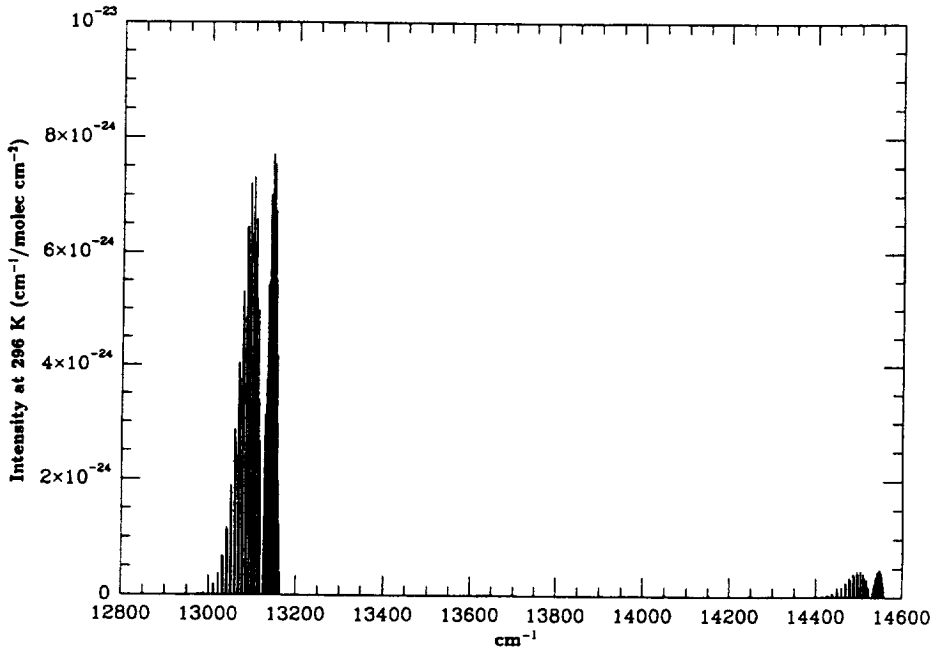

Figure 2. A stick spectrum showing the O_2 *A* and *B* band positions and intensities from the 1992 HITRAN database.

ments in the O_2 bands. The radiance measured in the satellite geometry by spectral channel j, neglecting scattering, is described by

$$I(j) = \sum_{i=1}^{N} \alpha_{ij} r_i \int f_j(\nu) F(\nu) \exp\left(-s\tau(\nu, h_i)\right) \frac{d\nu}{\Delta\nu}$$

$$+ \beta_j \left(1 - \sum_{i=1}^{N} r_i\right) \int f_j(\nu) F(\nu) \exp\left(-s\tau(\nu, 0)\right) \frac{d\nu}{\Delta\nu}, \quad (1)$$

where N is the number of different cloud top height types, α_{ij} is the cloud top reflectivity for cloud type i in spectral channel j, r_i is the coverage of type i cloud, $f_j(\nu)$ is the slit function of channel j, $F(\nu)$ is the solar spectrum, $\tau(\nu, h)$ is the optical depth between cloud top and satellite (proportional to total O_2 column amount above the cloud top), h_i is the top height of type i cloud, $\Delta\nu$ is the full spectral width at half maximum of the instrument, and β_j is the Earth's surface diffusive albedo. Here α_{ij} and β_j are assumed to be constant over the small spectral size of spectrometer channel considered here. The optical path factor s is $\sec(\theta) + \sec(\varphi)$. The cloud type definitions that we use correspond to those of LOWTRAN and MODTRAN [*Kneizys et al.*, 1988; *Berk et al.*, 1989]. The major effect of different cloud types (except for cirrus, as noted below) is to change the radiance level of the reflected radiation. From studies such as the MODTRAN calculations shown in Figure 1, we can assume that clouds are thick enough that solar light reflects at the cloud tops; this is the operational definition of "cloud top" in these studies. There are several caveats in this assumption. If a cloud layer is not sufficiently thick that determination of a cloud top height to the ~1-km accuracy aimed for in this study is possible, there will obviously be an ambiguity in the determination. Different cloud types may have bidirectional reflectance distribution functions (BRDFs) that differ sufficiently that the reflectance calculations at different viewing and solar zenith angles are significantly affected; this aspect of the problem is currently under investigation at the University of Bremen, Bremen, Germany, (J. Burrows, R. Spurr, and T. Kurosu, private communication, 1993). The effect of cirrus clouds on the determination of cloud parameters deserves, and will get, more attention than it has received in this study. Our current feeling is that optically thin cirrus will not present a significant problem; clouds that are partially transmitting have the same effect when averaged over the instrumental field of view as a partial coverage. Multiple Mie scattering inside of clouds may significantly affect the optical path; the size of this effect is currently being investigated at the University of Heidelberg, Heidelberg, Germany, with Monte Carlo multiple scattering calculations (H. Frank and U. Platt, private communication, 1993). This specifically includes an investigation into potential multiple scattering problems in cirrus. The effect of multiple scattering inside clouds may be the limiting factor in the general applicability of optical methods in cloud determinations. Radiance in the absence of absorption by O_2 or other gases (e.g., out of band), without scattering, is described as

$$I_0(j) = \gamma_j \int F(\nu) f_j(\nu) \frac{d\nu}{\Delta\nu}, \quad (2)$$

where

$$\gamma_j = \sum_{i=1}^{N} \alpha_{ij} r_i + \beta_j \left(1 - \sum_{i=1}^{N} r_i\right).$$

For GOME, $F(\nu)$ is determined from a priori information and on-board solar flux monitoring using a diffuser. Thus the

scene-averaged albedo γ_j out of band can be directly determined.

Scattering effects are considered below. In the above wavelength region, absorptions by gases other than O_2 are small compared with the dominant O_2 absorption; they can be safely neglected for cloud detection at the present level of accuracy. In the O_2 *A* and *B* bands, γ_j is interpolated using the spectrum near the O_2 *A* and *B* bands where there is no strong absorption. The slit function $f_j(\nu)$ is assumed to be triangular, because the spaceborne spectrometers we are considering have the same output slit (detector) size as the entrance slit. In the real measurements the slit function must, of course, be measured with high spectral resolution. The vertical profiles of O_2 number density and temperature are assumed to be well known. Optical depths $\tau(\nu, h)$ between the satellite orbit and each height are calculated with high accuracy using FASCODE 3 (G. P. Anderson and J. H. Chetwynd, private communication, 1992).

The measured values are convolutions of the slit function, $I_0(\nu)$, and the atmospheric transmittance. By analogy with *Fleig et al.* [1990] it is convenient to describe the convolution in terms of a parameter Q, defined in our case as

$$Q(j, h_i) = \int f_j(\nu) \exp(-s\tau(\nu, h_i)) \frac{d\nu}{\Delta\nu}. \quad (3)$$

The parameter $R(\nu_0, h_i)$, which is the ratio of satellite-measured radiation to solar input radiation, is then defined by the following, assuming $F(\nu)$ is constant within a spectrometer channel so that it can be taken outside of the integral in equations (1) and (2):

$$R(j, h_i, \alpha_{ij}r_i) = \frac{I(j)}{F(\nu)}$$

$$= \sum_{i=1}^{N} \alpha_{ij}r_i Q(j, h_i) + \beta_j\left(1 - \sum_{i=1}^{N} r_i\right)Q(j, 0)$$

$$= \sum_{i=1}^{N} \alpha_{ij}r_i Q(j, h_i) + \left(\gamma_j - \sum_{i=1}^{N} \alpha_{ij}r_i\right)Q(j, 0) \quad (4)$$

3. Determination of Cloud Top Height and Related Parameters

3.1. Grid Search Least Squares Fit

Cloud parameters are determined by least squares fitting to calculated radiance ratios. We assume there is no a priori information on h_i and $\alpha_{ij}r_i$ in equation (4) and use a grid search method to search the parameter space of h_i, $\alpha_{ij}r_i$ to minimize the variance. The quantity χ^2 is defined as

$$\chi^2 = \sum_{j=1}^{M} \left(\frac{R_{obs}(j, h_i, \alpha_{ij}r_i) - R_{calc}(j, h_i, \alpha_{ij}r_i)}{R_{obs}(j, h_i, \alpha_{ij}r_i)}\right)^2 \Big/ M, \quad (5)$$

where the R_{obs} are R values from measurement and dividing by the measured solar calibration, the R_{calc} are R values for grid searching to determine h_i and $\alpha_i r_i$, and M is the number of spectrometer channels in the O_2 *A* and *B* band regions (α_{ij} and γ_j are assumed to be constant within each O_2 band).

Here χ^2 is not divided by the error value σ^2, because σ^2 is almost the same for each spectrometer channel. The σ^2 attained in the measurements determines the contour describing the level of accuracy achieved in cloud parameters, as shown below. The ranges of r_i and h_i are between 0 and 1 and between 0 and 10 km, respectively. In the present work, grid searching is used rather than a continuous nonlinear least squares technique, since we are evaluating χ^2 over a space of variables with discrete values. No particular attempt has yet been made to optimize the technique; rather, we perform complete evaluations of χ^2 over the range of coverage variable at ~0.01 resolution and over cloud-top height at ~0.1-km resolution. Because the ranges and resolutions are limited, the computation time necessary to search the resulting tables for minimum values is not a serious concern.

For both cloud top height and cloud coverage detection, optical depth is an important concern. If the optical thickness is too large, it becomes impossible to detect low cloud accurately, because the Q values become too small. If the optical depth is too small, the transmittance is an almost linear function of $\alpha_i r_i$ and optical depth, and it becomes impossible to distinguish cloud height from cloud coverage. If the difference of integrated optical depth between channels is too small, it is also impossible to distinguish cloud height from cloud coverage. Thus for cloud parameter detection, both the optical depth values and contrast between channels are important.

Figures 3a and 3b show calculated optical depths for a range of typical cloud top height scenarios using FASCODE 3: Figure 3a for the O_2 *A* band and Figure 3b for the O_2 *B* band. Around this spectral region the GOME resolution is about 4.0 cm^{-1}. The optical depths change substantially in this region, so calculations must be done with high spectral resolution. When the spectral resolution is much wider than the oxygen spectral lines in the bands, the measured optical depth is a highly averaged or smeared-out quantity and its variation with detector channel is small. Therefore higher spectral resolution improves cloud detection. Figure 4 shows Q values for several *A* and *B* band channels in the case of $\Delta\nu$ = 4.0 cm^{-1} and s = 2.0. The center positions of the channels are 13,132, 13,144, 14,539, and 14,551 cm^{-1}.

We have calculated the variation of χ^2 in the space of cloud top height versus the coverage parameter $\alpha_1 r_1/\gamma$ for representative cases of instrumental resolution, number of measuring channels, and cloud top heights. The results are given in Figure 5 as contour plots showing the logarithm of χ^2; these plots are intended to give a visual sense of how well a minimization scheme (such as the grid search employed here) will succeed in the independent determination of cloud top height and the coverage parameter. Figure 5a shows the variation of χ^2 for a typical GOME case, $\Delta\nu$ = 4.0 cm^{-1}, N = 1, and M = 12, with a cloud layer at 5 km and a coverage parameter of $\alpha_1 r_1/\gamma$ = 0.5 (50% coverage when the cloud top reflectivity is equal to the Earth albedo). The twelve spectrometer channels chosen consist of seven O_2 *A* and five O_2 *B* band measurements. The center positions of the channels are 13,132, 13,136, 13,140, ... 13,156 cm^{-1} for the O_2 *A* band and 14,539, 14,543, 14,547, ... 14,555 cm^{-1} for the O_2 *B* band. N = 1 is assumed because there will most often be one cloud type within the IFOV. Figure 5b compares this case with that of higher spectral resolution, $\Delta\nu$ = 0.2 cm^{-1}. The center positions of the channels are 13,150.6, 13,150.8, 13,151.0, ... 13,151.8 cm^{-1} for the O_2 *A* band and

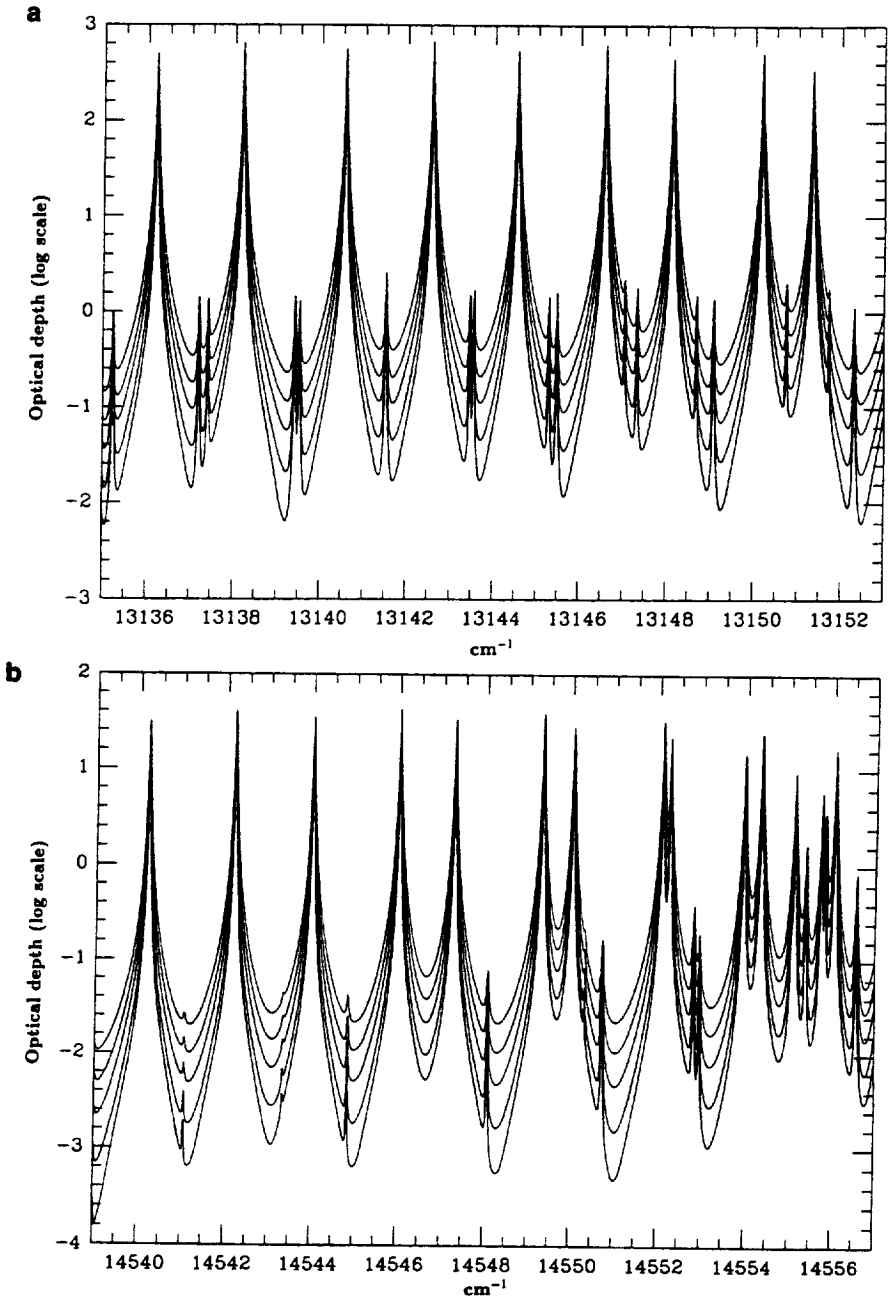

Figure 3. Calculated nadir optical depths for the visible bands of O_2 between space and the altitudes 0 (top), 2, 4, 6, and 8 (bottom) km: (a) O_2 *A* band and (b) O_2 *B* band.

14,555.1, 14,555.3, 14,555.5, . . . 14,555.9 cm^{-1} for the O_2 *B* band. Figures 5c and 5d show cases of a lower cloud top height (2 km) with $\Delta\nu = 4.0\ cm^{-1}$ and $\Delta\nu = 0.20\ cm^{-1}$ as in Figures 5a and 5b. Figure 5c has several minima, but the proper one is significantly deeper; if the measurement accuracy is very good, the solution is unique. For the lower-altitude cloud and lower spectral resolution there are extended trough regions in the variation of χ^2 with cloud height versus cloud coverage. This indicates that high accuracy is required in order to get a unique solution for cloud coverage. Generally, higher resolution is better for cloud detection, but there may be a tradeoff here between resolution and signal-to-noise ratio. However, as Figure 5c shows, cloud height is easily determined. For total ozone retrieval, the coverage of low cloud may not be critically important. From the hyperbolic shapes of the contours in Figure 5c we may conclude that for low cloud top height and low cloud coverage, the cloud top height is not accurately determined. On the other hand, for the higher cloud top height and higher coverage case, both height and coverage detection accuracy is high. There is a basic tradeoff in cloud coverage versus cloud height information that stems from the fact that the most basic accurate information obtained by measurements in the O_2 bands, which is that of absorption in the optically thin portions of the bands, gives the average transmission or, equivalently, path length through the atmosphere. Any overestimate of cloud coverage thus implies an underestimate in cloud top height. Figures 5e and 5f are moderate- and

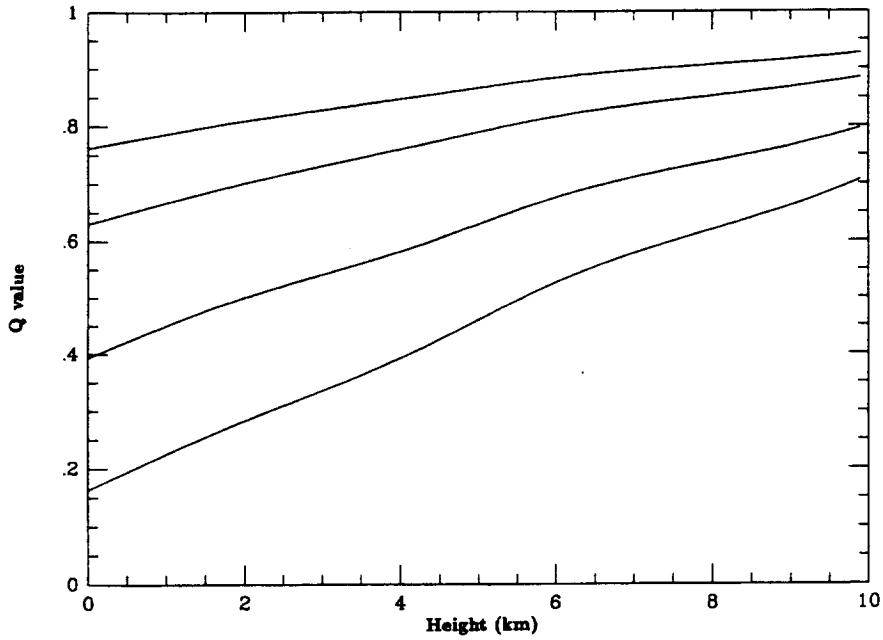

Figure 4. Q values (convolutions of the instrument slit function and the atmospheric transmittance) for O_2 A and B band channels with center positions of 14,539, 14,551, 13,132, and 13,144 cm^{-1} (top to bottom) for instrument resolution $\Delta\nu = 4.0$ cm^{-1}.

high-resolution cases of $M = 2$, $r_1 = 0.5$, and $h_1 = 5$ km. These are calculated in order to compare results obtained with differing numbers of measurement channels. The resolution is 4.0 cm^{-1}, and the center wavelengths of the channels are 13,140 and 14,547 cm^{-1} for Figure 5e; the resolution is 0.2 cm^{-1}, and the center wavelengths of the channels are 13,151.0 and 14,555.5 cm^{-1} for Figure 5f. Comparison of Figures 5e and 5a shows clearly that the use of a large number of spectral channels greatly improves the accuracy for moderate (i.e., GOME) resolution. However, for higher spectral resolution, a small number of spectral channels is adequate, as shown by Figure 5f.

The above method determines $\alpha_1 r_1$. By using interpolated values of γ_j, $\beta(1 - r_1)$ may also be determined. If appropriate a priori data for β are available, α_1 and r_1 may be determined individually. From the α_1 value it may be possible to estimate the cloud depth. This study is for one cloud type and cloud top height, but the determination of two or more cloud layers within the IFOV may be possible with the use of a grid search in more than four dimensions.

3.2. Accuracy Requirements and Error Estimation

The desired uniqueness of solution determines the accuracy requirement. As mentioned above, for lower-height cloud detection, high accuracy is required. This statement can be quantified in a typical example. Figure 6 indicates the $|\chi|$ variation for $N = 1$, $M = 12$, $r_1 = 0.5$, $h_1 = 5$ km, and $\Delta\nu = 4.0$ cm^{-1}. As before, the twelve spectrometer channels include seven in the A band and five in the B band. The central contour, shown as a bold line, corresponds to the limit of ±1% measurement error about the central minimum. This contour corresponds to ±20% error in cloud coverage and ±2 km in cloud top height. If the cloud coverage detection accuracy is required to be ±20%, the sum of measurement error and model calculation error must be less than 1%. The anticipated random errors in measurements are small enough to allow precise solution (the modeled signal-to-noise ratio for GOME is ~1000), but the forward model calculations in the present study have uncertainties which may cause substantial systematic error. It is possible to detect the area surrounded by the contour line in Figure 6 when the systematic errors are 1%. This area indicates the correlation between cloud top and cloud coverage and should be useful for removing cloud effects in total ozone determinations. To separate cloud top height and coverage accurately, higher spectral resolution is required. The significant systematic error sources are discussed below. These items are expected to be corrected by adequate calibration.

Measurement errors. Because R is a ratio, that of the Earth measurement to the solar measurement, the systematic radiance errors of the instrument response largely cancel. The capability for relative radiance measurements should be better than 1%.

Model calculation errors include the items listed below. The first two items affect both γ and Q value calculations. The third affects γ, and the others affect the Q values.

Single and multiple scattering effects. As discussed below, scattering effects must be included for accurate cloud determination.

Effects of other gases. There are strong H_2O bands between the O_2 A and B bands, but they do not affect the O_2 A and B bands significantly. In FASCODE 3 studies we find the calculated optical depth due to other gases within the O_2 A and B band limits to be negligible.

Scene-averaged albedo interpolation in the O_2 A and B bands. The solar spectrum can be assumed to decrease linearly around the O_2 A and B bands. The error caused by interpolation is negligibly small.

Line parameter database. As discussed below, the line

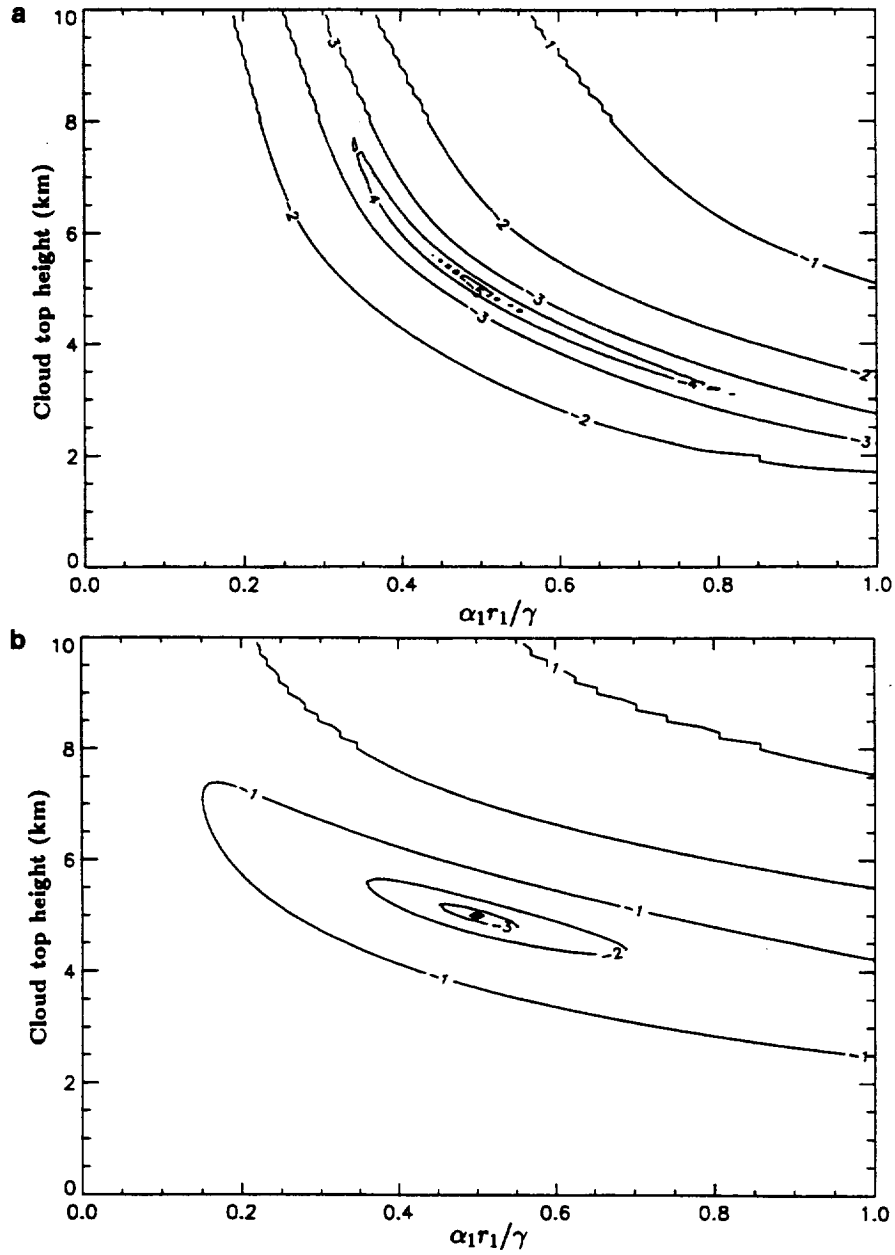

Figure 5. The χ^2 variation in log scale, where χ^2 is the sum of squares of radiance ratio deviations, which is minimized in the fitting process to determine cloud-top height and coverage (see text for details). Estimated uncertainties are not included in χ^2; rather, the uncertainties determine which contour is applicable. Results are presented for several case studies illustrating differences due to the number of measurement channels, M; the height of the cloud layer, h; and the instrument resolution, $\Delta\nu$. The cloud coverage parameter, $\alpha_1 r_1/\gamma = 0.5$, includes a ratio of albedos, as explained in the text. (a) $M = 12$, $\alpha_1 r_1/\gamma = 0.5$, $h = 5$ km, and $\Delta\nu = 4.0$ cm^{-1}; (b) $M = 12$, $\alpha_1 r_1/\gamma = 0.5$, $h = 5$ km, and $\Delta\nu = 0.2$ cm^{-1}; (c) $M = 12$, $\alpha_1 r_1/\gamma = 0.5$, $h = 2$ km, and $\Delta\nu = 4.0$ cm^{-1}; (d) $M = 12$, $\alpha_1 r_1/\gamma = 0.5$, $h = 2$ km, and $\Delta\nu = 0.2$ cm^{-1}; (e) $M = 2$, $\alpha_1 r_1/\gamma = 0.5$, $h = 5$ km, and $\Delta\nu = 4.0$ cm^{-1}; and (f) $M = 2$, $\alpha_1 r_1/\gamma = 0.5$, $h = 5$ km, and $\Delta\nu = 0.2$ cm^{-1}.

intensities and pressure-broadening coefficients must be determined to high accuracy compared to that of the desired detection accuracy, or an appropriate in-flight characterization and calibration scheme must be used.

Temperature profiles. According to the *Wark and Mercer* [1965] absorptance calculations, the effect of temperature profile ambiguity on optical depth calculations in these bands (at low spectral resolution) is less than 1%. A calculational check of the temperature dependences for selected individual line strengths confirms this conclusion for the stronger lines in the *A* band.

Slit function. The absolute value of spectral responsivity is not a concern in this method. The shape of the modeled instrument slit function is, however, extremely important.

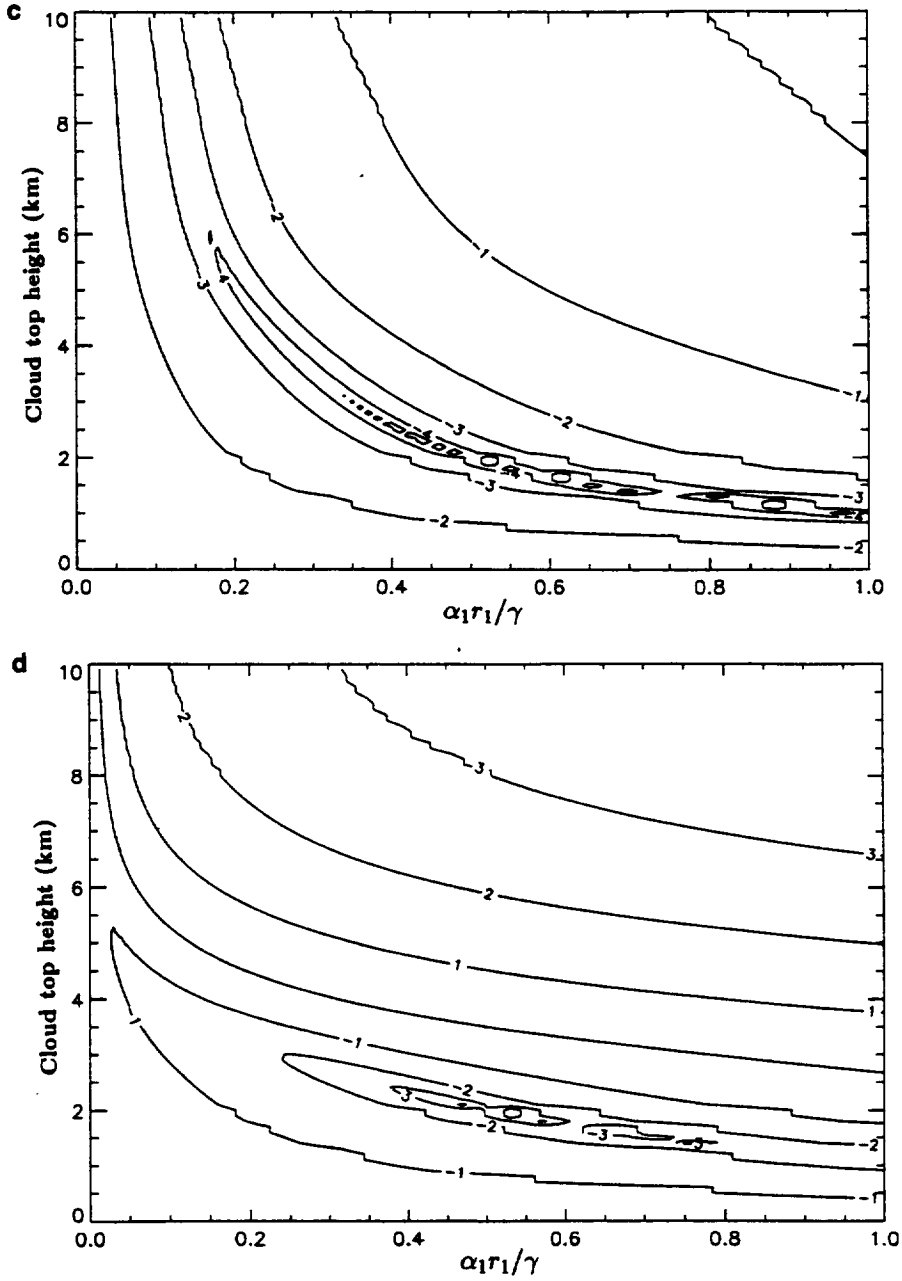

Figure 5. (continued)

Extra absorption inside clouds. The estimated cloud top is always below the actual cloud top because of the extra absorption inside the clouds [cf. *Saiedy et al.*, 1967]. For our present purposes of correcting for ozone and other trace species, the important consideration is whether multiple Mie scattering within the cloud, of light that is eventually scattered back out into the instrument field of view, is a severe limitation. If the major effect of penetration into the cloud is replacement of the cloud top by a diffuse scattering surface at a lower altitude, then the technique is perfectly suited for such correction. This problem is not thought to be serious at the present (1 km) level of accuracy, but the previously mentioned calculations underway at the Universities of Bremen and Heidelberg will provide more definitive answers to this concern.

3.3. Algorithm and Operation

Before launch, the optical depths necessary to determine Q values are calculated for several temperature profile scenarios at a resolution of 0.001 cm^{-1}, and the slit function is measured at similarly high resolution. Look-up tables in terms of optical depth are then prepared at intervals of ~0.1 km.

After launch, the operational software searches for the minimum χ^2 and estimates the cloud top heights and coverage. The increments for heights and coverages are ~0.1 km and 1%, respectively. The default number of different cloud types within the IFOV, N, is 1. Thermal differences between ground calibration and orbit, including thermal cycling of the instrument through the satellite orbit, may cause the center wavelengths for the measurement channels to change. Thus

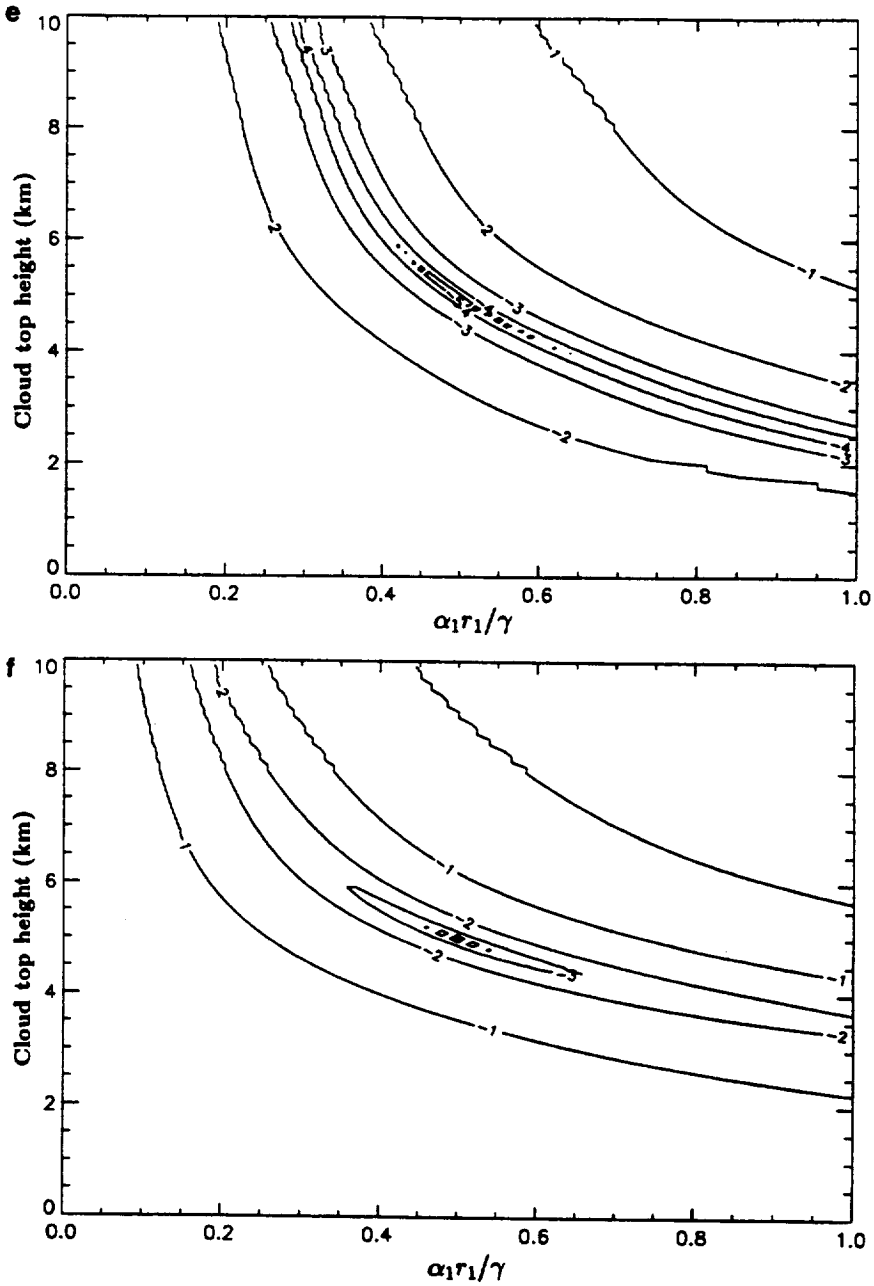

Figure 5. (continued)

Q values must be recalculated after the on-board wavelength calibration.

4. Discussion

4.1. Cloud Reflectivity and Earth Surface Albedo

Both $\alpha_1 r_1$ and $\beta(1 - r_1)$ are determined in this method. As mentioned above, in order to estimate cloud coverage and cloud reflectivity we will, as our initial working algorithm, employ an a priori Earth surface albedo table which includes both geographical and seasonal information. The source of the albedo database used to create this table is the ETOPO5 data set (NOAA/National Geophysical Data Center, Boulder, Colorado). More sophisticated future versions of the algorithm should exploit the radiance data from the satellite instrument itself further. GOME and SCIAMACHY each measure the scene-averaged albedo, γ_j, from 240 nm to 790 nm, including measurements in wide spectral regions where atmospheric gas absorptions are small. As β has substantially stronger wavelength dependence than α_1, this scene-averaged albedo information should help to further separate surface albedo and cloud coverage. Additionally, cloud scattering studies currently underway at the University of Bremen should provide invaluable information on cloud top reflection coefficients coupled to cloud type and altitude (J. Burrows, R. Spurr, and T. Kurosu, private communication, 1993). Thus we anticipate that the proper combination of the satellite radiance measurements and cloud scattering studies will provide the necessary leverage to separate albedo, cloud reflectivity, and coverage to high accuracy.

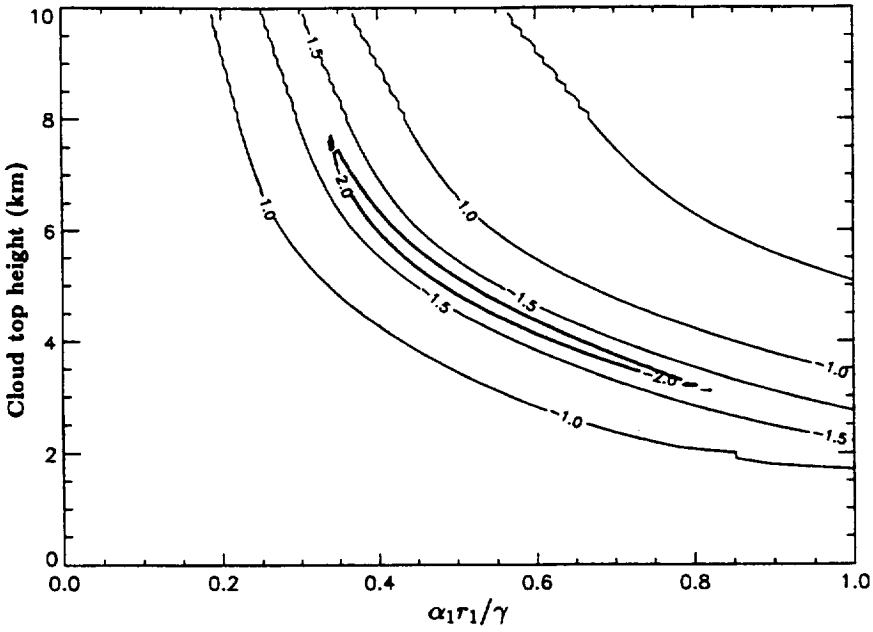

Figure 6. The $|\chi|$ variation in log scale; $M = 12$, $\alpha_1 r_1/\gamma = 0.5$, $h = 5$ km, and $\Delta\nu = 4.0\ \text{cm}^{-1}$.

4.2. Scattering Effects

Even though Rayleigh scattering is small in the visible O_2 absorption region compared with the ultraviolet region covered by GOME, its effect in the atmospheric path must be considered for accurate cloud detection. Single-scattering radiance calculations do not depend on either the cloud top reflectivity or Earth surface albedo, but when multiple scattering is included, there is a strong dependence on both. Therefore to estimate scattering effects, a priori data of α and β are necessary. The input radiance $I_s(j)$, including scattering effects is

$$I_s(j) = r_1 \int f_j(\nu)(\alpha_1 F(\nu) T(s, \nu, h_1) + S(\nu, h_1, \alpha_1)) \frac{d\nu}{\Delta\nu} + (1 - r_1) \int f_j(\nu)(\beta F(\nu) T(s, \nu, 0) + S(\nu, 0, \beta)) \frac{d\nu}{\Delta\nu}, \quad (6)$$

where $T(s, \nu, h_1)$ is the transmittance and $S(\nu, h_1, x)$ is the single and multiple scattered radiance.

In general, reflectivity of cloud tops is high in the visible region. Therefore scattering effects are relatively small and radiance calculation errors are small. Out of the O_2 absorption region the scattering affects γ_j estimation. The difference between the radiance not considering scattering, $I_0(j)$, and the radiance considering scattering, $I_s(j)$, is less than 1% when $\beta = 0.3$, because the back-scattering ratio to the zenith is almost equal to the Earth surface diffusive reflectivity (note that geometry must be carefully considered when evaluating the importance of Rayleigh scattering in non-GOME geometries, though). A 10% ambiguity of a priori β in the $S(\nu, 0, \beta(\nu))$ calculation causes an error of a few percent in $I_s(j)$. Therefore the γ_j error caused by scattering is less than a few percent.

In the O_2 absorption region, scattering affects Q value calculations. Because the optical path, including the O_2 column density, is multiplied by scattering, the effective optical depth calculation depends on α and β. For low β, scattering effects on Q value estimation are relatively high. Therefore ambiguity in β might cause a serious error, and a priori data on β are important for estimation of scattering effects.

4.3. Spectral Band Database

The line parameters for these bands necessary to perform the quantitative analysis proposed here are included in the HITRAN and GEISA databases, derived from measurements by *Miller et al.* [1969] and *Giver et al.* [1974]. The line positions are well known for both bands. The intensities for the O_2 *B* band are well known (to better than 2%), but for the O_2 *A* band they are known to only 4%. For both bands, considerable work is necessary on line-broadening parameters. Pressure broadening is the chief determinant of line widths and thus of radiative transfer through the bands below about 8 km in the Earth's atmosphere.

O_2 broadening of the O_2 *A* band lines at room temperature is known to about 15%. No N_2 or air broadening studies have been made, and no temperature dependencies have been measured. The values used in the catalogs for O_2 *A* band broadening are actually the more accurately determined O_2 *B* band width parameters (see below), a substitution made on the presumption that the vibrational dependence of pressure-broadening coefficients is negligible. Studies for the magnetic dipole-allowed microwave rotationless and far infrared rotational lines [*Chance et al.*, 1991] show that (1) air broadening can be substantially different from O_2 broadening, (2) temperature dependence can differ substantially from the suggested hard sphere value of $T^{-0.5}$, and (3) state-to-state dependence, even when sharing a common lower state, can vary substantially between the microwave rotationless and far infrared rotational lines. This fact, plus experience with rotational and vibrational comparisons for other molecules, suggests that the O_2 *A* and *B* band broadening parameters may differ at a level that is important for detailed geophysical studies. The cumulative error in the

widths under atmospheric conditions, considering all of these factors, may well exceed 25%.

The O_2 *B* band widths are in somewhat better shape, as they were performed at a later time using more fully developed techniques, but there are still only widths (albeit good to 2–3%) for room temperature O_2 broadening. Broadening values for this band also need to be expanded to include air broadening and low temperatures to be useful for realistic geophysical analysis.

Q value calculations depend directly on line intensities; 2% error in the intensities corresponds to a few percent error in *Q* value calculation. Although GOME and SCIAMACHY have a ~4.0-cm^{-1} resolution, wider than the O_2 *A* and *B* band line widths, the *Q* values are sensitive to pressure broadening line widths both because the pressure broadening affects line saturation except in the optically thin limit and because the slit function is triangular and the *Q* values are proportional to convolutions of the line shape and the slit function. The exact sensitivity depends on the line center location in each channel. A 3% error in line width generally corresponds to less than a few percent error in *Q* value calculation.

Detailed sensitivity analyses to assess the precise effect of line parameter uncertainties on the cloud parameter retrieval accuracy are planned for the next phase of this investigation. This will include more detailed dependence of *Q* values on line parameters and on the measurement channel placement with respect to the peaks of the O_2 lines. Simple radiative transfer considerations imply that the determination of the scene average path length is a process that depends primarily on the optically thin components of the observations. We expect that at the first level of approximation, the knowledge of this quantity depends linearly upon the knowledge of the line intensities. We also expect that in order to be able to overcome potentially large systematic effects due to uncertainties in line parameters, an in-flight characterization and calibration scheme will need to be devised in order to effectively utilize any data other than optically thin absorption measurements.

5. Conclusions

GOME and SCIAMACHY have several channels of varying, but moderate, optical depth in the O_2 *A* and *B* band regions. We have proposed an operational method for determination of cloud parameters that has the potential to produce accurate results with minimal computation time. This method has been primarily developed as a contribution to the development of the GOME and SCIAMACHY programs. It has the potential to be effective for other satellite-based measurement programs as well, including geostationary meteorological satellite observations that employ larger IFOVs and longer integration times compared with the Sun synchronous satellite observations of GOME and SCIAMACHY. For accurate detection, further studies of spectral band parameters, scattering effects, and Earth albedo studies are required. Scattering studies currently underway include those of cloud-top reflection coefficients (BRDFs) coupled to cloud type and altitude (J. Burrows, R. Spurr, and T. Kurosu, private communication, 1993) and the Monte Carlo multiple scattering calculations of scattering inside clouds (H. Frank and U. Platt, private communication, 1993).

Acknowledgments. This research was supported by NASA grant NAGW-2541.

References

Berk, A., L. S. Bernstein, and D. C. Robertson, MODTRAN: A moderate resolution model for LOWTRAN 7, *AFGL Tech. Rep., 89-0122*, 1–42, 1989.

Chance, K. V., W. A. Traub, K. W. Jucks, and D. G. Johnson, On the use of O_2 spin-rotation lines for elevation angle calibration of atmospheric thermal emission spectra, *Int. J. Infrared Millimeter Waves, 12*, 581–588, 1991.

Fisher, J., and H. Grassl, Detection of cloud-top height from backscattered radiances within the oxygen A band, 1, Theoretical study, *J. Appl. Meteorol., 30*, 1245–1259, 1991.

Fisher, J., W. Cordes, A. Schmitz-Peiffer, W. Renger, and P. Mörl, Detection of cloud-top height from backscattered radiances within the oxygen A band, 2, Measurements, *J. Appl. Meteorol., 30*, 1260–1267, 1991.

Fleig, A. J., R. D. McPeters, P. K. Bhartia, B. M. Schlesinger, R. P. Cebula, K. F. Klenk, and D. F. Heath, Nimbus 7 solar backscatter ultraviolet (SBUV) ozone products user's guide, *NASA Ref. Publ., 1234*, 1–128, 1990.

Giver, L. P., R. W. Boese, and J. H. Miller, Intensity measurements, self-broadening coefficients, and rotational intensity distribution for lines of the oxygen B band at 6880 Å, *J. Quant. Spectrosc. Radiat. Transfer, 14*, 793–802, 1974.

Kneizys, F. X., E. P. Shettle, L. W. Abreu, J. H. Chetwynd, G. P. Anderson, W. O. Gallery, J. E. A. Selby, and S. A. Clough, Users guide to LOWTRAN 7, *AFGL Tech. Rep., 88-0177*, 1–137, 1988.

Miller, J. H., R. W. Boese, and L. P. Giver, Intensity measurements and rotational intensity distribution for the oxygen A band, *J. Quant. Spectrosc. Radiat. Transfer, 9*, 1507–1517, 1969.

Rothman, L. S., et al., The HITRAN molecular database editions of 1991 and 1992, *J. Quant. Spectrosc. Radiat. Transfer, 14*, 469–507, 1992.

Saiedy, F., H. Jacobowitz, and D. Q. Wark, On cloud-top determination from Gemini-5, *J. Atmos. Sci., 24*, 63–69, 1967.

Wark, D. G., and D. M. Mercer, Absorption in the atmosphere by the oxygen "A" band, *Appl. Opt., 4*, 839–844, 1965.

Yamamoto, G., and D. Q. Wark, Discussion of the letter by R. A. Hanel, "Determination of cloud altitude from a satellite," *J. Geophys. Res., 66*, 3596, 1961.

A. Kuze and K. V. Chance, Harvard-Smithsonian Center for Astrophysics, 60 Garden Street, Cambridge, MA 02138.

(Received June 1, 1993; revised March 24, 1994;
accepted April 20, 1994.)

Satellite measurements of halogen oxides by the Global Ozone Monitoring Experiment, GOME, on ERS2: Distribution of BrO and comparison with groundbased observations

E. Hegels*, P.J. Crutzen, T. Klüpfel, D. Perner
Max-Planck-Institut für Chemie, Saarstr. 23, 55122 Mainz, Germany

J.P. Burrows, A. Ladstätter-Weißenmayer
Inst. für Fernerkundung, Univ. Bremen, Postfach 330440, 28334 Bremen, Germany

M. Eisinger
Alfred Wegener Institut, Postfach 600148, 14401 Potsdam, Germany

J. Callies, A. Hahne
ESA-ESTEC, LRX, Keplerlaan 1, Noordwijk, The Netherlands

K. Chance
Harvard-Smithonian Center for Astrophysics, Cambridge MA, U.S.A.

U. Platt
Inst. Umweltphysik, Univ. Heidelberg, Im Neuenheimer Feld 366, 69120 Heidelberg, Germany

W. Balzer
DLR-DFD, 82234 Weßling, Germany

Abstract. ERS2 based GOME provides UV-VIS-spectra of nadir scattered sunlight. The spectral observations yielded column data of OClO and BrO besides those of ozone and NO_2. The observations of stratospheric OClO and BrO at solar zenith angles of 80° and higher in polar regions are unambiguous because the long optical paths give rise to strong absorptions. The vertical column for BrO in the equatorial region is found to be $(3.0 \pm 1.5) \times 10^{13}$ molec/cm^2 which amounts to 16 ppt in the stratosphere. GOME data are compared to a number of groundbased differential optical spectroscopy observations of BrO by zenith scattered sunlight at Søndre Strømfjord, Greenland. Consequences for ozone depletion are discussed.

Introduction

Soon after the significance of chlorine as a sink for stratospheric ozone, O_3, became clear, the potential for O_3 depletion by bromine was pointed out by Watson, 1975 and Wofsy et al., 1975. Yung et al., 1980 and McElroy et al., 1986 recognized the synergistic coupling between bromine monoxide, BrO and chlorine monoxide, ClO, to destroy ozone. About half of this net reaction leads to ozone loss. Under conditions of high ClO concentrations like during the antarctic ozone hole formation it may account for 15 to 30 % of the ozone loss in the polar stratospheric vortex (Jones et al., 1989, Anderson et al., 1990, Solomon et al., 1990).

Under normal conditions the majority of inorganic chlorine in the stratosphere is tied up in relatively long lived reservoirs, HCl and $ClONO_2$, and the ClO concentrations are low. Yet the photolysis lifetimes of the bromine reservoirs, HOBr and $BrONO_2$, are short resulting in considerable amounts of daytime BrO, a reactive bromine species. As a result of this partitioning, bromine is much more efficient than chlorine on a per atom basis at destroying ozone (WMO/UNEP, 1995). BrO in the stratosphere has been detected before by remote spectroscopy (Caroll et al., 1989; Roth, 1992; Richter et al.,1996 and references therein) as well as by in situ measurements (Brune et al., 1989; Toohey et al., 1990). BrO is considered mainly to regenerate Br or Br_2 by reactions (1)-(3). The BrO dimer (Br_2O_2) is less important than the ClO dimer (Cl_2O_2).

$$BrO + BrO \rightarrow Br + Br + O_2 \quad (1)$$
$$\rightarrow Br_2 + O_2 \quad (2)$$
$$Br_2 + h\nu \rightarrow Br + Br \quad (3)$$

Ozone is destroyed by reaction (4) and in addition the reaction of HO_2 and BrO (5) leads to further destruction of O_3.

$$Br + O_3 \rightarrow BrO + O_2 \quad (4)$$
$$HO_2 + BrO \rightarrow HOBr + O_2 \quad (5)$$
$$HOBr + h\nu \rightarrow Br + OH \quad (6)$$

At midlatitude the lower stratospheric ozone is consumed via this reaction at a rate comparable to or even exceeding that of chlorine alone (Poulet et al., 1992; Avallone et al., 1993; Garcia and Solomon, 1993).

Experimental and Results

GOME comprises four spectrometers observing the region 240-790 nm simultaneously and having 4 diode array detectors. In total 3586 spectral measurements are made enabling the differential optical absorption technique, DOAS, (Perner et al., 1991) to be used for constituent retrieval. The spatial resolution is variable from

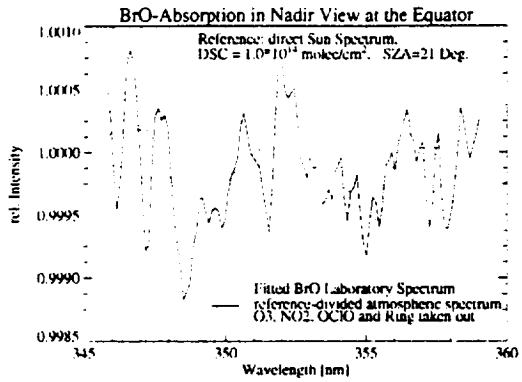

Figure 1. *Differential absorption for BrO in the sum of 100 spectra at the Equator (114° W, 21° SZA) at day 950907, direct sun reference. The two absorption bands of the BrO present an example for the precision reached so far. The strength of the fitted laboratory BrO absorption spectrum corresponds to* $8 \times 10^{13} molec/cm^2$.

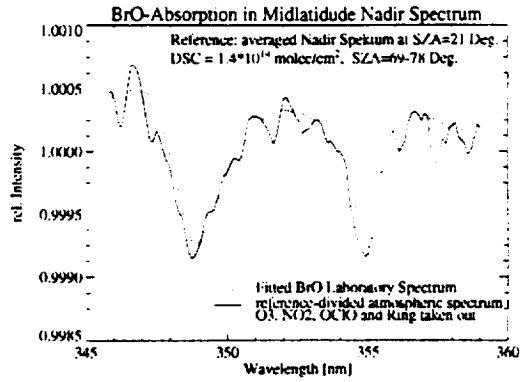

Figure 2. *Differential slant column absorptions of BrO are considerable more precise when a sum of 100 spectra at 60° SZA at southern midlatitudes is Fraunhofer corrected by the sum of the 100 spectra at 21° SZA (Fig. 1) of the same orbit. The laboratory BrO absorption spectrum shown corresponds in strength to the retrieved value.*

40×40 to 40×320 km^2. Full coverage of the longitudinal distribution is reached in about 3 days for the largest swath width. GOME flies on ERS2 in a polar sun synchronous orbit with a period of about 100 minutes.

Direct sun reference spectra are measured daily via a scattering plate. Figure 1 shows the differential absorption spectrum of BrO obtained from the division of 100 spectra at a solar zenith angle, SZA of 21° and the extra-terrestrial solar spectrum. Up to seven spectra can be fitted by a simultaneous nonlinear multiparameter procedure to the nadir spectra. In figure 1 and in figure 2 the residual absorption, having removed O_3, O_4, NO_2, OClO and Ring-spectrum, is plotted together with a BrO laboratory spectrum. The two absorption bands of the BrO are discernible.

The average spectrum for about 21° SZA contains 8×10^{13} molec/cm^2 which amounts to a vertical column of $(3.0 \pm 1.5) \times 10^{13}$ molec/cm^2 assuming that most of the light is scattered in the troposphere. The differential absorption cross section was 7.9×10^{-18} cm^2 molec^{-1} (223 K) at 355 nm and the spectral resolution 0.6 nm. A stratospheric mixing ratio of 14 ppt or 16 ppt is derived assuming a homogeneous distribution throughout the stratosphere starting from 16 or 17 km, respectively, assuming there is no BrO in the troposphere.

The larger high frequency structure when using the sun reference in the background noise as compared with that for example in a spectrum which is obtained by dividing the sum of 100 spectra at 60° SZA at southern midlatitudes by the sum of the 100 spectra at 21° SZA (Fig. 2) is not yet fully understood but is most likely due to limitations in the measured Ring reference spectra.

OClO was also identified and measured by its bands at 367, 376 and 385 nm (see also Burrows et al., 1996). For OClO the differential absorption cross section of 1.05×10^{-17} cm^2 molec^{-1} (223 K) at 376 nm was used. NO_2 slant columns, SCs, were retrieved and tests have shown that the retrieved amounts of BrO and NO_2 were independent of each other. Measurements around the globe of BrO, NO_2 and OClO (Fig.3) in September show high NO_2 in the northern areas and lower values at the south pole. BrO is fairly symmetrically distributed while no OClO is detected except in the vortex area around the south pole. Figure 4 shows the situation a month later. The northern NO_2 shown at sunrise has already diminished due to N_2O_5 formation at night while NO_2 at the south pole has somewhat recovered. Partly as consequence of the now enhanced $ClONO_2$ formation OClO has decreased and in the north sporadic OClO signals indicate the start of chlorine activation. BrO is diminished in southern hemisphere at large solar zenith angles most likely due to the lack of ozone in the region where most of the bromine is situated and partly due to the $BrONO_2$ formation. The positive values of OClO outside of the polar vortex require furter analysis.

Validation

From 950727 to 950808 remote sensing experiments of zenith scattered sun light were performed in Greenland by groundbased DOAS (GDOAS). BrO was evaluated and compared to the GOME data. Overpasses by ERS2 at Søndre Strømfjord, SS, during that period were at $\sim 88°$ SZA. In Table 1 the SC densities of BrO as measured by the nadir and by the zenith observations are given. The orbits of GOME with respect to SS are sometimes quite close and sometimes several hundred km to the east or west.

On day 950728 the orbit is quite close to SS. GDOAS shows higher values which might be due to tropospheric BrO which was recognized by GDOAS unambiguously around noon every day until 950804. On day 950729 the orbit went over the ice cap to the east of SS. GOME in-

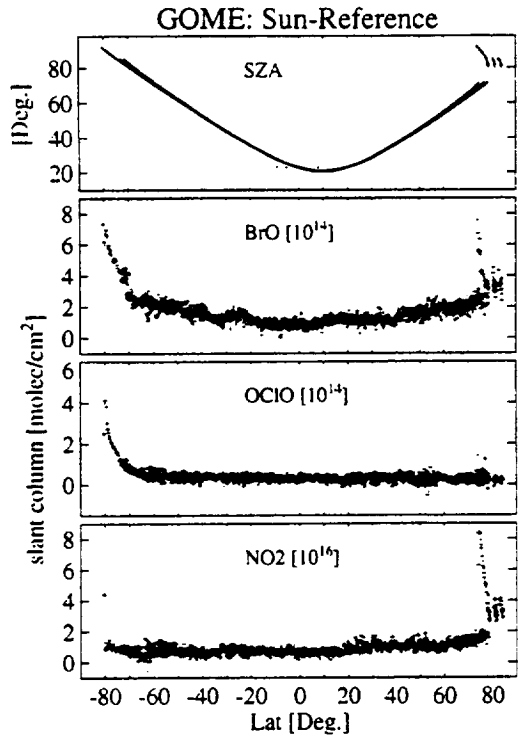

Figure 3. *Slant column of BrO, OClO and NO_2 and solar zenith angle as function of latitude of an orbit crossing the equator at 114 ° W at day 950907 (sun reference from 950905).*

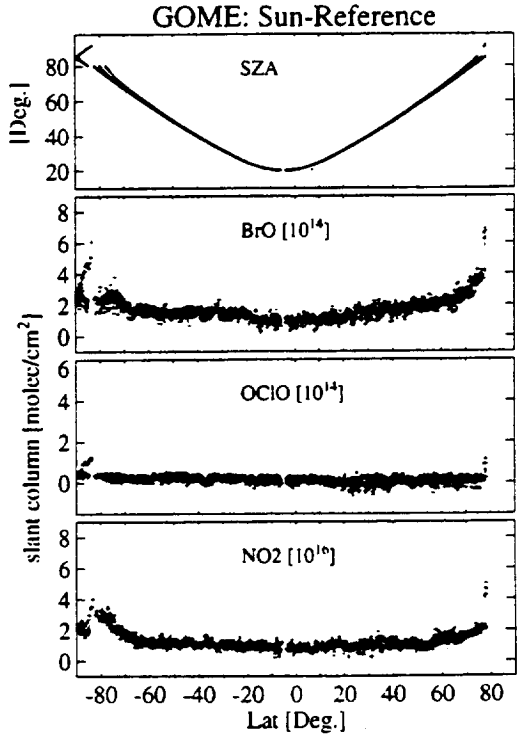

Figure 4. *Slant column of BrO, OClO and NO_2 and solar zenith angle as function of latitude of an orbit crossing the equator at 114 ° W at day 951012, (sun reference from 951012).*

dicates some variability but the agreement is fair. Day 950730 the orbit went over the David Street close to Canada and GDOAS still being influenced by tropospheric BrO shows the highest values about twice as high as those of GOME. Next day the orbit is close to SS and crosses the coastal area. On this sunny and cloudfree day at SS both instruments show high values in excellent agreement indicating that tropospheric BrO was still present and was seen this time with GOME as well. On day 950801 the instruments agreed well again on BrO though the orbit went far away over the ice cap. On day 950806 the orbit went over the Davis Street close to Greenland. Larger slant columns agreed within 10-20%. In general the columns seen by the two instruments agreed within error limits except that on occasions when the troposphere contained BrO or the orbit was further away from SS larger deviations might have be occurred. Calculations with GOMETRAN++, a radiative transport program developed at the University of Bremen, show that the differences in SC of GOME and GDOAS for SZA from 86° to 92° are less than 5% for a stratospheric BrO layer. An unintentional validation of BrO in those orbits by groundbased DOAS at Arrival Heights (Kreher et al.,1996) shows excellent agreement. In the beginning of 1996 calibration by the Greenland based instrument were resumed and vortex events above Søndre Strømfjord were studied. The evaluation of the corresponding GOME spectra is underway.

Concluding remarks

The validation of the GOME on-board ESR2, the European Space Agency's new environmental satellite launched in April 1995, has resulted in the first space based observation of the atmospheric BrO. This observation of a key halogen species demonstrates the excellent performance of GOME and provides the opportiunity to derive global maps of BrO. In the future studies of global, seasonal, interannual and longterm variations will be carried out.

Acknowledgements. The support of the groundbased measurements by the Danish Meteorological Institute is highly appreciated. We thank for the financial support of the groundbased measurements by the EU (CT93 0347) and for the support of the evaluation by DARA (50EE9515).

References

Anderson J.G., W.H. Brune, S.A. Lloyd, D.W. Toohey, S. P. Sander, W. L. Starr, M. Loewenstein, and J.R. Podolske, Kinetics of O_3 destruction by ClO and BrO within the Antarctic vortex; an analysis based on ER-2 data, J. Geophys. Res., 94, 11480-11520, 1989

GOME					G-DOAS 67.0° N 50.6° W		
SZA	Time	SC	Lat.	Long.	SZA	Time	SC
[°]	UT	$\frac{10^{14}}{cm^2}$	[°] N	[°] W	[°]	UT	$\frac{10^{14}}{cm^2}$
950728							
89.1	0:35	3.6	65.7	50.8	87.7	0:29	7.6
88.7	0:35	6.5	66.0	51.1	88.0	0:34	7.9
88.4	0:35	4.2	66.3	51.5	88.3	0:38	8.3
88.0	0:35	6.9	66.7	51.9	88.6	0:38	8.2
950729							
88.0	0:04	4.5	66.9	44.2	86.5	0:09	5.8
87.7	0:04	6.2	67.2	44.6	87.0	0:15	5.3
87.4	0:04	6.3	67.5	45.0	87.2	0:19	6.5
87.0	0:04	4.3	67.9	45.4	87.5	0:23	6.1
950730							
90.7	1:12	6.4	64.5	59.0	89.7	0:54	8.6
90.4	1:12	4.1	64.8	59.3	90.1	1:02	9.0
90.0	1:12	3.6	65.2	59.6	90.7	1:12	9.0
89.7	1:12	5.1	65.5	60.0	91.1	1:21	9.9
950731							
89.7	0:41	7.1	65.7	52.3	89.1	0:41	7.2
89.4	0:41	8.1	66.0	52.7	89.4	0:45	7.9
89.0	0:41	5.7	66.4	53.0	89.7	0:50	8.1
950801							
89.4	0:09	5.6	66.3	45.0	87.6	0:14	5.9
89.0	0:09	4.0	66.6	45.3	87.9	0:18	6.3
88.7	0:09	3.4	67.0	45.7	88.2	0:23	5.9
88.4	0:09	6.2	67.3	46.1	88.6	0:28	6.5
950806							
91.8	0:52	7.7	65.2	54.6	90.8	0:44	7.0
91.4	0:52	10.0	65.5	55.0	91.1	0:48	7.0
91.1	0:52	8.0	65.8	55.3	91.8	1:00	7.6
90.8	0:52	8.5	66.2	55.6	92.1	1:06	7.5

Table 1. *Comparison of slant columns of BrO measured by GOME and by groundbased DOAS (GDOAS) in the region of Søndre Strømfjord, SS, Greenland. GOME evaluations were made with sun reference spectra taken at 950725. For GDOAS afternoon spectra of the particular day were used which were normalized to an older reference with known content of BrO absorption. Differential cross section at 355nm was* 6.6×10^{-18} cm^{-2} *for GDOAS (1.1 nm resolution).*

Avallone, L.M., D.W. Toohey, W.H. Brune, R.J. Salawitch A.E. Dessler, and J.G. Anderson, In situ measurements of ClO and ozone: Implications for heterogeneous chemistry and mid-latitude ozone loss, Geophys. Res. Lett., 17, 1795-1798, 1993

Burrows et al., Global ozone monitoring experiment (GOME) measurements of OClO over Antarctica 1995, Proc. of XVIII Quadrennial Ozone Symposium, L'Aquila, Italy, 12-21 September, 1996

Brune W.H., J.G. Anderson, and K.R. Chan, In situ observation of BrO over Antarctica: ER-2 aircraft results from 54°S to 72°S latitude, J. Geophys. Res., 94, 16639-16647, 1989

Carroll, M.A., R.W. Sanders, S. Solomon, and A.L. Schmeltekopf, Visible and near-ultraviolet spectroscopy at McMurdo station, Antarctica. 6. Observations of BrO, J. Geophys. Res., 94, 16633-16638, 1989

Garcia, R.R., and S. Solomon, A new numerical model of the middle atmosphere, 2, Ozone and related species, J. Geophys. Res., 99, 12937-12951, 1994

Jones, R.L., et al., Lagrangian photochemical modeling studies of the 1987 Antarctic spring vortex, 1, Comparison with AAOE observations, J. Geophys. Res., 94, 11529-11558, 1989

Kreher, K., P.V. Johnston, S.W. Wood, G.J. Keys and U. Platt, Ground-based observations of OClO, BrO and NO_2 during 1995 at Arrival Heights (77.8 S) Antarctica, Proc. of XVIII Quadrennial Ozone Symposium, L'Aquila, Italy, 12-21 September, 1996

McElroy, M. B., R. J. Salawitch, S. C. Wofsy and J. A. Logan, Antarctic ozone: Reductions due to synergistic interactions of chlorine and bromine. Nature, 321, 759-762, 1986

Perner D., T. Klüpfel, U. Parchatka, A. Roth, and T. Jörgensen, Groundbased UV-VIS spectroscopy: Diurnal OClO profiles during January 1990 above Søndre Strømfjord, Greenland, Geophys. Res. Lett., 18, 787-790, 1991

Poulet, G.M., M. Pirre, F. Magain, R. Ramaroson, and G.le Bras, Role of the BrO + HO_2 reaction in the stratospheric chemistry of bromine, Geophys. Res. Lett., 23, 2305-2308, 1992

Richter A., M. Eisinger, A. Ladstätter-Weißenmayer, F. Wittrock and J.P. Burrows, Ground based UV/VIS measurements of O_3, NO_2, and BrO over Bremen (53°), Proc. of XVIII Quadrennial Ozone Symposium, L'Aquila, Italy, 12-21 September, 1996

Roth, A., Bodengebundene Fernerkundung von Spurengasen der arktischen Stratosphäre mit der Methode der UV/VIS-Spektroskopie, Dissertation, Gutenberg Universität Mainz, 1992

Solomon, S., R.W. Sanders, and H.L. Miller, Visible and near-ultraviolet spectroscopy at McMurdo Station, Antarctica, 7, OClO diurnal photochemistry and implications for ozone destruction, J. Geophys. Res., 95, 13807-13817, 1990

Toohey, D.W., J.G Anderson, W.H. Brune, and K.R. Chan, In-situ measurements of BrO in the Arctic Stratosphere, Geophys. Res. Lett., 17, 513-516, 1990

Watson, R.T., Chlorine, the chlorine oxides, and other halogen species. CIAP Monogr., No. 1, Publ. DOT-TST-75-51, Dept. of Transportation, Climatic impact assessment program (see Section 5.7.5)

Wofsy, S.C., M.B. McElroy, and Y.L. Yung, The chemistry of atmospheric bromine, Geophys. Res. Lett., 2, 215-218, 1975

World Meteorological Organization (WMO), Global Ozone Research and Monitoring Project, Scientific assessment of ozone depletion: 1994, WMO Rep. No. 37, Geneva 1995

Yung, Y.L., J.P. Pinto, R.T. Watson, and S.P. Sander, Atmospheric bromine and ozone perturbations in the lower stratosphere, J. Atmos. Sci., 37, 339-353, 1980

* present address: DLR-DFD 82234 Weßling, Germany

JOURNAL OF GEOPHYSICAL RESEARCH, VOL. 102, NO. D14, PAGES 16,683–16,695, JULY 27, 1997

GOMETRAN: A radiative transfer model for the satellite project GOME, the plane-parallel version

V. V. Rozanov, D. Diebel,[1] R. J. D. Spurr,[2] and J. P. Burrows
Institut für Umweltphysik, Universität Bremen, Bremen, Germany

Abstract. The Global Ozone Monitoring Experiment (GOME) is a new, nadir-viewing instrument on the European Space Agency satellite ERS 2 which was launched in April 1995. With diode-array detector technology, spectra of the upwelling radiance are measured simultaneously at thousands of wavelengths in the UV, visible, and near-IR regions. Inversion of these measurements by appropriate algorithms allows the retrieval of the distribution of gaseous and particulate constituents, which modulate the radiance by absorption, emission, or scattering processes. Such a retrieval algorithm requires an accurate radiative transfer model to describe the propagation of light through the atmosphere. The model GOMETRAN has been specially designed to fulfill the needs of GOME, but it applies generally to other downward looking space instrumentation in the UV, visible, or near-IR. In this paper the model is described in the plane-parallel version, and the optimization of computational parameters and comparisons with other radiative transfer models is presented.

1. GOME Project

The second European Remote-Sensing (ERS 2) satellite was launched by the European Space Agency (ESA) in April 1995. The scientific payload of ERS 2 is similar to that of ERS 1, which was launched in summer 1992 with a number of instruments designed to measure and assess the state of the Earth's surface. However, to meet the increasingly important requirement to monitor atmospheric composition and processes on a global scale, it was decided to add an atmospheric sensor, GOME (Global Ozone Monitoring Experiment) to the already existing ERS 2 payload. GOME is a small-scale version of the scanning imaging absorption spectrometer for atmospheric chartography (SCIAMACHY), which has been selected for flight on the ESA environmental satellite ENVISAT 1 [*Burrows et al.*, 1988]. GOME was proposed to ESA in answer to a call for atmospheric constituent monitoring instrumentation for ERS 2. Its development represents a collaboration between ESA and the European atmospheric science community [*Burrows et al.*, 1993].

The main objective of GOME is the global assessment of the state of the atmosphere's composition. In recent years it has been recognized that both natural (e.g., volcanic eruptions) and anthropogenic activities (e.g., industrial pollution) may significantly influence the behavior of the atmosphere. The most widely known effects are the Antarctic springtime ozone hole phenomenon, tropospheric pollution in and around industrialised areas, and the potential global climate warming. While ground-based measurements are usually sufficient to monitor well-mixed species with relatively large lifetimes (such as O_2 and CO_2), it is necessary to use satellite instrumentation to obtain a global picture of short-lived constituents (such as O_3 and NO_2), which are characterized by a higher horizontal and vertical variability.

GOME is a nadir-viewing spectrometer which measures solar radiation backscattered from the atmosphere and reflected from the Earth's surface. The ERS 2 satellite follows a Sun-synchronous 100-min polar orbit. The spectrum is measured in four separate bands from 240 to 790 nm at more than 3500 spectral channels, with intervals of 0.11 and 0.2 nm (see Table 1). GOME is building on the experiences with the total ozone mapping system (TOMS) and the solar backscatter ultraviolet (SBUV) instrument on the Nimbus 7 satellite [*Heath et al.*, 1975], which detected the solar backscattered radiation in 4 and 11 channels, respectively, with a width of 1 nm each. Because of the limitation of a small number of channels, all in the ultraviolet wavelength range, TOMS and SBUV constituent retrievals were confined to column amounts and profiles, respectively, of ozone only. Although the primary objective of GOME is, as its name suggests, also the retrieval of ozone amounts, the specific characteristics of the instrument enable information about a number of other atmospheric constituents to be identified in the spectrum. The gases that are potential candidates for a retrieval include O_3, O_2, O_4, the nitrogen compounds NO, NO_2, and NO_3, the halogen species OClO, ClO,

[1]Now at European Organisation for the Exploitation of Meteorological Satellites (EUMETSAT), Darmstadt, Germany.

[2]Now at Deutsche Forschungsanstalt für Luft- und Raumfahrt (DLR), Weßling, Germany.

Paper number 96JD01535.
0148-0227/97/96JD-01535$09.00

Table 1. GOME Instrument

Characteristic	Value
Wavelength coverage	240 to 790 nm in four bands 1, 240-316 nm; 2, 311-405 nm; 3, 405-611 nm; 4, 595-793 nm;
Spectral intervals	0.11 nm (bands 1 and 2), 0.20 nm (bands 3 and 4)
Spectral resolution	0.22 nm (bands 1 and 2), 0.31 nm (bands 3 and 4)
Instantaneous field of view	0.143° across track, 2.860° along track
Flight altitude	780 km
Ground speed	7 km/s
Scan angle	variable, with a maximum of ±31°
Scanning period	4.5 s (forward scan), 1.5 s (fly back scan)
Readout time	12 s below 312 nm, 1.5 s above 312 nm (default values)
Spatial resolution on ground	320 x 40 km^2 (at 1.5 s readout and ±31° swath)
	960 x 80 km^2 (at 30 s readout and ±31° swath)

and BrO, plus HCHO, SO_2, and H_2O, some of which might be detectable only under perturbed atmospheric conditions as, for example, ozone hole formation, pollution episodes, etc. In addition, the distribution of particulate substances (aerosols, tropospheric clouds, polar stratospheric clouds) and Earth surface reflectance properties will be investigated. While it will be possible to retrieve vertical profiles of O_3 and possibly of NO_2 and aerosols, the retrieval of other gaseous constituents will most likely be limited to column amounts, i.e., concentrations integrated vertically over the atmosphere.

The simultaneous retrieval of a multitude of parameters, which may be partially cross-correlated with each other, is a challenging task and requires a sophisticated retrieval algorithm. The retrieval method applicable to this task and chosen for GOME is based on "optimal estimation," in which the measurements are supplemented by a priori information about the parameters to be retrieved, in order to achieve a stable and unique inverse solution [*Rodgers*, 1976]. (It should be mentioned here that the first operational GOME retrieval algorithm is based on a different method and will be restricted to the retrieval of total column amounts of O_3 only. At present, the application of the optimal estimation technique for GOME is at a scientific level but will be considered for the second generation of the operational data analysis.) Optimal estimation is an iterative process in which the atmospheric retrieval parameters are adjusted to obtain the best fit between a simulated radiance spectrum and the measured spectrum of the radiance. The calculation of simulated radiances requires a radiative transfer model which describes the propagation of solar radiation through the atmosphere by taking into account scattering, absorption, and emission processes in the atmosphere, and the reflection of the Earth's surface.

The development of a GOME-specific radiative transfer model, GOMETRAN, is the subject of this paper. The requirements for such a model will be discussed in section 2, which is followed by a description of the general concept of GOMETRAN in section 3, and an exposition of the mathematical principles in section 4. The optimization of computational parameters which determine accuracy and speed is described in section 5 for the plane-parallel version of GOMETRAN. Section 6 presents comparisons with other plane-parallel radiative transfer models. Section 7 concludes with a summary.

2. Requirements for a GOME-Specific Radiative Transfer Model

Any radiative transfer model in an "optimal estimation" retrieval algorithm must calculate two kinds of output: first a simulated spectrum of the radiance as received at the satellite, and secondly the so-called "weighting functions." The latter are the derivatives of the radiance with respect to the parameters to be retrieved (e.g., concentrations of O_3 at various atmospheric levels, column amounts of gases, etc.). Existing radiative transfer models are not set up for the convenient calculation of weighting functions (this is because of the inherent mathematical structure). With these models the only way to derive weighting functions is to perturb the retrieval parameters singly and calculate the resulting radiance; the difference to the radiance simulated without perturbation yields the desired weighting function. Depending on the number of parameters to be retrieved, the radiative transfer model has to be executed many times for each iteration step of the retrieval.

The efficient calculation of weighting functions is one of the most important (but not the only) criterion for the selection of a model applicable to GOME. The ultimate version of such a model must contain the following features: (1) spectral coverage of the full GOME range between 240 and 790 nm at intervals corresponding to the instrument detector pixels, namely 0.11 nm in the ultraviolet and 0.20 nm in the visible; (2) inclusion of all relevant atmospheric gases with absorption structures in the GOME spectral range, i.e., O_3, NO_2, NO_3, ClO, OClO, BrO, H_2O, O_2, O_4, HCHO, and SO_2; (3) inclusion of all relevant emissions features, e.g., NO γ bands; (4) inclusion of all atmospheric constituents with scattering properties in the GOME spectral range, i.e., of molecular (Rayleigh) scatterers and particulate scatter-

ers (aerosols and clouds); (5) an exact treatment of multiple scattering in the mathematical solution of the basic radiative transfer equation (RTE) in order to achieve accurate simulations of radiance and weighting functions; (6) an adequate description of the land surface spectral reflectance and of the bidirectional reflectance over the oceans; (7) spherical and refractive geometry to ensure global applicability of the model; and (8) high computational speed for the calculation of radiance and especially weighting functions; this is a requirement for future real-time data processing algorithms. A review of the literature showed that none of the existing and publicly available models could fulfill these requirements. The models LOWTRAN and MODTRAN both involve a simplified approach to describe multiple scattering and are therefore not accurate enough [*Isaacs et al.*, 1989, 1987; *Kneizys et al.*, 1986; *Berk et al.*, 1989]. FASCODE is a high-resolution model designed to take into account the line character of gas absorption above 560 nm [*Ridgway et al.*, 1982; *Isaacs et al.*, 1989, 1987; *Clough et al.*, 1986, 1989]. The calculation of radiative transfer by a line-by-line approach is too time consuming for GOME. The model DISORT has acceptable accuracy and speed provided that only the calculation of the spectral radiance is considered [*Stamnes and Swanson*, 1981; *Stamnes and Dale*, 1982; *Stamnes and Conklin*, 1984; *Stamnes et al.*, 1988].

3. General Concept of GOMETRAN

The decision to develop a GOME-specific model, GOMETRAN, was driven by the necessity to calculate efficiently the weighting functions in addition to the radiance spectrum. This requirement resulted in the selection of the finite difference method as most suitable for this purpose [*Barkstrom*, 1976; *Lenoble*, 1985]. This method is amenable to a linearized description of the change in radiance caused by variations in any of the atmospheric parameters in the radiative transfer equation , i.e., the weighting functions. This provides an efficient way to perform sensitivity studies or to use the model in any retrieval algorithm which requires weighting functions for the fitting process (least squares, optimal estimation, etc.).

GOMETRAN is available both in a plane-parallel and in a spherical version, the latter including refraction. The plane-parallel model is applicable to solar zenith angles below 75° and hence must exclude polar regions from its geographical coverage. This model has been optimized and validated and is presented in this paper. The spherical version is still undergoing a thorough investigation; it is actually a quasi-spherical solution, whereby only the solar flux entering the RTE is calculated in a spherical geometry, while expressions for single and multiple scattering correspond to those in the plane-parallel RTE (see section 4). It is anticipated that this approach is suitable for solar zenith angles below 93° (which is the largest possible angle occurring during a GOME polar orbit).

With regard to the wavelength coverage and spectral resolution, GOMETRAN is a generic model and can therefore be matched to the design of the GOME instrument. The model can be operated either in a monochromatic mode, where at each wavelength a time-consuming solution of a system of equations has to be performed, or in a polychromatic mode, where radiance calculations for a larger number of wavelengths are based on a single evaluation of this solution. This second mode of operation is less accurate but computationally efficient (see section 5.5).

With respect to the mathematical implementation of absorption and emission features, GOMETRAN has been set up as a band model. This implies that line absorption spectra for gases such as O_2 and H_2O need to be preprocessed to a form suitable as input for GOMETRAN. Absorption spectra for other GOME-relevant gases can be taken directly from laboratory-measured cross sections. This refers to O_3, O_4, NO_2, NO_3, ClO, OClO, BrO, HCHO, and SO_2.

Multiple scattering by molecular and particulate substances can, in principle, be treated accurately by the finite difference method. There are, however, two features in the current version of GOMETRAN that are worth mentioning. The first is the description of the aerosol scattering phase functions by the Henyey-Greenstein formula [*Lenoble*, 1985]. The Henyey-Greenstein factor in this formula determines, in conjunction with the scattering angle, unambiguously the value of the phase function. Highly anisotropic phase functions cannot be characterized accurately with this approximation. The option to read phase functions from user-provided databases will be included shortly. The second note refers to clouds in GOMETRAN. At present, clouds have to be treated as particle layers of high optical thickness. Inside the cloud the radiance I changes rapidly with penetration depth z, with correspondingly high values for the gradient dI/dz. In the finite difference method this gradient is approximated by a finite difference $\Delta I/\Delta z$ between two discrete atmospheric levels used in the model (see also section 4). To follow radiative transport through the cloud accurately, a very large number of atmospheric levels is required and this makes the model too slow for any real-time data processing. An alternative approach is currently under investigation for optically thick water droplet clouds, whereby the cloud top is treated as a bidirectional reflecting surface (*T. Kurosu*, private communication, 1994). The Earth's surface can be selected to be either a Lambertian, wavelength-independent reflector or to be described by a bidirectional surface reflectance.

4. Mathematical Principles of GOMETRAN

4.1. Calculation of Radiance

The basis for any radiative transfer model is the integro-differential radiative transfer equation for the radiation field I. The parameters that are needed to describe the RTE are (1) the atmospheric composition, given by vertical concentration profiles of the gaseous and particulate constituents; (2) the Earth's surface spectral reflectance; (3) the viewing geometry, defined by the solar zenith angle, the line-of-sight angle (which is closely related to the intrument scan angle), and the relative azimuth angle between the Sun and the line-

of-sight direction at top of atmosphere; and (4) a database of spectral parameters, including the absorption, emission, and scattering properties of gases and particulates. In a plane-parallel atmosphere the radiation I depends only on three spatial coordinates: the altitude z in the atmosphere (an alternative is the optical depth), the zenith angle θ, and the azimuthal angle φ. The solar zenith angle θ_0 is a parameter in this case. The RTE can now be expressed in the following form, where μ is the cosine of the zenith angle θ and where the dependence on the wavelength λ is omitted. For simplicity a Lambertian surface albedo is assumed

$$\mu\frac{dI(z,\mu,\varphi)}{dz} = -c(z)I(z,\mu,\varphi) + \frac{b(z)}{4\pi}\int_0^{2\pi}\int_{-1}^{1} p(z,\mu,\mu',\varphi,\varphi')I(z,\mu',\varphi')d\mu'd\varphi' \quad (1)$$

where

$$\begin{aligned} c(z) &= a(z) + b(z) \\ a(z) &= a_M(z) + \sum_{i=1}^{k}\alpha_i n_i(z) \\ b(z) &= b_M(z) + b_R(z) \end{aligned} \quad (2)$$

and the boundary conditions at the top and the bottom of the atmosphere lead to

$$\begin{aligned} I^-(z_0,\mu,\varphi) &= \delta(\mu-\mu_0,\varphi-\varphi_o)\pi F \\ I^+(0,\mu,\varphi) &= \frac{A}{\pi}\int_0^{2\pi}\int_0^{1} I^-(0,\mu',\varphi')\mu'd\mu'd\varphi' \end{aligned} \quad (3)$$

where $I^-(z_0,\mu,\varphi)$ is the downwelling radiance at z_0 and $I^+(0,\mu,\varphi)$ is the upwelling radiance at the ground. The other symbols used in the equations have the following meaning:

I	total radiance (i.e., radiation field);
z	altitude;
z_0	altitude at top of atmosphere;
μ,μ'	cosines of zenith angles θ,θ';
μ_0	cosine of the solar zenith angle θ_0;
φ,φ'	azimuthal angles in relation to the line-of-sight projection on the Earth's surface;
φ_0	azimuthal angle of the Sun in relation to the line-of-sight projection on the Earth's surface;
k	number of trace gases;
c	total extinction coefficient;
a	total absorption coefficient (sum of trace gas and particle absorption coefficients);
b_R	Rayleigh-scattering coefficient;
b_M	particle-scattering coefficient;
b	total scattering coefficient (sum of Rayleigh- and particle-scattering coefficients);
p_R	Rayleigh-scattering phase function;
p_M	particle-scattering phase function;
p	total scattering phase function (weighted sum of Rayleigh- and particle-scattering phase functions, i.e. $(b_R p_R + b_M p_M)/(b_R + b_M)$);
α_i	trace gas absorption cross sections for all relevant gases;
n_i	concentrations of trace gases;
a_M	particle absorption coefficient;
$\pi F\mu_0$	solar flux at the top of the atmosphere;
A	spectral reflectance (Lambertian) of the Earth's surface.

Various mathematical techniques have been developed to obtain a numerical solution for the radiance I from the RTE. Each method involves approximations which determine the accuracy and speed of the numerical algorithm. The "finite difference method" chosen for GOMETRAN combines high accuracy with reasonable computational speed [*Lenoble*, 1985].

This method is based on an expansion of the scattering phase function $p(\gamma)$ in terms of Legendre polynomials, where γ is the scattering angle between the directions of incident and scattered radiance. (It should be noted here that the expansion with Legendre polynomials is not specific to the finite difference method but may be used in association with a number of methods to solve the RTE.) Using the geometrical relation between cosine γ and the cosines of the zenith angles μ and μ' and the azimuth angles φ and φ' for the directions of incidence and scattering, the phase function can be expanded as a Fourier series of the cosine of the azimuthal angle

$$p(z,\mu,\mu',\varphi,\varphi') = p^0(z,\mu,\mu') + 2\sum_{m=1}^{M} p^m(z,\mu,\mu')\cos(m(\varphi-\varphi')) \quad (4)$$

where the harmonic moments $p^m(z,\mu,\mu')$ can be described in terms of associated Legendre polynomials. The radiance I can be expanded correspondingly into a Fourier series of the cosine of $(\varphi-\varphi_0)$.

The combination of the two Fourier series for the phase function and the radiance in conjunction with the application of the orthogonality property of the integrals over the azimuthal angle φ in the RTE results in an elimination of the dependence on φ. The RTE reduces to a set of equations containing the Fourier components of the diffuse upwelling and downwelling radiances I^{+m}_{diff} and I^{-m}_{diff} the subscripts m and diff are omitted for all the following equations for reasons of simplicity:

$$\mu\frac{dI^+(z,\mu)}{dz} = -c(z)I^+(z,\mu) + \frac{b(z)}{2}\int_0^1 p(z,\mu,\mu')I^+(z,\mu')d\mu' + \frac{b(z)}{2}\int_0^1 p(z,\mu,-\mu')I^-(z,\mu')d\mu'$$

$$+\frac{b(z)}{4}p(z,\mu,-\mu_0)Fe^{-\frac{\tau(z)}{\mu_0}}$$
$$+\frac{b(z)}{2}AF\mu_0 e^{-\frac{\tau_0}{\mu_0}}\int_0^1 p(z,\mu,\mu')e^{-\frac{\tau_0-\tau(z)}{\mu'}}d\mu'$$

$$\mu\frac{dI^-(z,\mu)}{dz} = -c(z)I^-(z,\mu) + \frac{b(z)}{2}\int_0^1 p(z,-\mu,\mu')I^+(z,\mu')d\mu' + \frac{b(z)}{2}\int_0^1 p(z,-\mu,-\mu')I^-(z,\mu')d\mu' + \frac{b(z)}{4}p(z,-\mu,-\mu_0)Fe^{-\frac{\tau(z)}{\mu_0}} + \frac{b(z)}{2}AF\mu_0 e^{-\frac{\tau_0}{\mu_0}}\int_0^1 p(z,-\mu,\mu')e^{-\frac{\tau_0-\tau(z)}{\mu'}}d\mu' \quad (5)$$

where τ is the vertical optical depth and τ_0 is the optical depth of the entire atmosphere. For higher-order Fourier components ($m>0$) the surface reflection term in this equation is zero. The boundary conditions at the top and at the bottom of the atmosphere yield

$$\begin{aligned} I^-(z_0,\mu) &= 0 && \text{for } m\geq 0\\ I^+(0,\mu) &= 2A\int_0^1 I^-(0,\mu')\mu'd\mu' && \text{for } m=0\\ I^+(0,\mu) &= 0 && \text{for } m\geq 1 \end{aligned} \quad (6)$$

The next step of the finite difference method is to introduce two new variables, J and H :

$$\begin{aligned} J(z,\mu) &= \frac{1}{2}(I^+(z,\mu)+I^-(z,\mu))\\ H(z,\mu) &= \frac{1}{2}(I^+(z,\mu)-I^-(z,\mu)) \end{aligned} \quad (7)$$

and equation (5) now reduces to

$$\mu\frac{dH(z,\mu)}{dz}+c(z)J(z,\mu) - \frac{b(z)}{2}\int_0^1 p^+(z,\mu,\mu')J(z,\mu')d\mu' = \frac{b(z)}{4}Fe^{-\frac{\tau(z)}{\mu_0}}\frac{1}{2}p^+(z,\mu,\mu_0) + \frac{b(z)}{2}AF\mu_0 e^{-\frac{\tau_0}{\mu_0}}\frac{1}{2}\int_0^1 p^+(z,\mu,\mu')e^{-\frac{\tau_0-\tau(z)}{\mu'}}d\mu' \equiv Q^+(z,\mu) \quad (8)$$

$$\mu\frac{dJ(z,\mu)}{dz}+c(z)H(z,\mu) - \frac{b(z)}{2}\int_0^1 p^-(z,\mu,\mu')H(z,\mu')d\mu' = \frac{b(z)}{4}Fe^{-\frac{\tau(z)}{\mu_0}}\frac{1}{2}p^-(z,\mu,\mu_0) + \frac{b(z)}{2}AF\mu_0 e^{-\frac{\tau_0}{\mu_0}}\frac{1}{2}\int_0^1 p^-(z,\mu,\mu')e^{-\frac{\tau_0-\tau(z)}{\mu'}}d\mu' \equiv Q^-(z,\mu)$$

with the abbreviations

$$\begin{aligned} p^+(z,\mu,\mu') &= p(z,\mu,\mu')+p(z,\mu,-\mu')\\ p^-(z,\mu,\mu') &= p(z,\mu,\mu')-p(z,\mu,-\mu') \end{aligned} \quad (9)$$

The boundary conditions now correspond to

$$\begin{aligned} J(z_0,\mu)-H(z_0,\mu) &= 0 && \text{for } m\geq 0\\ J(0,\mu)-2A\int_0^1 J(0,\mu')\mu'd\mu'+H(0,\mu) &= 0 && \text{for } m=0\\ -2A\int_0^1 H(0,\mu')\mu'd\mu' &= 0 && \\ J(0,\mu)+H(0,\mu) &= 0 && \text{for } m\geq 1 \end{aligned} \quad (10)$$

In the next steps discrete coordinates for the altitude z and the cosine of the zenith angle μ are selected and the integrals over the zenith angle μ in the RTE are replaced by Gaussian quadrature summation over the "discrete" streams. (In conjunction with the expansion of the phase function into a series of Legendre polynomials, the Gaussian integration method minimizes the residual error.) As a result, the gradients dH/dz and dJ/dz are replaced by finite differences between two discrete altitude levels, $\Delta H/\Delta z$ and $\Delta J/\Delta z$. These procedures are described in detail by [*Lenoble*, 1985]. Thus the RTE is obtained in a matrix form:

$$C\vec{L} = \vec{R} \quad (11)$$

All elements of the matrix C and of the vector $\vec{R}$ are known functions of the atmospheric, surface, viewing, and spectroscopic parameters, while the vector $\vec{L}$ on the left side contains the unknown quantities H and J for each altitude level and zenith angle direction. The solution can be obtained by decomposition of the matrix C into lower and upper triangular matrices. This so called LU decomposition is required for each of the Fourier components. To obtain the radiance received at the satellite, all Fourier components have to be added up. The RTE considers only the "diffuse" part of the radiation, which has been scattered at least once. The direct contribution by the solar flux being reflected at the Earth's surface into the direction of the satellite is added separately.

The matrix C dimensions are of the order of $N \times N$, where N is the product of the number of discrete atmospheric levels plus 2 with the number of discrete zenith angles (i.e., streams). Typical values of matrix dimension is of about 400 x 400. To save computational time, a procedure is adopted to avoid matrix LU decomposition at every single wavelength. The need for a new decomposition when stepping through the wavelength range is judged by the change in matrix norms between the previous and the new wavelength. If the change is below a certain limit, the previously decomposed matrix is used in conjunction with an appropriate correction procedure, which is based on first-order perturbation theory.

4.2. Calculation of Weighting Functions

For the derivation of weighting functions it is necessary to express the relation between changes of the atmospheric and surface parameters τ, b, c and A on the one hand and the radiances H and J on the other hand. For this purpose, new perturbed atmospheric and surface parameters are defined as $p' = p + \delta p$, where p represents τ, b, c, or A. The correspondingly perturbed J and H function can be written as

$$\begin{aligned} H'(z,\mu,\lambda) &= H(z,\mu,\lambda) + \delta H(z,\mu,\lambda) \\ J'(z,\mu,\lambda) &= J(z,\mu,\lambda) + \delta J(z,\mu,\lambda) \end{aligned} \tag{12}$$

Using the perturbed values H', J', c', b', τ', and A' in equation (8) and in boundary condition (10) instead of H, J, c, b, τ, and A and ignoring second-order terms, the first part of equation (8) can be written as

$$\begin{aligned} &\mu \frac{d\delta H(z,\mu)}{dz} + c(z)\delta J(z,\mu) - \\ &\frac{b(z)}{2}\int_0^1 p^+(z,\mu,\mu')\delta J(z,\mu')d\mu' = \\ &-\delta c(z) J(z,\mu) + \frac{\delta b(z)}{2} \\ &\int_0^1 p^+(z,\mu,\mu') J(z,\mu')d\mu' + \delta Q^+(z,\mu) \end{aligned} \tag{13}$$

the variation of the source term Q^+ can be expressed in the following way:

$$\begin{aligned} \delta Q^+(z,\mu) &= \frac{\delta b(z)}{4} F e^{-\frac{\tau(z)}{\mu_1}} \frac{1}{2} p^+(z,\mu,\mu_0) \\ &- \frac{b(z)}{4} F e^{-\frac{\tau(z)}{\mu_1}} \frac{1}{2\mu_0} p^+(z,\mu,\mu_0)\delta\tau \\ &+ \frac{\delta b(z)}{4} A F \mu_0 e^{-\frac{\tau_0}{\mu_1}} \int_0^1 p^+(z,\mu,\mu') e^{-\frac{\tau_0 - \tau(z)}{\mu'}} d\mu' \\ &- \frac{b(z)}{4} A F e^{-\frac{\tau_0}{\mu_1}} \delta\tau_0 \int_0^1 p^+(z,\mu,\mu') e^{-\frac{\tau_0 - \tau(z)}{\mu'}} d\mu' \end{aligned} \tag{14}$$

$$\begin{aligned} &+ \frac{b(z)}{4} A F \mu_0 e^{-\frac{\tau_0}{\mu_1}} (\delta\tau - \delta\tau_0) \int_0^1 p^+(z,\mu,\mu') e^{-\frac{\tau_0 - \tau(z)}{\mu'}} \frac{d\mu'}{\mu'} \\ &+ \frac{b(z)}{4} A F \mu_0 e^{-\frac{\tau_0}{\mu_1}} \delta A \int_0^1 p^+(z,\mu,\mu') e^{-\frac{\tau_0 - \tau(z)}{\mu'}} d\mu' \end{aligned}$$

where the following expansion has been used:

$$e^{-\frac{(\tau_0 + \delta\tau_0)}{\mu_1}} \approx e^{-\frac{\tau_0}{\mu_1}} - \frac{1}{\mu_0} e^{-\frac{\tau_0}{\mu_1}} \delta\tau_0 \tag{15}$$

Exchanging J and H and replacing p^+ by p^- and Q^+ by Q^-, a similar equation results for the differential $d\delta J/dz$. The boundary conditions are now given by

$$\begin{aligned} &\delta J(z_0,\mu) - \delta H(z_0,\mu) = 0 && \text{for } m \geq 0 \\ &\delta J(0,\mu) - 2A \int_0^1 \delta J(0,\mu')\mu' d\mu' \\ &\quad + \delta H(0,\mu) + 2A \int_0^1 \delta H(0,\mu')\mu' d\mu' = && (16) \\ &2\delta A \int_0^1 (J(0,\mu') - H(0,\mu'))\mu' d\mu' && \text{for } m = 0 \\ &\delta J(z_0,\mu) + \delta H(z_0,\mu) = 0 && \text{for } m \geq 1 \end{aligned}$$

The variation of $\delta\tau$, δb, and δc arises from changes in aerosol scattering and absorption coefficient, Rayleigh-scattering coefficient, and trace gas absorption coefficients. These parameters are dependent on wavelength and are not suitable as parameters for weighting function calculation. New parameters, which are independent of wavelength, are required: (1) for trace gases instead of absorption coefficients the vertical profiles of the trace gas concentration $n_i(z)$ have been chosen; (2) for aerosol the vertical profile of absorption and scattering coefficients at three specified reference wavelengths have been selected and linear interpolation has been used for the other wavelengths:

$$\begin{aligned} &\text{for } \lambda_1 \leq \lambda \leq \lambda_2: \\ &\quad b_M(z,\lambda) = (1-\gamma_1) b_M(z,\lambda_1) + \gamma_1 b_M(z,\lambda_2) \\ &\text{for } \lambda_2 < \lambda \leq \lambda_3: \\ &\quad b_M(z,\lambda) = (1-\gamma_2) b_M(z,\lambda_2) + \gamma_2 b_M(z,\lambda_3) \end{aligned} \tag{17}$$

with $\gamma_1 = (\lambda - \lambda_1)/(\lambda_2 - \lambda_1), \gamma_2 = (\lambda - \lambda_2)/(\lambda_3 - \lambda_2)$ and the same equation for $a_M(z,\lambda)$; (3) for Rayleigh scattering the wavelength-independent part of the scattering coefficient is selected:

$$b_R(z,\lambda) = \beta_R(\lambda) r(z) \tag{18}$$

where $r(z)$ is a function of temperature and pressure.

Thus all atmospheric parameters are now described by $n_i(z)$ $(i = 1, \ldots, k)$, $b_M(z,\lambda_1)$, $b_M(z,\lambda_2)$, $b_M(z,\lambda_3)$, $a_M(z,\lambda_1)$,

$a_M(z,\lambda_2)$, $a_M(z,\lambda_3)$, $r(z)$, and A. It should be noted that the number of reference wavelengths λ_i and, correspondingly, the number of aerosol parameters can be readily extended if considered necessary.

As different atmospheric parameters have different orders of magnitude, a normalization is used which is given here for the example of trace gas concentrations:

$$\delta\xi_i(z) = \frac{\delta n_i(z)}{n_i(z)}, \quad i = 1, \ldots, k \tag{19}$$

Using the normalized parameters, equation (13) takes the form

$$\mu\frac{d\delta H(z,\mu)}{dz} + c(z)\delta J(z,\mu) - \frac{b(z)}{2}\int_0^1 p^+(z,\mu,\mu')\delta J(z,\mu')d\mu' = \sum_{j=1}^{P}\int_0^{z_0} v_j^+(z',z,\mu)\delta\xi_j(z')dz' \tag{20}$$

as an example the functions $v_j^+(z',z,\mu)$ for dimensionless variation of the vertical profile of the trace gas concentration is as follows:

$$\begin{aligned} v_j^+(z',z,\mu) = -\alpha_j(z',\lambda)n_j(z')\Big\{ & J(z',\mu)\delta(z-z') \\ & -\frac{b(z)}{4}Fe^{-\frac{\tau_0}{\mu_0}}\frac{1}{2\mu_0}p^+(z,\mu,\mu_0)d(z,z') \\ & -\frac{b(z)}{4}AFe^{-\frac{\tau_0}{\mu_0}}\Big[\int_0^1 p^+(z,\mu,\mu')e^{-\frac{\tau_0-\tau(z)}{\mu'}}d\mu' \\ & -\mu_0\int_0^1 p^+(z,\mu,\mu')e^{-\frac{\tau_0-\tau(z)}{\mu'}}\frac{d\mu'}{\mu'}(1-d(z,z'))\Big]\Big\} \end{aligned} \tag{21}$$

where P is the number of parameters; $\delta(z-z')$ is the Dirac delta function, and $d(z,z')$ is the Heaviside function:

$$\begin{aligned} d(z,z') &= 0 \quad 0 \le z' < z \\ d(z,z') &= 1 \quad z \le z' \le z_0 \end{aligned} \tag{22}$$

In the following steps the integrals in the above equation are replaced by sums with suitable Gaussian weights, and the differentials $d\delta H/dz$ and $d\delta J/dz$ are replaced by the differences $\Delta\delta H/\Delta z$ and $\Delta\delta J/\Delta z$. This is analogous to the treatment of the basic radiative transfer equation in section 4. The previous equation can be expressed now in matrix form:

$$C\delta\vec{L} = B\delta\vec{\xi} \tag{23}$$

where vector $\delta\vec{\xi}$ consists of all vectors $\delta\vec{\xi}_j$ which are represented the functions $\delta\xi_i(z)$ in equation (20) for the finite altitude grid, the vector $\delta\vec{L}$ contains in an alternating way elements of δH and δJ, and the matrix C is identical to the one in equation (11).

Equation (23) describes the linear relationship between variation of radiance and the variation of selected atmospheric parameters. This equation is, therefore, the linear finite difference radiative transfer equation. The solution of equation (23) is

$$\delta\vec{L} = C^{-1}B\delta\vec{\xi} \tag{24}$$

As is evident from equation (24) and the above definition of the weighting functions as the derivatives of the radiance with respect to the atmospheric parameters, the matrix product $C^{-1}B$ is the finite difference approximation of these derivatives. It should be noted that it is not necessary to perform a new decomposition of matrix C to obtain the weighting functions but only to calculate the matrix B. A detailed discussion of the weighting functions generated by GOMETRAN is given elsewhere (*V.V. Rozanov*, A linear radiative transfer model for the interpretation of measurements of scattered and reflected solar radiation of the Earth's atmosphere, submitted to Journal of Quantitative Spectroscopy and Radiative Transfer, 1996).

5. Optimization of Computational Parameters

The "finite difference method" chosen for GOMETRAN represents a numerical solution of the radiative transfer equation (RTE). The accuracy of the solution is limited by the need to adopt discrete values for the height and angular coordinates and the expansion of variables in series of finite length. The values assigned to the related computational parameters determine the accuracy. For GOMETRAN the objective is an accuracy of 1% for the simulated radiance. The ensuing requirements on the computational parameters have been investigated for the plane-parallel version of GOMETRAN and are discussed in the following.

5.1. Number of Fourier Terms

In GOMETRAN the radiance is expanded as a Fourier series in the azimuthal coordinate. The terms in this series are calculated consecutively, so that an automatic convergence criterion can be applied; this criterion determines the number of Fourier terms required to achieve a given accuracy. An example for the convergence of radiance at five different wavelengths in the GOME spectral range is shown in Figure 1. Four Fourier terms are sufficient to achieve an accuracy of better than 1% in the visible wavelength range. An even lower number of Fourier terms is required in the ultraviolet. The reason for this is that the backscattered radiance in the ultraviolet originates from the upper parts of the atmosphere where molecular scattering, which has a comparably low degree of anisotropy, is dominant. This results in a low angular dependency in the radiance. In visible wavelength regions, where aerosols contribute more strongly to the radiance, the more anisotropic aerosol scattering phase function leads to higher anisotropy in the radiance and hence a larger number of Fourier terms is required.

5.2. Number of Legendre Polynomials

A second important computational parameter related to the azimuthal coordinate in the RTE is the number of Leg-

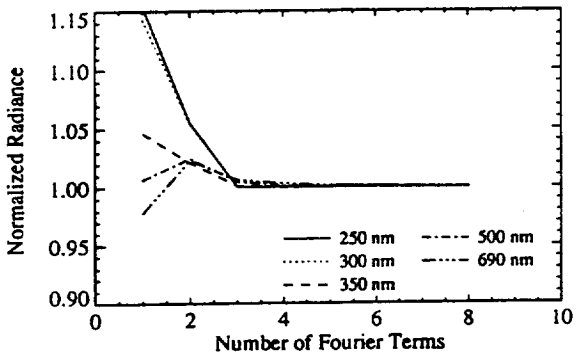

Figure 1. Dependence of the radiance on the number of Fourier terms. The simulated radiance is displayed at five wavelengths as a function of the number of Fourier terms used in the simulation; the radiance is normalized to that obtained using eight Fourier terms to illustrate the degree of convergence with respect to this "quasi-infinite" value. Atmospheric conditions: latitude 45°N, time of year July, with O_3, NO_2, temperature, and pressure calculated from the MPI two-dimensional atmospheric model [B92]; four different aerosol types: maritime between 0 and 2 km, tropospheric between 2 and 10 km, background stratospheric between 10 and 30 km, and mesospheric between 30 and 60 km; surface albedo 0.3. Conditions for the viewing geometry: solar zenith angle 75°; relative azimuth angle between the Sun and the satellite 60° (as defined by the line of sight); line-of-sight zenith angle 30°. Conditions for the computation: 49 atmospheric layers, 7 stream zenith angles, 20 Legendre polynomials.

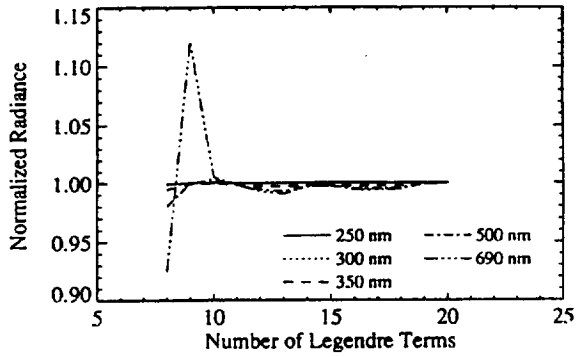

Figure 2. Dependence of the radiance on the number of Legendre terms. The simulated radiance is displayed at five wavelengths as a function of the number of Legendre terms used in the simulation; the radiance is normalized to that obtained using 20 Legendre terms to illustrate the degree of convergence with respect to this "quasi-infinite" value. Conditions for the atmosphere, the viewing geometry, and the computation are as in Figure 1 but with four Fourier terms and the number of Legendre terms being varied.

endre polynomials. This number determines the accuracy of the description of the scattering phase function as series in Legendre polynomials. As with the number of the Fourier terms, there are significant differences between the behavior in the ultraviolet and in the visible (for an example, see Figure 2). The molecular (Rayleigh) scattering phase function is fully described by the sum of a zeroth-and second-order Legendre polynomial. Thus the ultraviolet radiance, which is dominated by molecular scattering, remains almost unchanged for scattering expansions with three or more Legendre polynomials. In the visible the anisotropy of the aerosol phase function requires a higher number of Legendre expansion terms. For the aerosol types studied so far (maritime, tropospheric background, and stratospheric background) an expansion with 15 to 20 terms is sufficient for the 1% accuracy objective.

However, these results for aerosols were obtained using the relatively smooth Henyey-Greenstein phase functions, and more realistic particulate phase functions (especially those for water or ice particulates) would require many more terms in the Legendre expansion. Sharp forward peaks in the phase functions can be treated separately after an approximation by a delta function, and this helps to lower the Legendre number.

5.3. Number of Zenith Stream Angles

The numerical solution of the RTE in GOMETRAN requires a discretization of the coordinate of the zenith angle. The "streams" of radiation propagating through the atmosphere are calculated in these discrete directions. The directions are then the abscissae used in the Gaussian quadrature of the zenith angle integrals in the RTE, which are replaced by summations. The number of streams should be at least half the number of Legendre polynomials to minimize the error caused by the Gaussian quadrature, which replaces the integral over the zenith angle in the RTE by a summation over discrete streams. The number of streams has a significant effect on the computational time because the dimensions of the matrix, which has to undergo the LU decomposition, are proportional to the number of stream angles.

Five different wavelengths were selected to study the number of streams required to achieve a 1% convergence. Fig-

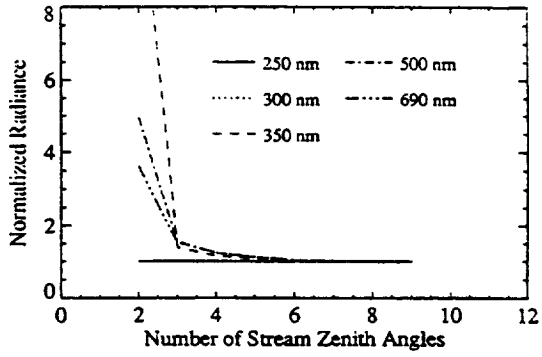

Figure 3. Dependence of the radiance on the number of zenith stream angles. The simulated radiance is displayed at five wavelengths as a function of the number of stream zenith angles terms used in the simulation; the radiance is normalized to that obtained using nine stream angles to illustrate the degree of convergence with respect to this "quasi-infinite" value. Conditions for the atmosphere, the viewing geometry, and the computation are as in Figure 1 but with four Fourier terms and the number of stream angles being varied.

ure 3 shows that seven streams (for the half space) are sufficient in the visible range, whereas in the ultraviolet the number of streams is not critical due to the dominance of single scattering in this spectral range. Therefore in the ultraviolet the multiple-scattering and the surface reflection terms in the RTE can be neglected, thus making the Gaussian quadrature of the integrals redundant. The remaining single-scattering part of the RTE can be solved directly for a stream into the line-of-sight direction and is hence not dependent on the zenith stream angles.

5.4. Selection of Altitude Levels

The selection of altitude levels in GOMETRAN is more difficult than the selection of the other computational parameters. The reason for this is that there are effectively two degrees of freedom: the number of levels and the choice of the altitudes of the levels. In the ultraviolet the selection of levels depends on the wavelength, because of rapid changes of the optical depth and hence the penetration depth in this range. GOMETRAN uses four different altitude grids: three in the ultraviolet up to 315 nm, with a shift of levels from the upper to the lower atmosphere toward the longer wavelength end; and the fourth grid for the rest of the GOME range with a concentration of levels in the lower 35 km of the atmosphere. In the UV the transitions between different altitude grids are at 275 nm, 300 nm, and 315 nm.

The consequence of a poor selection of the number and positions of levels can result in sudden changes in the calculated radiance, which occur at wavelengths corresponding to transitions between the grids, which is demonstrated in Figure 4 for the transition occurring at 300 nm. There are two different approaches to the determination of the number and suitable positions of the atmospheric levels required to calculate the radiance accurately. The first is to adopt an altitude grid covering the relevant part of the atmosphere (up to about 60 km) with more or less equally spaced levels with high vertical resolution and to add lower-resolution levels for the remaining height up to about 100 km. A resolution of typically 0.5 km seems to be sufficient and would result in about 100 to 150 levels. Because of computational time constraints, this is not the preferred long-term solution but can be used to establish references for "accurate" values of the radiance.

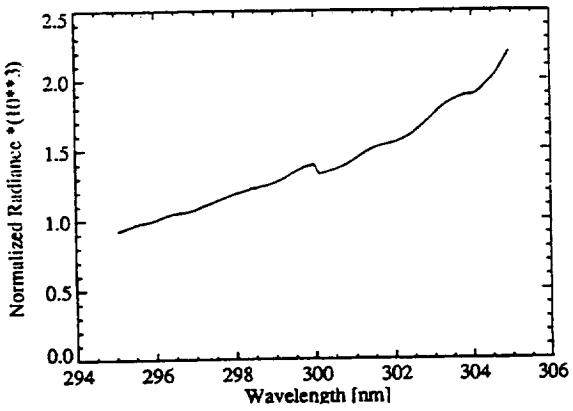

Figure 4. Radiance calculated with GOMETRAN before optimization of the selected altitude levels. The transition between different altitude grids is at 300 nm. Conditions for the atmosphere, the viewing geometry, and the computation are as in Figure 1 but with four Fourier terms.

The second approach to altitude grid selection optimizes, for a fixed lower number of levels, the positions of these levels in such a way that the accurate reference values calculated before can be matched by the radiance calculated with this lower number of levels. For GOMETRAN it has been established that the minimum number of levels should be about 50. As the finite difference method requires an odd number, 49 has been chosen as the optimum number for the altitude levels. The positions of these 49 levels are optimized to achieve agreement with an accurate 99-level reference calculation.

The choice of altitude levels is dependent on the vertical structure of the atmospheric composition. Different scenarios have been investigated to ensure that a set of optimized altitude levels is valid for all climatological conditions. Differences between the radiance calculated with the optimized levels and the "reference" radiances (based on 99 levels) are displayed in Table 2 for three of the scenarios (Antarctic ozone hole condition, northern midlatitude industrial pollution in the troposphere, and tropical biomass burning). Also presented are the differences between the reference radiances and those calculated with the original suboptimal levels (as used in Figure 4). It is evident that the optimization has been necessary for a 1% overall accuracy of the radiance. For each of the four wavelength ranges it has been possible to find common altitude levels for all scenarios investigated. Figure 5 shows for the example of the transition at 300 nm the smooth behavior of the radiance achieved after having optimized the altitude levels.

5.5. Radiance at the Line-of-Sight Angle

The "finite difference method" as described, for example, by *Lenoble* [1985] calculates the radiance only for the zenith stream angles used in the Gaussian quadrature of the integrals in the RTE. Interpolation or extrapolation would then be needed to obtain the radiance into the line-of-sight direction. This process causes considerable errors, especially with extrapolation as required with a direct nadir-viewing geometry.

To avoid this error, the line-of-sight angle has been added to the regular zenith stream angles with a zero weight. The result is, because of the zero weight, the maintenance of the Gaussian quadrature formula in conjunction with the additional calculation of the radiance into difference between the reference radiance calculated with 99 altitude levels and the radiance calculated with the optimized 49-level grid and between the reference radiance and the radiance calculated with the original, suboptimal 49-level grid. Conditions for the computation are 7 stream zenith angles, 4 Fourier terms and 20 Legendre polynomials.

(Scenario A) Antarctic ozone hole Trace gas profiles are based on the MPI database (*C. Brühl*, private communi-

Table 2. Comparison of Altitude Grids

	Difference (%): Reference - Optimized Grid			Difference (%): Reference - Suboptimal Grid		
λ, nm	Scenario A	Scenario M	Scenario T	Scenario A	Scenario M	Scenario T
274.9	0.1	0.3	0.4	2.2	0.2	0.8
275.1	0.2	0.2	0.4	1.5	2.9	1.9
299.7	0.1	0.1	0.8*	5.0	5.4	4.7
300.1	0.3	0.6	0.1	0.5	2.1	0.7
314.8	0.2	0.4	0.1	0.5	2.1	0.7
315.1	0.1	0.1	0.1	0.1	0.1	0.1
789.8	0.1	0.1	0.1	0.4	0.4	0.1

* Two additional levels at 3 and 7 km.

cation (hereinafter referred to as B92)) for 85°S and October but with a depletion of O_3 and NO_2 and an enhancement of BrO and ClO between 15 and 25 km altitude; maritime aerosols between 0 and 2 km, background aerosol types above; surface albedo 0.85; solar zenith angle 75°; relative azimuth angle between the Sun and the satellite 60°; line-of-sight zenith angle 43°.

(Scenario M) northern midlatitude industrial pollution Trace gas profiles are based on the MPI database for 55°N and January but with elevated levels of O_3, NO_2, SO_2, and HCHO in the boundary layer between 0 and 2 km; urban aerosols between 0 and 2 km, background aerosol types above; surface albedo 0.3; solar zenith angle 75°; relative azimuth angle between the Sun and the satellite 0°; line-of-sight zenith angle 30°.

(Scenario T) tropical biomass burning Trace gas profiles are based on the MPI database for 5°N and January but with elevated levels of O_3, NO_2, and HCHO in the troposphere; rural aerosols between 0 and 2 km, background aerosol types above; surface albedo 0.3; solar zenith angle 30°; relative azimuth angle between the Sun and the satellite 0°; line-of-sight zenith angle 30°; the direction of the line-of-sight angle. The computational time is increased because of larger matrix dimensions (by about 30% for seven regular stream angles), but the approach is much preferable over interpolation/extrapolation. Figure 6 presents a comparison between the radiance at the line-of-sight angle calculated directly as described above and calculated with an interpolation/extrapolation routine based on Legendre polynomials. It is obvious that errors exceeding the 1% accuracy requirement occur if the radiance is not calculated directly.

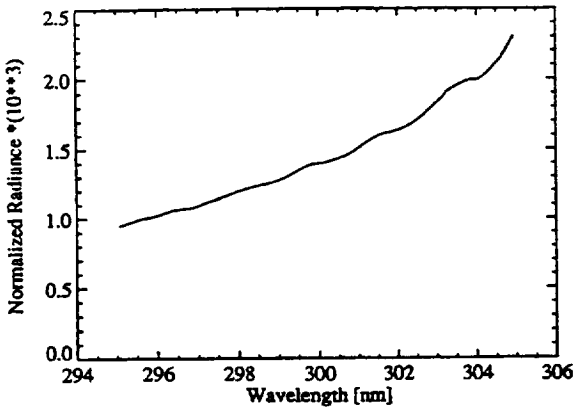

Figure 5. Radiance calculated with GOMETRAN after optimization of the selected altitude levels, otherwise as in Figure 4.

5.6. Frequency of the LU Decomposition

To solve the radiative transfer equation, GOMETRAN has to solve a system of equations that can be expressed in the form of a matrix whose dimensions are roughly equal to 400 by 400 in case of 50 altitude levels and 8 stream angles. The LU decomposition of the matrix performed to obtain this solution is the most time-consuming part of the computation. GOMETRAN can be operated in two modes: either in the monochromatic mode, where the set of equations is solved at every wavelength or in the more efficient "quasi-polychromatic" mode where a LU decomposition at the subsequent wavelength is only done when the norm of the new matrix has changed by more than a preset factor compared to the matrix norm at the previous wavelength. Through adjustment of this factor the frequency of matrix LU decompositions can be influenced. The computational speed is high for a small number of decompositions but at the expense of accuracy and vice versa.

The O_3 Huggins bands between 300 and 350 nm are the range with the most rapid changes of the optical properties with wavelength. A part of this range was selected to optimize the frequency of matrix decomposition. Reference values of backscattered radiances were calculated in the monochromatic mode with decomposition at each wavelength. Differences to the references are shown in Figure 7 for two conditions, first for decompositions at every 0.2 to 1 nm, secondly for decompositions every 2 to 10 nm. The second case leads to unacceptable errors of up to 3%. The first case with the more frequent decompositions represents a good compromise, with the accuracy level maintained to about 0.5% or lower.

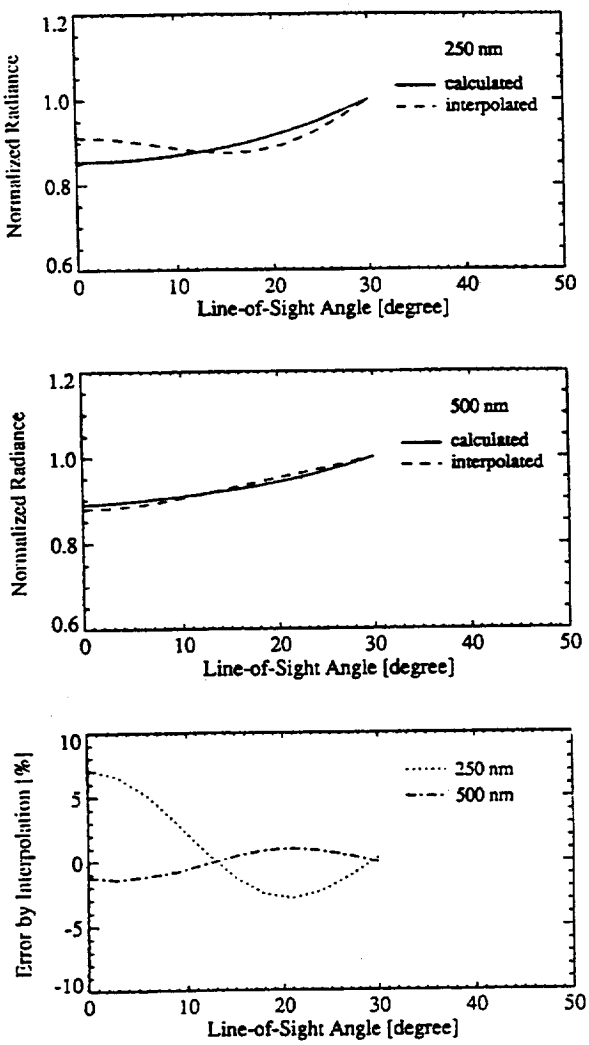

Figure 6. Direct calculation of the radiance at the line-of-sight angle versus interpolation/extrapolation. The normalized radiance for two wavelengths (top and middle figures) is displayed as function of the line-of-sight angle, obtained by direct calculation (solid line) and by Legendre interpolation/extrapolation (dashed line). The seven zenith stream angles used as basis in the interpolation/extrapolation process are 13.0°, 29.5°, 45.3°, 60.0°, 72.7°, 82.6°, and 88.5°. Also shown is the relative difference between the calculated and the interpolated radiances (bottom). Conditions for the atmosphere, the viewing geometry, and the computation are as in Figure 4 but with the line-of-sight angle being varied.

6. Comparison with Other Radiative Transfer Models

The plane-parallel GOMETRAN model has been validated against other radiative transfer models, especially against DISORT, which is a model based on the "discrete-ordinate method." DISORT in its present plane-parallel form is the result of more than 10 years development, the code is well documented and validated. The evaluation of DISORT is described thoroughly by *Stamnes and Swanson* [1981], *Stamnes and Dale* [1982], *Stamnes and Conklin* [1984], *Stamnes et al.* [1988], and *Lenoble* [1985]. It was shown that DISORT is accurate to 1% provided the computational parameters are chosen appropriately.

In DISORT the number of Fourier terms is determined automatically by a convergence criterion (which has been copied for GOMETRAN). The number of Legendre polynomials is set internally as twice the number of zenith stream angles. Typical numbers of streams (for the half space) in the evaluation of DISORT were 8 for moderately anisotropic atmospheres, and 16 or 24 when aerosol types are present with sharply peaked phase functions. For the aerosol types used so far in the GOMETRAN and DISORT test scenarios (maritime and tropospheric and stratospheric background aerosols), 7 streams were appropriate for both models. Optimized altitude grids were used for GOMETRAN, while for DISORT, optical depth grids with 99 levels were used in the ultraviolet and grids with 79 levels in the visible wavelength range.

6.1. Ultraviolet Wavelength Range

For the comparison between GOMETRAN and DISORT in the ultraviolet, radiances were calculated using GOMETRAN in the monochromatic mode. This is necessary to

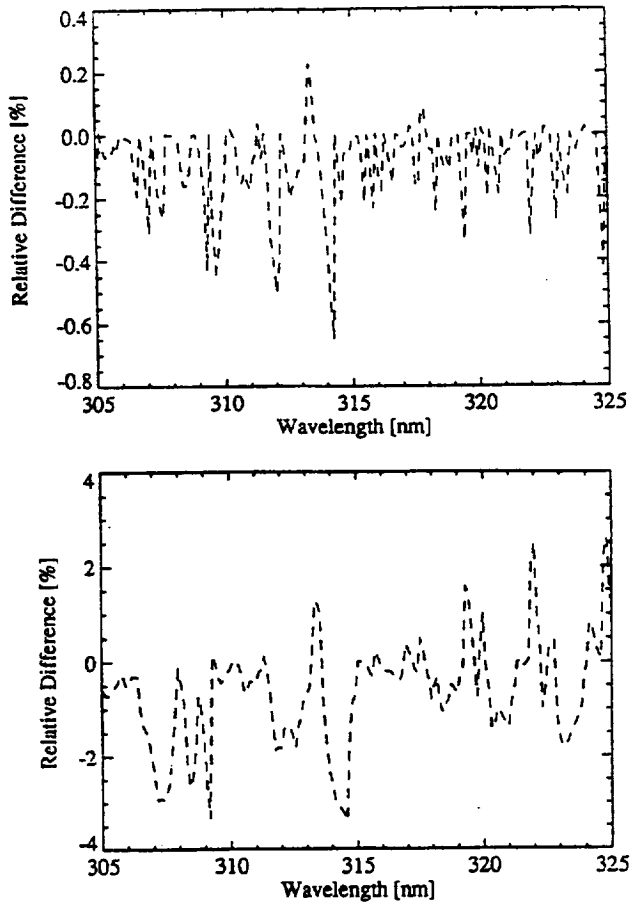

Figure 7. Difference between the GOMETRAN radiance calculated with matrix lower-upper (LU) decomposition at every GOME wavelength and the radiance obtained with a less frequent decomposition: one decomposition every 0.2 to 1 nm (top), one decomposition every 2 to 10 nm (bottom).

avoid unwanted errors caused by infrequent matrix LU decompositions in the Huggins bands between 300 and 350 nm. The agreement between both forward models is close to or better than 0.5% for a set of different viewing geometries, atmospheric conditions, and wavelength ranges, and it is expected that the differences between GOMETRAN and DISORT will stay within the 1% range for all possible scenarios.

Some comparisons were also made with a model developed at St. Petersburg University (*M. Birylina and V.V. Rozanov*, private communication, 1992), based on the "doubling and adding method." For a northern midlatitude scenario at a wavelength of 337 nm, a solar zenith angle of 45°, a number of line-of-sight and azimuth angles, and surface albedos between 0 and 1 the agreement was within 1%.

6.2. Visible Wavelength Range

The radiance calculated by GOMETRAN in the visible range shows good agreement with that from DISORT, with differences of less than 0.5%. Representative spectral ranges, atmospheric and viewing conditions were chosen for the investigations. Again, it is anticipated that under all possible conditions in the plane-parallel geometry an agreement of better than 1% can be achieved between GOMETRAN and DISORT.

A limited number of comparisons in the visible were made between GOMETRAN and two other accurate models, both based on the "doubling and adding method." The first model was that from St. Petersburg University, the second one is described by *Haan et al.* [1987] and (*P. Stammes*, private communication, 1993a). The St. Petersburg comparison with GOMETRAN at 650 nm for a northern midlatitude scenario with a solar zenith angle of 45° and a surface albedo of 0.5 produced an agreement of better than 1% for all possible line-of-sight and azimuth angles. Comparisons with the second doubling and adding model were performed for a northern midlatitude scenario and a solar zenith angle of 75°. The surface albedo is 0.3, and the line-of-sight and azimuth angles are 30° and 60°, respectively. Again, differences of less than 1% were observed at 450 and 650 nm.

7. Conclusion

A new radiative transfer model, GOMETRAN, has been developed for the ultraviolet, visible, and near-infrared wavelength range. It has been designed primarily as a tool for the data analysis of GOME measurements, but it can also be applied to other downward looking spaceborne sensors in this wavelength range. The model performs a computationally efficient calculation of radiances and weighting functions. The plane-parallel version of this model, which is applicable to geographical latitudes between 75°S and 75°N, has been presented in this paper. GOMETRAN has been optimized with respect to the calculation of radiances to achieve an accuracy close to 1%. Comparisons with other radiative transfer models (based on the discrete-ordinate and on the doubling-adding methods) have yielded agreement close to or better than 1% for all parts of the spectral range.

Future work on GOMETRAN, in addition to the already mentioned evaluation of the spherical version and the implementation of an approximative cloud treatment, will focus on two important issues: corrections for the polarization insensitivity of the model and the implementation of a procedure to take the so-called Ring effect into account. The following will briefly discuss these open tasks and possible ways for their solution.

GOMETRAN is an unpolarized model which neglects polarizing properties of the atmosphere in order to limit computational time requirements. The errors induced by this omission have been quantified by a radiative transfer model which can be operated both with and without polarization taken into account [*Haan et al.*, 1987], (*P. Stammes*, private communication, 1993b). Typical differences are negligible below 290 nm, then rise to a maximum of up to 5% in the O_3 Huggins bands, and decrease again toward longer wavelengths with values between 0 and 2% above 350 nm, depending on the atmospheric and viewing conditions. To exploit the Huggins bands for O_3 profile retrievals and other tasks, it will be necessary to correct the radiance calculated with GOMETRAN for polarization effects. One possibility here is the use of tables with correction factors which have to be applied to the unpolarized radiances. These tables would have to be created for a variety of atmospheric, surface, and viewing scenarios.

Another point of concern is the Ring effect, which can be mainly attributed to inelastic rotational Raman-scattering processes in the atmosphere. The most notable feature here is the filling of the solar Fraunhofer lines [*Grainger and Ring*, 1962]. This effect was shown to be significant in the analysis of ground-based spectroscopic measurements, where it is usually accounted for by an effective negative absorption coefficient [*Solomon et al.*, 1987]. This ignores the inelastic nature of the process and is an empirical approach based on a limited number of experimental observations. The appropriateness of this technique will be studied for satellite-based measurements or different approaches such as a correction by a single-scattering approximation of the Ring spectrum. An accurate treatment is computer intense and is therefore not considered for GOMETRAN.

Acknowledgments. The work presented in this paper has been funded in part by the University of Bremen, by the European Space Agency (ESA), the Deutsche Agentur für Raumfahrtangelegenheiten (DARA, contract 50 EP92 07), and by NATO. We thank Yu. Timofeyev from St. Petersburg University, Russia, for the cooperation throughout the project. Computational assistance has been provided by Kai-Uwe Eichmann at the University of Bremen, Germany. The subject of the paper has also been presented in an internal report for Serco Space, Southall, United Kingdom.

References

Barkstrom, B., A finite difference method of solving anisotropic scattering problems, *J. Quant. Spectrosc. Radiat. Transfer*, *16*, 725–739, 1976.

Berk, A., L. Bernstein, and D. Robertson, MODTRAN: A Moderate Resolution Model for LOWTRAN 7, *AFGL Tech. Rep. F19628-86-C-0079*, 38 pp., Air Force Geophys. Lab., Hanscom AFB, Mass., 1989.

Burrows, J., et al., *SCIAMACHY – A European Proposal for Atmospheric Remote Sensing from the ESA Polar Platform*, Max Planck Inst. for Chem., Mainz, Germany, 1988.

Burrows, J., et al., Global Ozone Monitoring Experiment: Interim Science Report, *Tech. Rep. SP–1151*, Eur. Space Agency, Eur. Space Res. and Technol. Cent., Noordwijk, Netherlands, 1993.

Clough, F. K., E. Shettle, and G. Anderson, Atmospheric radiance and transmittance: FASCOD2, in *Proceedings of the 6th Conference on Atmospheric Radiation*, pp. 141–144, Am. Meteorol. Soc., Boston, Mass., 1986.

Clough, F. K., G. Anderson, E. Shettle, J. Chetwynd, L. Abreu, L. Hall, and R. Worsham, FASCOD3: Spectral simulation, in *IRS '88: Current Problems in Atmospheric Radiation*, edited by J. Lenoble, and J. Geleyn, pp. 372–375, A. Deepak, Hampton, Va., 1989.

Grainger, J., and J. Ring, Anomalous fraunhofer line profiles, *Nature*, *193*, 762, 1962.

Haan, J., P. Bosma, and J. Hovenier, The adding method for multiple scattering calculations of polarized light, *Astron. Astrophys.*, *183*, 371–391, 1987.

Heath, D. F., A. J. Krueger, H. A. Roeder, and B. D. Henderson, The solar backscatter and total ozone mapping spectrometer (SBUV/TOMS) for Nimbus 7, *Opt. Eng.*, *14*, 323–313, 1975.

Isaacs, R., W.-C. Wang, R. Worsham, and S. Goldberg, Multiple scattering LOWTRAN and FASCODE models, *Appl. Opt.*, *26*, 1272–1281, 1987.

Isaacs, R., W.-C. Wang, R. Worsham, and S. Goldberg, Multiple Scattering Treatment for Use in the LOWTRAN and FASCODE Models, *Tech. Rep. AFGL-TR-86-0073, AD A173990*, Air Force Geophys. Lab., Hanscom AFB, Mass., 1989.

Kneizys, F., E. Shettle, L. Abreu, J. Chetwynd, G. Anderson, W. Gellery, J. Selby, and S. Clough, Users Guide to LOWTRAN 7, *Tech. Rep. AFGL-TR-86-0177*, Air Force Geophys. Lab., Hanscom AFB, Mass., 1986.

Lenoble, J., *Radiative Transfer in Scattering and Absorbing Atmospheres: Standard Computational Procedures*, 300 pp., A. Deepak, Hampton, Va., 1985.

Ridgway, W., R. Moose, and A. Cogley, Atmospheric Transmittance/Radiance Computer Code FASCOD2, *Tech, Rep. AFGL-TR-82-0392*m, Air Force Geophys. Lab., Hanscom AFB, Mass., 1982.

Rodgers, C., Retrieval of atmospheric temperature and composition from remote measurements of thermal radiation, *Rev. Geophys.*, *14*, 609–624, 1976.

Solomon, S., A. L. Schmeltekopf, and R. W. Sanders, On the interpretation of zenith sky absorption measurements, *J. Geophys. Res*, *92*, 8311–8319, 1987.

Stamnes, K., and P. Conklin, A new multi-layer discrete ordinate approach to radiative transfer in vertically inhomogeneous atmospheres, *J. Quant. Spectrosc. Radiat. Transfer*, *31*, 273–282, 1984.

Stamnes, K., and H. Dale, A new look at the discrete ordinate method for radiative transfer calculations in anisotropically scattering atmospheres. 2, intensity calculations, *J. Atmos. Sci.*, *38*, 2696–2706, 1982.

Stamnes, K., and R. Swanson, A new look at the discrete ordinate method for radiative transfer calculations in anisotropically scattering atmospheres, *J. Atmos. Sci.*, *38*, 387–399, 1981.

Stamnes, K., S.-C. Tsay, W. Wiscombe, and K. Jayaweera, Numerically stable algorithm for dicrete–ordinate–method radiative transfer in multiple scattering and emitting layered media, *Appl. Opt.*, *27*(12), 2502–2509, 1988.

D. Diebel, EUMETSAT, Am Elfengrund 45, D-64242 Darmstadt, Germany.

V.V. Rozanov and J.P. Burrows, Institut für Umweltphysik, Universität Bremen, Postfach 33 04 40, D-28334 Bremen, Germany. (e-mail: rozanov@gome5.physik.uni-bremen.de; burrows@gome5.physik.uni-bremen.de)

R.J.D. Spurr, DLR-DFD, Postfach 11 16, D-82230 Weßling, Germany.

(Received March 30, 1994; revised November 16, 1995; accepted May 10, 1996.)

Pergamon

J. Quant. Spectrosc. Radiat. Transfer Vol. 57, No. 4, pp. 467–476, 1997
Published by Elsevier Science Ltd. Printed in Great Britain
0022-4073/97 $17.00 + 0.00

PII: S0022-4073(96)00157-4

SATELLITE MEASUREMENTS OF ATMOSPHERIC OZONE PROFILES, INCLUDING TROPOSPHERIC OZONE, FROM ULTRAVIOLET/VISIBLE MEASUREMENTS IN THE NADIR GEOMETRY: A POTENTIAL METHOD TO RETRIEVE TROPOSPHERIC OZONE

K. V. CHANCE,[a] J. P. BURROWS,[b] D. PERNER,[c] and W. SCHNEIDER[d]

[a]Harvard-Smithsonian Center for Astrophysics, 60 Garden Street, Cambridge, MA 02138, U.S.A., [b]Institute of Remote Sensing, University of Bremen, Bremen, Germany, [c]Atmospheric Chemistry Division, Max Planck Institute for Chemistry, Mainz, Germany, and [d]Euromap GmbH, Neustrelitz, Germany

(Received 6 September 1996)

Abstract—Numerical studies of a new method for the retrieval of ozone profile information from nadir-observing satellite measurements in the ultraviolet and visible are presented. The method combines information from back scattered radiation in the Hartley band down to the O_3 concentration peak, lower atmospheric information from the temperature structure of the Huggins bands, and a constraint on the total column from the Chappuis bands. The Huggins bands' temperature structure provides altitude information on the ozone distribution that includes clear distinction between stratospheric and tropospheric ozone. Studies presented here include dependence of the retrieved O_3 profiles on surface albedo, tropospheric aerosol, and tropospheric O_3 content for a range of atmospheric conditions. Published by Elsevier Science Ltd

1. INTRODUCTION

The importance of the stratospheric ozone layer to terrestrial life and the need for precise long-term monitoring of the stratospheric ozone climatology are well established. Ozone also plays a significant role in the chemistry of the troposphere, where its photolysis leads to the production of OH, the most important tropospheric oxidizing agent.[1] Haagen-Smit et al[2] showed that the production of tropospheric ozone is dependent on the presence of hydrocarbons, oxides of nitrogen, and light. Crutzen[3] elucidated the mechanism for the HO_x- and NO_x-catalysed photochemical generation of ozone in the troposphere. The first experimental evidence that tropospheric ozone may be increasing was reported from balloon-sonde observations made between 1967 and 1982 at the meteorological station on Hohenpeissenberg in southern Germany.[4] An analysis of ozone measurements made at the clean air stations of Mauna Loa, Hawaii and Point Barrow, Alaska agreed with this finding and indicated an average increase of ozone of 0.5–1.5% per year during the period 1974–1989 with the largest increases occurring during summer.[5] Volz and Kley[6] investigated the ozone measurement technique used by Albert-Lévy and co-workers at Montsouris, near Paris, in the late 19th and early 20th centuries and concluded that the method is reliable.[7,8] These data indicate that the ozone mixing ratio in clean air was about 10 ppbv at the end of the last century near Paris. Present day surface measurements are a factor of 2–4 larger. As a result of such observations, concern about the impact of tropospheric ozone pollution is rapidly growing. To accurately assess the importance of these changes, global measurements of the distribution of tropospheric ozone are required.

Due to the relatively short lifetime and consequent variability of tropospheric ozone, measurements made by satellite-borne remote sensing instruments are the most efficient way to obtain global information on its distribution. A key difficulty in spaceborne monitoring of tropospheric ozone is the ability of the measurements and the retrieval approach to distinguish the contribution of stratospheric ozone from that of tropospheric ozone in the detected signals. A

method to determine the vertical distribution of stratospheric ozone by monitoring back scattered radiation in the ultraviolet Hartley and Huggins bands of ozone was first proposed by Singer and Wentworth in 1957,[9] and has been successfully applied by the BUV instrument on *Nimbus* 4 and the SBUV instrument on *Nimbus* 7.[10,11] SBUV obtains stratospheric profile information from the differing scattering depths, as well as the total ozone column, by measuring at 12 selected wavelength bands in the range 256–340 nm. The SBUV instrument uses relatively wide (1 nm) wavelength bands that do not resolve the fine structure of the ozone absorption. Stratospheric ozone vertical profiles, with limited geographical coverage, have also been obtained successfully using solar occultation by the SAGE I and II instruments.[12]

A method is presented here for remote sensing of ozone profiles, including tropospheric ozone, from orbiting spectrometers which measure upwelling atmospheric radiation between 240 and 800 nm. This study includes simulation of several viewing scenarios, as well as realistic estimation of instrument performance derived from studies for the Global Ozone Monitoring Experiment (GOME) and the SCanning Imaging Absorption spectroMeter for Atmospheric CHartographY (SCIAMACHY), since demonstrated by GOME, to infer the precision of the technique. The present work was instrumental in establishing the GOME and SCIAMACHY instrument programs, by demonstrating that nadir-looking instruments can measure tropospheric ozone globally. GOME is a European Space Agency instrument launched on the European Remote Sensing 2 satellite in April 1995. It is a nadir mapping instrument that views the Earth with continuous wavelength coverage from 240 to 790 nm at a resolution of 0.2 nm in the ultraviolet and 0.4 nm in the visible.[13–15] SCIAMACHY is a German/Dutch/Belgian instrument which is part of the payload for the ESA Envisat-1 Polar Platform, currently scheduled for launch in 1999. SCIAMACHY is an enhanced version of GOME having, in addition to nadir viewing, limb and occultation measuring modes, and extended wavelength coverage to 2.4 μm.[16–18]

2. SPECTROSCOPIC METHOD

The Huggins bands of ozone have discrete vibrational structure between 300 and 370 nm, with features having widths significantly less than 1 nm. This is the sharpest known vibrational structure of any electronic band of O_3. This structure has a strong temperature dependence due to the onset of thermal population of excited vibrational levels in the electronic ground state (see measurements in Refs. 19 and 20). It is this temperature-dependent structure that provides a spectral signature for tropospheric O_3; its differential character derives from the onset with increasing temperature of the weaker vibrational hot-band absorption between the stronger absorption peaks, which are due to absorption from $O_3(000)$.

The ozone measurement technique presented here includes the measurement of the Hartley, Huggins, and Chappuis bands at moderately high resolution (ca. 0.2 nm in the Hartley and Huggins bands, ca. 0.4 nm in the Chappuis bands). In addition to providing more continuous wavelength coverage for deriving information on vertical profiles from the scattering depth, it permits the use of the temperature structure of the Huggins bands to increase the altitude profile information. In particular, since tropospheric ozone is significantly warmer than stratospheric ozone at any altitude in the stratosphere where there is significant O_3, tropospheric ozone column amounts are cleanly separated from the stratospheric column. The Chappuis bands are temperature independent and occur at visible wavelengths where light penetrates to the ground under favorable meteorological conditions. Thus, their measurement provides improved total column O_3 information to the measurement set.

3. RADIANCE AND RETRIEVAL CALCULATIONS

3.1. *Forward radiance model*

Radiance calculations are performed for the present studies using the AFGL LOWTRAN7 radiance code.[21] The version of the code used here includes the correction of all recently discovered errata [G. P. Anderson and L. W. Abreu, private communications (1989–1992)]. The only modifications made to the code are to increase the number of significant figures for total radiance

provided by the code and for ozone concentrations read in by the code. All calculations are performed using the provided option for multiple scattering employing the k-distribution method.[22]

Calculations use a 12 layer (13 level) model atmosphere, including O_3, H_2O, and O_2, with concentrations from the AFGL atmospheric constituent profiles;[23] their model 6 atmosphere, with pressure and temperature corresponding to the U.S. Standard Atmosphere, is used. This model has a tropopause height of 15 km: subsequent references to tropospheric and stratospheric ozone refer to the column from 0 to 15 km and from 15 to 60 km, respectively (the error due to inclusion of the small mesospheric column, 50–60 km, with the stratosphere is negligible for present purposes). Calculations in this paper are performed for a satellite instrument in a polar orbit with a 10:00 a.m. crossing time, looking vertically down, at 45°N, for two viewing scenarios and tropospheric O_3 distributions: (1) vernal equinox, solar zenith angle = 53.5°, ground level O_3 mixing ratio = 40 ppbv ("normal" tropospheric ozone). In this case, the tropospheric ozone column is 63 Dobson units (DU, 1 DU = 2.687×10^{16} cm^{-2}) and the stratospheric column 276 DU; (2) summer solstice, solar zenith angle = 48.9°, ground level O_3 mixing ratio = 120 ppbv (corresponding to a boundary layer pollution episode under anticyclonic conditions). In this case, the tropospheric ozone column is 76 DU, and the stratospheric column 276 DU. The two ozone distributions are shown in Figs 1(a–h), along with the retrieved O_3 results described below. Contributions from minor interfering atmospheric species are not included in the present calculations. In the ultraviolet these include BrO, H_2CO, and SO_2. Measurements of these species simultaneous with ozone determinations, implying the appropriate correction of the spectra for analysis of ozone absorption, is intended. For example, stratospheric SO_2, greatly enhanced by the eruption of El Chichon, was measured by both the TOMS and SBUV instruments on *Nimbus* 7.[24–26] Clearly, the presence of interfering species, even when they are included in the retrieval process, will increase the uncertainty in derived ozone over that calculated here. The major interference for the Chappuis bands is from NO_2 and H_2O. These can both be readily corrected for, since the overlaps with the broad Chappuis bands are only partial, and since detailed study of the wavelength-dependent absorption by the Chappuis bands is not necessary; only their absorption in portions of the bands, cleanly separated from interfering species, is necessary to provide column O_3 measurements.

The studies include albedos of 0.3 (typical land value) and 0.02 (sea surface minimum) as specified in the input to LOWTRAN7. They also include rural and urban tropospheric aerosol extinction (IHAZE = 1 and 5 in LOWTRAN7). All studies have been done with the background stratospheric aerosol (IVULCN = 0 in LOWTRAN7). Clear sky conditions are assumed. The limitations to tropospheric ozone measurements due to cloud coverage are currently being studied extensively in the context of the GOME and SCIAMACHY satellite algorithm development. These studies include the knowledge of penetration depth of solar radiation into clouds gained from measurements in the oxygen A bands.[27–29]

3.2. Instrument modeling

The instrument model used in the present studies is a simple one developed in the preliminary stages of instrument and algorithm design for the GOME and SCIAMACHY projects. The instrument is assumed to measure the atmospheric spectrum over the O_3 regions at 0.2 nm resolution from 240 to 350 nm, and at 0.4 nm resolution from 400 to 800 nm (GOME and SCIAMACHY both include the 350–400 nm region as well, negligible for O_3; the GOME coverage ends at 790 nm, a negligible correction to the coverage in the present study). Spectra calculated with LOWTRAN7 are converted to the nanometer scale, appropriate for our measurements with dispersive instruments, and are corrected for resolution and for instrument parameters as follows: etendue = 5.0×10^{-5} cm^2 sr; instrument throughput = 0.15 for $\lambda \leqslant 400$ nm, = 0.20 for $\lambda > 400$ nm; detector quantum efficiency = 0.5; nadir sampling time = 1.5 sec (the GOME default nadir sampling time is 30 sec for $\lambda \leqslant 312$ nm and 1.5 sec for $\lambda > 312$ nm; for simplicity, and as a worst-case scenario, the present study is made using 1.5 sec sampling throughout the GOME wavelength range).

Synthetic noise is added to spectra calculated with the forward model for retrieval study purposes using the Box–Muller method for generating random deviates with a Gaussian distribution.[30] Noise sources include readout noise (10^3 e$^-$/pixel), dark current noise (10^2 e$^-$/pixel), photon statistics, and digitization noise. The digitization noise is calculated assuming 16-bit conversion, with gain factors

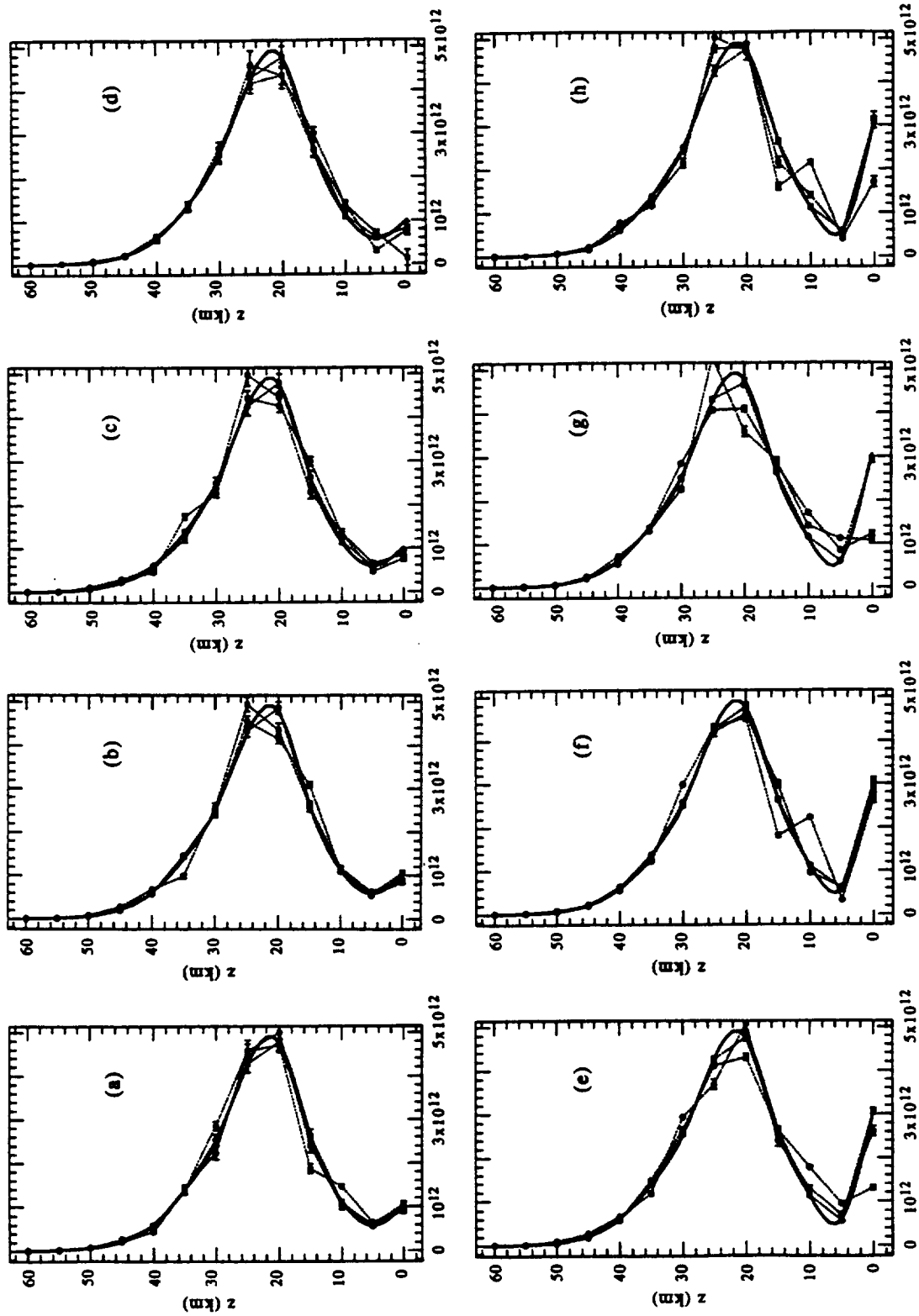

Fig. 1. The results of the fitting study for each of the eight atmospheric scenarios, and for three sets of initial concentrations for each scenario are shown. (——) are the modeled ozone concentrations. Retrieved values include 2σ fitting errors. The atmospheric scenarios are: (a) normal tropospheric ozone, rural haze, albedo 0.3; (b) normal tropospheric ozone, urban haze, albedo 0.3; (c) normal tropospheric ozone, rural haze, albedo 0.02; (d) normal tropospheric ozone, urban haze, albedo 0.02; (e) enhanced tropospheric ozone, rural haze, albedo 0.3; (f) enhanced tropospheric ozone, urban haze, albedo 0.3; (g) enhanced tropospheric ozone, rural haze, albedo 0.02; (h) enhanced tropospheric ozone, urban haze, albedo 0.02.

set appropriate to GOME measurements under conditions of maximum input. These range from 1.0×10^4 photons per pixel for $268 \leqslant \lambda < 312$ nm to 9.0×10^7 photons per pixel for $400 \leqslant \lambda < 800$ nm. Figure 2 is an example of the forward calculation, with noise added, corresponding to the measurement case with 40 ppbv tropospheric ozone, albedo = 0.3, and the rural haze model.

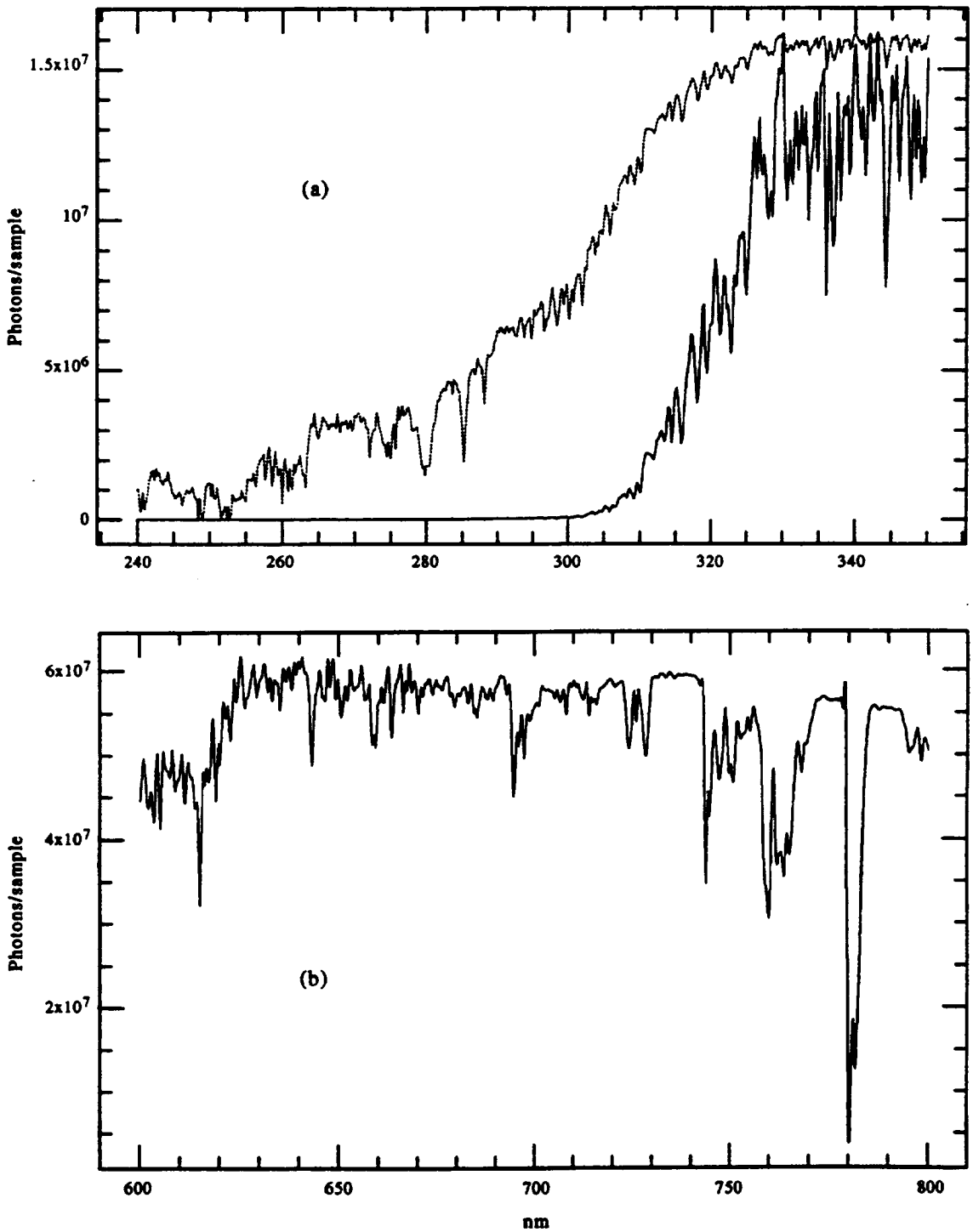

Fig. 2. An example of the forward calculation, with noise added, corresponding to the scenario with 40 ppbv tropospheric ozone, albedo = 0.3, and the rural haze model: (a) the Hartley–Huggins band region. Because of the large dynamic range of the spectrum its logarithm is also plotted (. . . .); (b) the Chappuis band region.

3.3. *Retrieval studies*

Figure 3 shows the ozone absorption cross sections for the Hartley, Huggins, and Chappuis bands at a representative temperature for the peak of the stratospheric ozone layer (220 K). These are calculated at the GOME/SCIAMACHY spectral resolution. The TOMS and standard (step

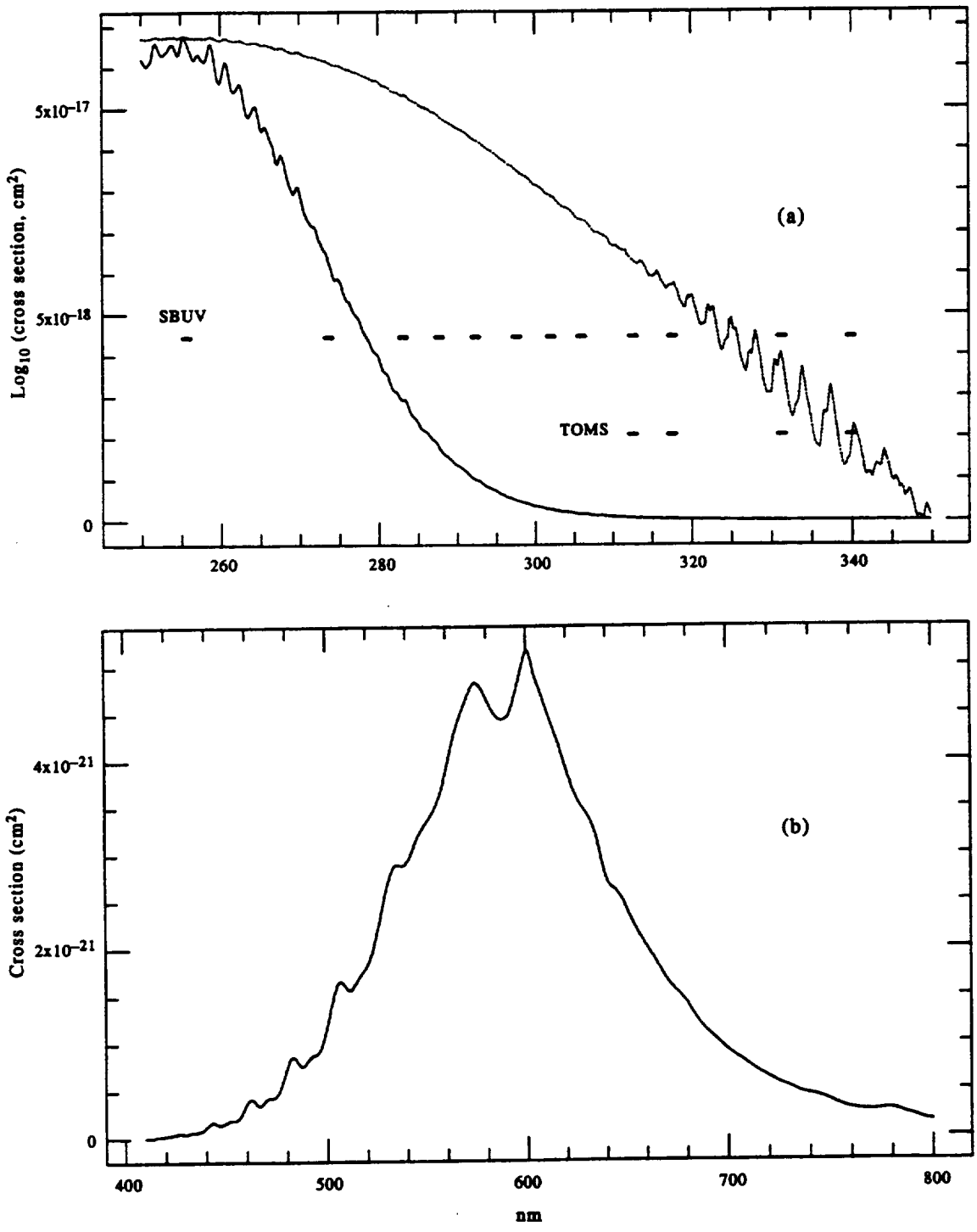

Fig. 3. Ozone absorption cross sections calculated at the GOME/SCIAMACHY spectral resolution. (a) The Hartley and Huggins bands at a representative temperature for the peak of the stratospheric ozone layer (220 K). The TOMS and standard (step scan mode) SBUV wavelength bands are also shown (TOMS also has channels at 360 and 380 nm). The strong variation in the strength for u.v. absorption, together with the approximate λ^4 dependence of the Rayleigh scattering, provides for discrimination of O_3 at different altitudes from the measurement of back scattered light at different wavelengths. (b) The Chappuis bands.

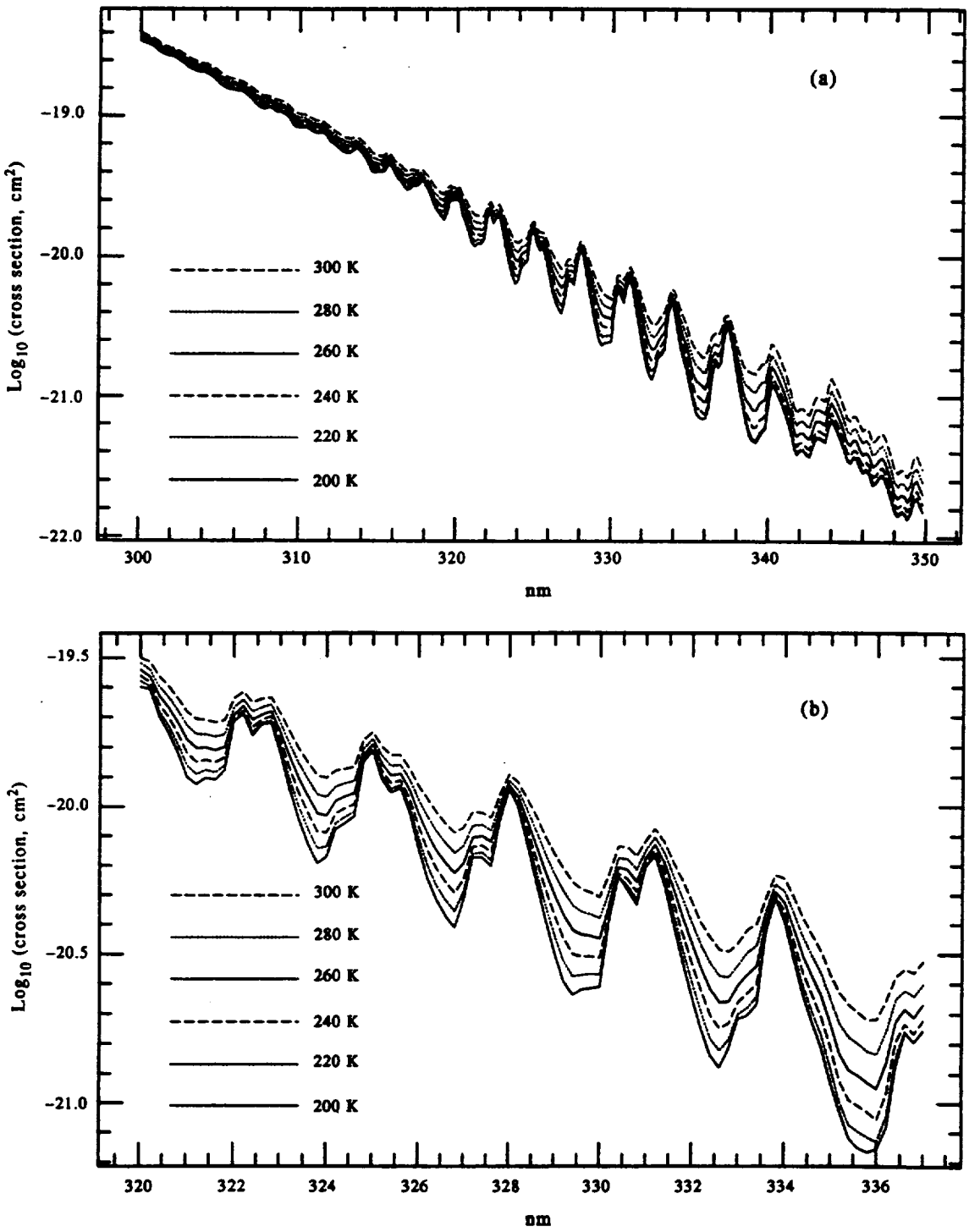

Fig. 4. (a) Temperature dependent cross sections in the O_3 Huggins bands calculated from the parameterization in the LOWTRAN7 code over the stratospheric and tropospheric ozone temperature range; (b) the same cross sections as Fig. 4(a), but only over the 320–337 nm range, to illustrate details of the temperature dependence in the region of primary importance for determination of tropospheric ozone.

scan mode) SBUV wavelength bands are also shown in the figure. The strong variation in the strength for u.v. absorption, together with the appropriate λ^4 dependence of the Rayleigh scattering, provides for discrimination of O_3 at different altitudes from the measurement of back scattered light at different wavelengths.

Precise measurements have been made of the temperature dependence of the Huggins bands from 300 to 340 nm.[19,20] The values of the cross sections derived from these measurements currently used

in the AFGL LOWTRAN7 radiance code are shown in Fig. 4(a) for the range of temperatures relevant to atmospheric ozone measurements. Less precise measurements exist to wavelengths longward of 340 nm, in the weaker part of the Huggins bands, and efforts are currently underway to provide precise laboratory measurements there as well. Figure 4(b) shows the same cross sections as Fig. 4(a), but only over the 320–337 nm range. The portion of the Huggins bands longward of 320 nm is the region of primary importance for determination of tropospheric ozone.

Calculated forward spectra, including the instrument model and noise, are generated as described in Sec. 3.2. Fitting studies are then performed on these synthetic spectra using the non-linear least squares technique.[31] Such an input spectrum is generated, with instrument parameters and noise, for each set of input conditions. These include (as detailed in Sec. 3.1) two choices of viewing scenario and ozone profile ("normal" and "polluted" troposphere), two choices of albedo (land surface average and sea surface minimum), and two choices of tropospheric aerosol distribution (rural and urban), for a total of eight input scenarios studied. The non-linear least-squares fitting analysis is then performed by allowing the O_3 concentration at each of the 13 atmospheric levels to vary independently in the forward model calculation while iterating to minimize the difference between the forward model calculation and the pre-computed forward spectrum plus noise. Iteration is continued until the calculated spectrum agrees in the least-squares sense with the input spectrum to within a specified χ^2 criterion or until all input parameters have stopped varying to within preset, small, amounts. Fitting is performed for each of the eight input scenarios, using three initial O_3 distributions. These are: (1) the normal input O_3 distribution; (2) the normal input O_3 distribution multiplied by 0.75, corresponding to 254 DU total ozone; and (3) the normal input O_3 distribution multiplied by 1.125, corresponding to 423 DU total ozone.

Non-linear least-squares fitting of data is not anticipated to be a part of the normal retrieval procedure for determination of O_3 profiles from satellite data; far too much computational time is required, even on advanced computers. This type of study has been used during the investigative phase of the GOME and SCIAMACHY to determine the maximal information that can be obtained from satellite measurements. Algorithm studies now being conducted include, among other elements, the use of look-up tables and the optimal estimation method[32,33] to design an efficient and accurate algorithm for retrieval of atmospheric gas amounts, including O_3 profiles, from the satellite measurements.

4. RESULTS AND DISCUSSION

Figures 1(a–h) shows the results of the fitting study for each of the eight input scenarios, and for the three sets of initial concentrations for each scenario. The concentrations for the input spectra and the 2σ fitting errors are included in the figure. Table 1 gives the integrated total ozone columns, as well as the tropospheric (i.e., $\leqslant 15$ km) and stratospheric (>15 km) columns, and their uncertainties, as derived from the fitting analysis.

The relative fitting uncertainties for tropospheric, stratospheric, and total ozone columns are substantially less than those for the individual derived levels. There is substantial correlation between ozone derived for adjacent levels, particularly in the troposphere. This is evident from examination of the correlation matrices derived in the least-squares fitting procedure (used to determine the uncertainties in the column amounts). There is also some suggestion of alternating behavior in fitting to adjacent altitude levels in Fig. 1. The fitting to the scenarios with enhanced tropospheric ozone shows a tendency to underestimate the ozone at the lowest altitude, compensating by placing it higher in the troposphere. The 5 km altitude resolution chosen for tropospheric retrievals in this study is probably near to the limit of what is feasible. An exception to this may be for ozone in a warm boundary layer where the temperature-induced contrast in the Huggins bands will be particularly pronounced. The U.S. Standard Atmosphere temperature and pressure profile used in these studies includes a very broad tropopause region (11–20 km). When atmospheric conditions with steeper temperature gradients in the tropopause region are encountered, ozone profiles might be retrievable to higher effective altitude resolution.

The ability to retrieve ozone profile information depends upon knowledge of the atmospheric temperature profile. The requirements for this knowledge have not been determined in the present study. Temperature knowledge to ± 5 K is estimated to be adequate, but this needs to be quantified

Table 1. Tropospheric, stratospheric, and total O_3 column retrievals.

Conditions			Normal tropospheric ozone†			Enhanced tropospheric ozone†		
			Troposphere	Stratosphere	Total	Troposphere	Stratosphere	Total
"True" profile			62.8	275.5	338.3	76.0	275.5	351.5
Albedo	Haze	Starting profile‡						
0.30	rural	1.00	61.9 ± 0.9	276.1 ± 0.6	337.9 ± 0.3	75.9 ± 0.5	275.6 ± 0.4	351.5 ± 0.2
0.30	rural	1.25	59.9 ± 1.1	277.5 ± 0.8	337.5 ± 0.5	78.1 ± 0.8	273.2 ± 0.7	351.2 ± 0.4
0.30	rural	0.75	63.8 ± 0.8	273.7 ± 0.6	337.4 ± 0.4	85.8 ± 0.5	267.3 ± 0.3	353.2 ± 0.2
0.30	urban	1.00	61.7 ± 0.6	276.2 ± 0.4	337.9 ± 0.4	76.0 ± 0.4	275.5 ± 0.3	351.5 ± 0.3
0.30	urban	1.25	63.2 ± 0.7	275.2 ± 0.5	338.4 ± 0.3	75.2 ± 0.5	275.8 ± 0.3	351.0 ± 0.3
0.30	urban	0.75	63.3 ± 0.5	274.1 ± 0.3	337.4 ± 0.3	76.8 ± 0.5	267.0 ± 0.2	343.8 ± 0.3
0.02	rural	1.00	62.4 ± 0.9	275.4 ± 0.7	337.8 ± 0.5	76.5 ± 0.5	275.1 ± 0.2	351.6 ± 0.3
0.02	rural	1.25	64.7 ± 1.0	274.0 ± 0.7	338.7 ± 0.5	83.2 ± 0.6	267.6 ± 0.3	350.8 ± 0.4
0.02	rural	0.75	64.3 ± 0.6	272.8 ± 0.5	337.1 ± 0.4	82.5 ± 0.6	268.4 ± 0.4	350.8 ± 0.5
0.02	urban	1.00	61.9 ± 1.0	275.5 ± 0.7	337.4 ± 0.9	76.0 ± 0.7	275.5 ± 0.4	351.5 ± 0.6
0.02	urban	1.25	60.9 ± 2.4	272.7 ± 0.7	333.6 ± 2.6	75.5 ± 0.8	274.6 ± 0.5	350.3 ± 0.7
0.02	urban	0.75	61.5 ± 0.8	272.6 ± 0.5	334.1 ± 0.7	71.0 ± 0.8	268.2 ± 0.5	339.3 ± 0.8

†2σ retrieval errors are given.
‡Multiplier for initial conditions (× "true" profile with normal tropospheric ozone).

in further studies. Limited retrievals were also performed using only the Hartley and Huggins band region, eliminating the Chappuis bands. In these cases, the uncertainties for tropospheric, stratospheric, and total ozone columns were about a factor of 10 higher. An attempt was made to retrieve profiles using only the Hartley band but, as expected, there was negligible sensitivity to lower atmospheric ozone.

5. CONCLUSION

It has been shown that nadir measurements of the ozone Hartley, Huggins, and Chappuis bands at sufficient spectral resolution to resolve the structure provides information on the altitude distribution of ozone, including tropospheric ozone. Altitude resolution in the troposphere is limited to ca. 5 km, except in special conditions. The studies here are limited to clear sky conditions; in practice, information could be derived down to the scattering height. These studies contributed to the decisions to produce several satellite instruments for atmospheric measurements. The first of these, GOME, is now operating successfully in orbit, producing data that should soon confirm the level to which this type of retrieval can be carried out practically.

Table 1 shows that the derived stratospheric and tropospheric ozone columns are cleanly separated to quite good precision, even with the caveat given above for strong correlation at the 5 km altitude resolution scale in the troposphere. Thus, under clear sky conditions, separate stratospheric and tropospheric columns are obtainable to high precision to within the limitations of the present study. While we do not anticipate that complete global coverage for tropospheric ozone will be routinely achieved by the satellite measurements we are undertaking, due chiefly to interference in the observations by clouds, we are confident that measurements of its global climatology will be greatly enhanced by these satellite measurements.

This type of measurement and analysis should also substantially improve the determination of the climatology of stratospheric ozone, since the interference in measurements by tropospheric ozone, including the confusion in analysis caused by the masking of tropospheric ozone by clouds, is removed by the clean separation achieved between stratospheric and tropospheric ozone determinations.

The studies for retrieval of ozone and other constituents from the GOME and SCIAMACHY instruments are currently in process. Clearly, the work discussed here is preliminary in the sense that many further atmospheric and instrumental complications, as well as details of retrieval theory, must be considered before a full retrieval procedure can be finalized. Practical application may well be limited by systematic effects, such as the uncertainty in radiometric calibration. The

results presented here are, however, an encouraging example of the power of utilizing modern array detector technology in satellite instruments for atmospheric constituent measurements. These efforts should lead to substantial improvement in the determination of the global distributions of ozone and other gases.

Acknowledgements—Research at the Smithsonian Astrophysical Observatory was supported by NASA Grant NAGW-2541. Research at the University of Bremen was partially funded by the Deutsche Agentur fuer Raumfahrtangelegenheiten, the European Space Agency, and the Max Planck Gesellschaft. We are grateful for the support and encouragement of our colleagues at the European Space Research and Technology Centre, particularly Drs C. J. Readings and A. Hahne, and Professor P. J. Crutzen at the Max Planck Institute for Chemistry.

REFERENCES

1. H. Levy, *Science* **173,** 141 (1971).
2. A. J. Haagen-Smit, E. F. Darley, M. Zaitlin, H. Hull, and W. Noble, *Plant Physio.* **27,** 18 (1951).
3. P. J. Crutzen, *Pure Appl. Geophys.* **106–108,** 1385 (1973).
4. W. Attmannspacher, R. Hartmannnsgruber, and P. Lang, *Meteorol. Rdsch.* **37,** 193 (1984).
5. S. J. Oltmans, W. D. Komhyr, P. R. Franchois, and W. A. Mathews, in *Ozone in the Atmosphere*, D. Bojkov and P. Fabian, eds. A. Deepak, Hampton, VA (1989).
6. A. Volz and D. Kley, *Nature* **332,** 240 (1988).
7. Albert-Lévy, *Annuaire de l'Observ. de Montsouris*, pp. 495–505, Gauthier-Villars, Paris (1878).
8. P. Miguel, *Annls. Obs. Mun.* **11,** 6 (1910).
9. S. F. Singer and R. C. Wentworth, *J. Geophys. Res.* **62,** 299 (1957).
10. D. F. Heath, A. J. Krueger, H. A. Roeder, and B. D. Henderson, *Opt. Eng.* **14,** 323 (1975).
11. J. E. Frederick, R. P. Cebula, and D. F. Heath, *J. Clim. Appl. Meteorol.* **24,** 904 (1985).
12. M. P. McCormick, J. M. Zawodny, R. E. Veiga, J. C. Larsen, and P. H. Wang, *Plan. Space Sci.* **37,** 1567 (1989).
13. J. P. Burrows, P. J. Crutzen, K. Chance, J. C. Geary, F. Goutail, G. W. Harris, G. K. Moortgat, C. Muller, D. Perner, U. Platt, J.-P. Pommereau, W. Schneider, and P. Simon, *SCIAMINI*, Max Planck Institut für Chemie, 55122 Mainz, Germany (1988).
14. K. V. Chance, J. P. Burrows, and W. Schneider, *Proc. S.P.I.E., Remote Sensing of Atmospheric Chemistry* **1491,** 151 (1991).
15. J. P. Burrows, K. V. Chance, A. P. H. Goede, R. Guzzi, B. J. Kerridge, C. Muller, D. Perner, U. Platt, J.-P. Pommereau, W. Schneider, R. J. Spurr, and H. van der Woerd, *Global Ozone Monitoring Experiment Interim Science Report*, T. D. Guyenne and C. Readings, eds. Report ESA SP-1151, ESA Publications Division, ESTEC, Noordwijk, The Netherlands, ISBN 92-9092-041-6 (1993).
16. J. P. Burrows, K. V. Chance, P. J. Crutzen, H. van Dop, J. C. Geary, T. J. Johnson, G. W. Harris, I. S. A. Isaksen, G. K. Moortgat, C. Muller, D. Perner, U. Platt, J.-P. Pommereau, H. Rodhe, E. Roeckner, W. Schneider, H. Sundqvist, and J. Vercheval, *The SCIAMACHY Project—A European Proposal for Atmospheric Remote Sensing*. Max Planck Institute für Chemie, 55122 Mainz, Germany (1988).
17. J. P. Burrows, W. Schneider, J. C. Geary, K. V. Chance, A. P. H. Goede, H. J. M. Aarts, J. de Vries, C. Smorenburg, and H. Visser, *Digest of Topical Meeting on Optical Remote Sensing of the Atmosphere*, Vol. 4, pp. 71–74, Optical Society of America, Washington, DC (1990).
18. J. P. Burrows and K. V. Chance, *Proc. S.P.I.E., Future European and Japanese Remote Sensing Sensors and Programs* **1490,** 146 (1991).
19. A. M. Bass and R. J. Paur, in *Atmospheric Ozone, Proceedings of the Quadrennial Ozone Symposium*, C. Zerefos and A. Ghazi, eds., pp. 606–616, D. Reidel, Hingham, MA (1985).
20. K. Yoshino, D. E. Freeman, J. R. Esmond, and W. H. Parkinson, *Planet. Space Sci.* **36,** 395 (1988).
21. F. X. Kneizys, E. P. Shettle, L. W. Abreu, J. H. Chetwynd, G. P. Anderson, W. O. Gallery, J. E. A. Selby, and S. A. Clough, *Users Guide to LOWTRAN7*, AFGL-TR-88-0177, AD A206773 (1988).
22. R. G. Isaacs, W.-C. Wang, R. D. Worsham, and S. Goldenberg, *Appl. Opt.* **26,** 1272 (1987).
23. G. Anderson, S. Clough, F. Kneizys, J. Chetwynd, and E. Shettle, Environmental Research Papers, No. 954, AFGL-TR-86-0110 (1986).
24. A. J. Krueger, *Science* **220,** 1377 (1983).
25. R. D. McPeters, D. F. Heath, and B. M. Schlesinger, *Geophys. Res. Lett.* **11,** 1203 (1984).
26. G. J. S. Bluth, S. D. Doiron, C. C. Schnetzler, A. J. Krueger, and L. S. Walter, *Geophys. Res. Lett.* **19,** 151 (1992).
27. J. Fischer and H. Grassl, *J. Appl. Meteorol.* **30,** 1245 (1991).
28. J. Fischer, W. Cordes, A. Schmitz-Peiffer, W. Renger, and P. Mörl, *J. Appl. Meteorol.* **30,** 1260 (1991).
29. A. Kuze and K. V. Chance, *J. Geophys. Res.* **99,** 14,481 (1994).
30. W. Press, B. Flannery, S. Teukolsky, and W. Vetterling, *Numerical Recipes*, Chap. 7, Cambridge Univ. Press, New York, NY (1986).
31. D. Marquardt, *J. Soc. Indust. Appl. Math.* **11,** 431 (1963).
32. C. Rodgers, *Rev. Geophys. Space Phys.* **14,** 609 (1976).
33. R. Munro, Middle atmosphere water vapour, Ph.D. thesis, Oxford Univ. (1991).

Pergamon

J. Quant. Spectrosc. Radiat. Transfer Vol. 58, No. 3, pp. 375–378, 1997
Published by Elsevier Science Ltd
Printed in Great Britain
0022-4073/97 $17.00 + 0.00

PII: S0022-4073(97)00002-2

IMPROVEMENT OF THE O_2 *A* BAND SPECTROSCOPIC DATABASE FOR SATELLITE-BASED CLOUD DETECTION

K. CHANCE

Harvard-Smithsonian Center for Astrophysics, 60 Garden Street, Cambridge, MA 02138, U.S.A.

(Received 19 June 1996)

Abstract—Detection of cloud parameters from space-based spectrometers can employ the vibrational bands of O_2 in the $b^1\Sigma_g^+ \leftarrow X^3\Sigma_g^-$ spin-forbidden electronic transition manifold, particularly the $\Delta v = 0$ *A* band. The European Space Agency's Global Ozone Monitoring Experiment (GOME), on board the European Remote Sensing 2 satellite, uses the *A* band in the Initial Cloud Fitting Algorithm (ICFA). The work reported here consists of making substantial improvements in the line-by-line spectral database for the *A* band, testing whether an additional correction to the line shape function is necessary in order to model correctly the atmospheric transmission in this band, and calculating prototype cloud and ground template spectra for comparison with satellite measurements. Published by Elsevier Science Ltd

1. SUMMARY OF NEW LABORATORY MEASUREMENT DATA

The measurements incorporated into the present work are from Refs. 1 and 2 (together, RW). They include improved measurements of line intensities, giving an overall band intensity that is 15% larger than the previous measurements that are the source of the parameters in the HITRAN92 listing [3,4]. It is worth noting that the uncertainties in Ref. 3 are given as 4%, while those of RW are 2%. The level of disagreement (arguably just a bit worse than 2σ) is an indication of how difficult these seemingly straightforward measurements actually are. RW also include self-broadening measurements of the linewidths, which are on the average 8% smaller than the air broadening values in HITRAN92 (the HITRAN92 values actually come from measurements in the *B* band [5], which were substituted for *A* band widths for lack of specific *A* band measurements (see Ref. 6 for a more detailed discussion). Measurements made at 294 K are presented by RW for lines up to *P*29*P*29 in the P branch and *R*27*R*27 in the R branch, except for the *R*21*Q*22 and *R*25*R*25 lines, which are blended together. The measurements also include air broadening studies for a selection of five lines. They find "roughly a 3% increase in broadening for air over pure O_2," although their Table II appears to indicate more like a 2% increase. Their 3% is adopted here, with a 2% uncertainty. The temperature dependence of the self broadening was measured for 24 lines, from *P*29*P*29 through *R*5*R*5, over the temperature range + 100 to − 20°C. The temperature coefficient, n, for the pressure broadening coefficients, determined by RW for the ensemble of lines measured, is 0.76(5) (where $\gamma(T) = \gamma(T_0) \times (T_0/T)^n$). This compares with the $\bar{n} = 0.72$ that can be obtained from the very limited data set assembled in Ref. 7.

Estimated (2σ) final uncertainties for the measurements are:

1. Intensity: 2%; directly from the RW band strength.
2. Pressure broadening coefficients: 2%; from 294 K individual line uncertainties (small), plus the N_2/O_2 correction (the dominant term).
3. n: 7%; directly from measurements, $\bar{n} = 0.76(5)$. This corresponds to less than 2% uncertainty in the broadening coefficient for the range of temperatures encountered in the lower and middle atmosphere. The root-sum-square of the various error terms in pressure broadening is 3%.

The data measured by RW can be extended to provide updated coefficients for use in cloud determination to replace the ones included in HITRAN92 [4], which have been shown to be insufficiently accurate for satellite-based cloud detection [6].

Processing of the RW data to provide a more complete data set is accomplished as follows:

1. Pressure broadening coefficients for the lines omitted due to interference are replaced by those with the same N', N'': $R21Q22$ and $R25R25$ are replaced by $R21R21$ and $R25Q26$.
2. O_2 pressure broadening coefficients measured by RW are multiplied by 1.03, to give air broadening. Coefficients for lines measured by RW in the $\upsilon = 0 \leftarrow 0$ band are also applied to the respective lines in the $\upsilon = 1 \leftarrow 1$ hot band and the $\upsilon = 0 \leftarrow 0$ band of $^{18}O^{16}O$. HITRAN92 lines not measured by RW are multiplied by 1.03/1.09009 = 0.94488, where 1.09009 is the average ratio of the RW measurements to the HITRAN92 coefficients.
3. The isotopic abundances are taken to be those used in HITRAN92, so that $^{16}O_2$ is 99.52% and $^{18}O^{16}O$ is 0.40%.
4. Intensity values for the three sub-bands are calculated starting with the 294 K band strength of RW, correcting the hot band by the Boltzmann factor of the band origin (1556.385 cm^{-1}) and the minor isotopic band by the appropriate isotopic ratio. The line intensities are translated to 296 K by explicitly calculating the rotation-spin partition functions using the term values from HITRAN92 and correcting for the RW approximation for the 294 K partition function of the major band.
5. In order to calculate individual line intensities, to supplement the measured ones, it is necessary to use the appropriate intensity formulas, which take into account the spin-rotation and spin-spin interactions [1,2,8]. For the $\upsilon = 0 \leftarrow 0$ band of $^{16}O_2$ measured by RW the molecular constants from Ref. 9 are used, to be consistent, although better constants are now available (Ref. 10 and references cited therein). These latter constants are used to calculate the individual line intensities for the $\upsilon = 1 \leftarrow 1$ band of $^{16}O_2$ and the $\upsilon = 0 \leftarrow 0$ band of $^{18}O^{16}O$.

The final database derived from these calculation is available from the author via ftp.

2. TESTING OF LINE SHAPES, INCLUDING LINE NARROWING COEFFICIENTS

RW determined that the data as measured under laboratory conditions at high spectral resolution ($< 10^{-4}$ cm^{-1}) were fitted better by including narrowing of the line core (Dicke narrowing) in the line shape function. Several line shapes were tested, including the Galatry line shape [11]. It was found that all of the tested line shapes which included line narrowing provided superior fits to those using the Voigt profile, and that all were equivalent to within experimental uncertainty. The Galatry profile was adopted for the bulk of the work because of the relative simplicity in implementing it [12]. RW found that all of the lines in the O_2 A band can be reasonably described by a line narrowing coefficient of 0.0145 cm^{-1} atm^{-1} (see RW for the exact definition of the coefficient in terms of the Galatry profile). An improved method for generating Galatry line profiles, employing the fast Fourier transform (FFT), has since been developed by Ouyang and Vargese [13] (OV). These authors have distributed a version of their FFT computer code, which was used in the present study for investigation of the effect of line narrowing on the atmospheric O_2 absorption. In order to use the code, it was necessary to update it and streamline it somewhat. The FFT routine used in the code is from the International Mathematical and Statistical Library (IMSL); however, calls were to an outdated version of IMSL, which is no longer supported at our institution (nor, presumably, at most others). Therefore, the code was updated to IMSL Version 10. The updated version of the Galatry line profile code is available from the author via ftp. Implementation of this code and atmospheric investigation for the O_2 A band proceeded as follows:

1. The OV code was compared in the Voigt limit against our standard Voigt subroutine (based upon algorithm 363 of the Collected Algorithms from CACM), which has an accuracy of 10 significant figures, for the case where the Lorentz half-width at half-maximum is 3.0 times the Gaussian half-width at 1/e intensity. The maximum disagreement was 0.13%; the maximum disagreement relative to the line center intensity was 0.06%. This was accepted as validation that the OV code can be properly used to assess the importance of line narrowing on the atmospheric O_2 spectrum.
2. Comparisons were made using the OV code with and without line narrowing for cases corresponding to the O_2 A band at 5 and 10 km altitudes in the atmosphere, using pressure and temperature values from the 1976 US Standard Atmosphere [14]. In the 5 km case, the maximum

relative error in the line shapes is 1.8%; differences go to < 1% by 2.9 Gaussian 1/e widths from line center. In the 10 km case, the maximum relative error is 2.4%; differences go to < 1% by 2.5 Gaussian 1/e widths from line center. In both cases, the integral of differences over the line shapes is zero to within the accuracy of the single precision calculations. In the atmosphere, these differences will be in the saturated central parts of the lines for all but the weakest lines. Differences greater than 1% are all within 0.02 GOME pixel (for example) so they will not be visible in the spectra. Thus, the effect of line narrowing should be totally negligible, and GOME analysis can simply use the Voigt profile for satellite-based cloud correction.

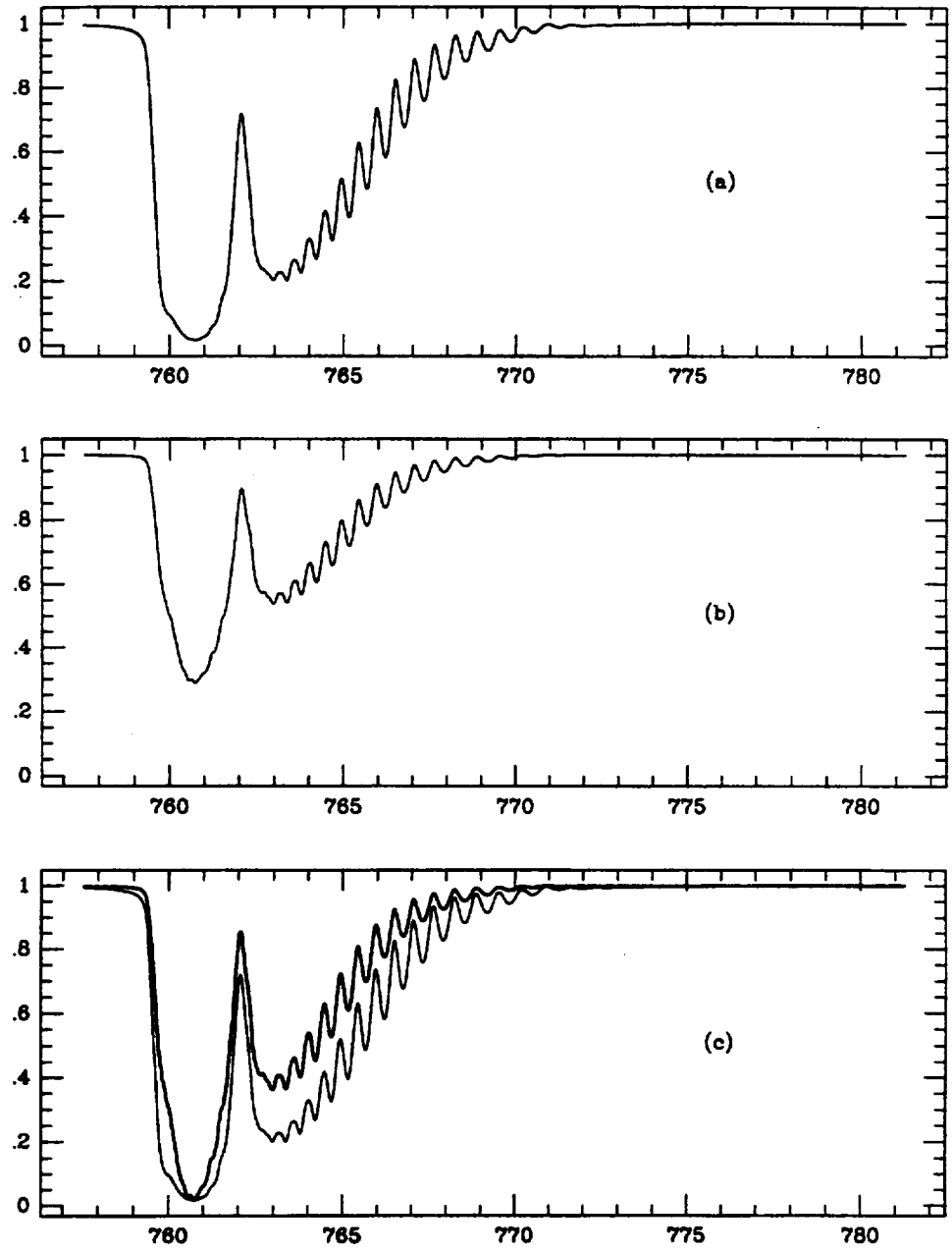

Fig. 1. Template spectra as used in the GOME Initial Cloud Fitting Algorithm. (a) is a sample ground template for GOME, *i.e.*, the measured spectrum for light reflected back from ground level (1013.25 mbar). (b) is sample template for reflection from a cloud surface at 400 mbar. (c) compares the shapes of the two templates to demonstrate the information available in distinguishing the relative level of light penetration from satellite spectra. The calculations are made for a solar zenith angle of 60° and a satellite viewing angle of 22°, for a total path multiplier of 3.07853.

3. SAMPLE O_2 *A* BAND CLOUD CORRECTION TEMPLATES FOR GOME

It has been shown that nadir-looking spectra of the O_2 *A* band from space can be used to determine cloud-top height and fractional cloud coverage when they are obtained with sufficiently high spectral resolution and low noise, and when the database of molecular parameters is sufficiently accurate [6]. The GOME satellite instrument [15] initially uses a more approximate technique to correct retrieved ozone abundances: Template spectra are prepared for the O_2 *A* band region for penetration of radiation to the ground and for penetration to standard cloud-top height; the effective cloud coverage is retrieved by linear least-squares fitting to determine the best coefficients for describing the measurements as a sum of the template spectra.

For initial comparisons with the GOME satellite data sample ground and 400 mbar cloud template spectra are calculated using a 16-layer atmosphere based upon the 1976 U.S. Standard Atmosphere [14] and employing Version 5 of the GOME key data for wavelength calibration and for the GOME compound hyperbolic slit function (Eq. (1)):

$$y = \frac{a_1^2}{(x - x_0)^2 + a_0^2} + \frac{a_2^2}{(x - x_0)^4 + a_0^2} + \frac{a_3^2}{(x - x_0)^6 + a_0^2} \quad (1)$$

where y is the normalized spectral response and x is the spectral position in pixel number. The current slit function values are $a_0 = 0.7334$, $a_1 = 0.0756$, $a_2 = 0.4689$, and $a_3 = 0.5589$. The calculations are made for a solar zenith angle of 60° and a viewing angle of 22°, for a total (typical) path multiplier of 3.07853, as initially used in the Initial Cloud Fitting Algorithm (ICFA) of GOME. Fig. 1(a) is the sample ground template, *i.e.*, the measured spectrum for light reflected back from ground level (1013.25 mbar). Fig. 1(b) is the sample template for reflection from a cloud surface at 400 mbar. Fig. 1(c) compares the shapes of the two templates to provide some feeling for the information available in distinguishing the relative level of light penetration from satellite spectra.

Acknowledgement—This research was supported by NASA grant NAGW-2541.

REFERENCES

1. Ritter, K. J., A high resolution spectroscopic study of absorption line profiles in the *A*-band of molecular oxygen. Ph.D. thesis, University of Maryland, 1986.
2. Ritter, K. J. and Wilkerson, T. D., *J. Molec. Spectrosc.* 1987, **121**, 1.
3. Miller, J. H., Boese, R. W. and Giver, L. P., *JQSRT*, 1969, **9**, 1507.
4. Rothman, L. S., Gamache, R. R., Tipping, R. H., Rinsland, C. P., Smith, M. A. H., Benner, D. C., Devi, V. M., Flaud, J.-M., Camy-Peyret. C., Perrin, A., Goldman, A., Massie, S. T., Brown, L. R. and Toth, R. A., *JQSRT*, 1992 **48**, 469.
5. Giver, L. P., Boese, R. W. and Miller, J. H., *JQSRT*, 1974 **14**, 793.
6. Kuze, A. and Chance, K. V., *J. Geophys. Res.* 1994 **99**, 14,481.
7. Chance, K. V., Traub, W. A., Jucks, K. W. and Johnson, D. G., *Int. J. IR MM Waves*, 1991, **12**, 581.
8. Watson, J. K. G., *Can. J. Phys.* 1968, **46**, 1637.
9. Albritton, D. L., Harrop, W. J. and Schmeltekopf, A. L., *J. Molec. Spectrosc.* 1973, **46**, 103.
10. Mizushima, M., Zink, L. R. and Evenson, K. M., *J. Molec. Spectrosc.* 1984, **107**, 395.
11. Galatry, L., *Phys. Res.* 1961, **122**, 1218.
12. Varghese, P. L. and Hanson, R. K., *Appl. Opt.* 1984, **23**, 2376.
13. Ouyand, X. and Varghese, P. L., *Appl. Opt.*, 1989, **28**, 1538.
14. U.S. Standard Atmosphere Supplements, 1976. U.S. Government Printing Office, Washington, DC.
15. Burrows, J. P., Chance, K. V., Goede, A. P. H., Guzzi, R., Kerridge, B. J., Muller, C., Perner, D., Platt, D., Pommereau, J.-P., Schneider, W., Spurr, R. J. and van der Woerd, H., *Global Ozone Monitoring Experiment Interim Science Report*, ed. Guyenne T. D. and Readings, C., Report ESA SP-1151, ESA Publications Division, ESTEC, Noordwijk, The Netherlands, ISBN 92-9092-041-6, 1993.

Ring effect studies: Rayleigh scattering, including molecular parameters for rotational Raman scattering, and the Fraunhofer spectrum

Kelly V. Chance and Robert J. D. Spurr

Improved parameters for the description of Rayleigh scattering in air and for the detailed rotational Raman scattering component for scattering by O_2 and N_2 are presented for the wavelength range 200–1000 nm. These parameters enable more accurate calculations to be made of bulk molecular scattering and of the Ring effect for a variety of atmospheric radiative transfer and constituent retrieval applications. A solar reference spectrum with accurate absolute vacuum wavelength calibration, suitable for convolution with the rotational Raman spectrum for Ring effect calculations, has been produced at 0.01-nm resolution from several sources. It is convolved with the rotational Raman spectra of O_2 and N_2 to produce an atmospheric Ring effect source spectrum. © 1997 Optical Society of America

1. Introduction

The phenomenon that has come to be known as the Ring effect was first noted by Grainger and Ring[1] as a filling in (broadening and reduction of depth) of solar Fraunhofer lines when viewed from the ground in scattered sunlight. Various processes have been proposed as contributing to the effect, including scattering with fluorescence from aerosols and from the ground.[2,3] However, the predominance of molecular scattering as the major cause was established by Kattawar *et al.*,[4] who analyzed the Ring effect contributions from rotational Raman scattering and inelastic Rayleigh–Brillouin scattering. The Rayleigh–Brillouin component is not of primary importance in satellite-based UV–visible backscatter measurements for which the present study is undertaken, and it is not analyzed here. The atmospheric scattering situation is nicely defined by Young[5]: "To summarize: molecular scattering consists of Rayleigh scattering and vibrational Raman scattering. The Rayleigh scattering consists of rotational Raman lines and the central Cabannes line. The Cabannes line is composed of the Brillouin doublet and the central Gross or Landau–Placzek line. None of the above is completely coherent. The term 'Rayleigh line' should never be used." Note that the vibrational Raman contribution results in lines so widely separated from the frequency of the incoming light that they are not normally considered part of the Ring effect, although in recent applications the Ring effect has developed a somewhat broader definition that includes substantial interfering structure in observations, rather than the initial effect that was limited to the broadening of partially resolved lines.

Understanding the Ring effect has become more important in recent years with the increase in ultraviolet and visible spectroscopic observations of the Earth's atmosphere from the ground[6,7] and from satellites.[8–12] To retrieve abundances of trace species from such observations, it is necessary to take the Ring effect into account. Methods have been developed to do so by pragmatic means: by measuring the polarization of scattered sunlight[6] and by modeling the effect directly from molecular scattering processes.[7,10] It has been proposed to use the Ring effect with selected Fraunhofer lines (in particular, the Ca II H and K lines) to determine cloud parameters in conjunction with satellite-based observations of O_3.[11] Joiner *et al.*[10] also determined that the contribution to the Ring effect from the Rayleigh–Brillouin scattering process is negligible for most geometries used in satellite observations.

The use of visible bands of O_2, in particular the 762-nm *A* band, for determination of cloud parameters is being developed for proposed and existing satellite instruments that monitor the atmosphere with

The authors are with the Smithsonian Astrophysical Observatory, 60 Garden Street, Cambridge, Massachusetts 02138.

Received 3 July 1996; revised manuscript received 23 December 1996.

0003-6935/97/215224-07$10.00/0

Table 1. Relative Rayleigh and Raman Scattering Intensities[a]

V Polarization in	*H* Polarization in	Sum (Natural Light in)
Rayleigh–Brillouin		
${}^{V}C_V = 180 + 4\epsilon$	${}^{H}C_V = 3\epsilon$	${}^{0}C_V = 180 + 7\epsilon$
${}^{V}C_H = 3\epsilon$	${}^{H}C_H = 3\epsilon + (180 + \epsilon)\cos^2\theta$	${}^{0}C_H = 6\epsilon + (180 + \epsilon)\cos^2\theta$
${}^{V}C_0 = 180 + 7\epsilon$	${}^{H}C_0 = 6\epsilon + (180 + \epsilon)\cos^2\theta$	${}^{0}C_0 = (180 + 13\epsilon) + (180 + \epsilon)\cos^2\theta$
		$\rho_0{}^{C} = 6\epsilon/(180 + 7\epsilon)$
Raman		
${}^{V}W_V = 12\epsilon$	${}^{H}W_V = 9\epsilon$	${}^{0}W_V = 21\epsilon$
${}^{V}W_H = 9\epsilon$	${}^{H}W_H = 9\epsilon + 3\epsilon\cos^2\theta$	${}^{0}W_H = 18\epsilon + 3\epsilon\cos^2\theta$
${}^{V}W_0 = 21\epsilon$	${}^{H}W_0 = 18\epsilon + 3\epsilon\cos^2\theta$	${}^{0}W_0 = 39\epsilon + 3\epsilon\cos^2\theta$
		$\rho_0{}^{W} = 6/7$
Sum		
${}^{V}T_V = 180 + 16\epsilon$	${}^{H}T_V = 12\epsilon$	${}^{0}T_V = 180 + 28\epsilon$
${}^{V}T_H = 12\epsilon$	${}^{H}T_H = 12\epsilon + (180 + 4\epsilon)\cos^2\theta$	${}^{0}T_H = 24\epsilon + (180 + 4\epsilon)\cos^2\theta$
${}^{V}T_0 = 180 + 28\epsilon$	${}^{H}T_0 = 24\epsilon + (180 + 4\epsilon)\cos^2\theta$	${}^{0}T_0 = (180 + 52\epsilon) + (180 + 4\epsilon)\cos^2\theta$
		$\rho_0{}^{T} = 6\epsilon/(45 + 7\epsilon)$

[a]Mostly from Kattawar *et al.*, 1981.

emphasis on tropospheric measurements.[13] This includes the European Space Agency's global ozone monitoring experiment (GOME) and the upcoming scanning imaging absorption spectrometer for atmospheric chartography (SCIAMACHY). The Ring effect has a substantial influence on such observations; work is under way in our institution to refine and model the effects. In this case, the effect is due to inelastic scattering in molecular absorption lines themselves rather than in the solar Fraunhofer lines. Similar effects have been noted for the detailed retrieval of trace species including O_3 and NO_2.[6,7,12]

This study is part of an ongoing effort to quantify the Ring effect for atmospheric radiative transfer modeling, with application to satellite- and ground-based measurements, and to apply it to particular cases such as detailed absorption in the visible O_2 bands, the retrieval of tropospheric O_3 from UV measurements, and retrieval of trace photochemically active gases. Much of the previous modeling work[7,10,14] has relied on the development of molecular parameters for N_2 and O_2 by Penney *et al.*[15]; only one study[10] has used the updated dynamic polarizability anisotropies as developed by Bates.[16] Previous research has largely ignored the complication of the rotational Raman spectrum of O_2 caused by the electronic spin angular momentum in the ${}^3\Sigma_g^-$ ground state and the issue of pressure broadening of the rotational Raman lines. In this publication, we update the molecular parameters and the scattering with respect to the solar Fraunhofer spectrum using the best currently available laboratory and field data and theoretical studies of which we are aware. This provides an updated expression for Rayleigh scattering by air, expressions for the wavelength-dependent polarizability anisotropies of O_2 and N_2, accurate Placzek–Teller coefficients (the state-dependent factors in the line intensities) for O_2 rotational Raman lines (the Placzek–Teller coefficients of Penney *et al.*[15] for N_2 are correct as given), a tentative set of pressure-broadening coefficients for the O_2 and N_2 rotational Raman lines, a solar reference spectrum for convolution with calculated Ring cross sections, and a convolved Fraunhofer-rotational Raman source spectrum for fitting of atmospheric spectra. The tables and spectra are not included here because of size limitations, but they are available from the authors.

2. Rayleigh Scattering

To examine the detailed Rayleigh and rotational Raman scattering properties, including their relative intensities and the scattering phase functions, we begin with Table I of Kattawar *et al.*,[4] which describes the relative intensities and angular behaviors for the Rayleigh–Brillouin and rotational components and their sum. They are given for various input polarizations, including unpolarized light (the predominant contribution for many atmospheric observations for which single scattering is the major contributor to the Ring effect). For unpolarized light, the depolarization ratios (defined in each case as the ratio of the horizontally polarized component to the vertically polarized component at a 90° scattering angle) can be determined directly. Table I of Kattawar *et al.*[4] is reproduced here as Table 1, with the addition of depolarization ratios for three cases: Rayleigh–Brillouin (the central Cabannes component *C*); rotational Raman (the wings *W*); and the sum of the two (*T* for total). The phase functions for scattering can also be derived for each case. They are (normalized over solid angle to 1)

$$\Phi_0{}^{C} = \frac{3}{160\pi}\left[\frac{(180 + 13\epsilon) + (180 + \epsilon)\cos^2\theta}{18 + \epsilon}\right],$$

$$\Phi_0{}^{W} = \frac{3}{160\pi}(13 + \cos^2\theta),$$

$$\Phi_0{}^{T} = \frac{3}{80\pi}\left[\frac{(45 + 13\epsilon) + (45 + \epsilon)\cos^2\theta}{9 + 2\epsilon}\right], \quad (1)$$

where $\epsilon = (\gamma/\bar{\alpha})^2$, γ is the anisotropy of the polarizability, and $\bar{\alpha}$ is the average polarizability. In each

case, the phase function is given in terms of the respective depolarization ratio ρ_0^X ($X = C, W, T$) by

$$\Phi_0^X = \frac{3}{8\pi}\left[\frac{(1+\rho_0^X)+(1-\rho_0^X)\cos^2\theta}{2+\rho_0^X}\right]. \quad (2)$$

The Rayleigh scattering cross section at standard temperature (273.15 K) and pressure (1 atm) is given by

$$Q_R = \frac{32\pi^3(n-1)^2F_K}{3N_0^2\lambda^4}, \quad (3)$$

where n is the index of refraction, F_K is the King correction factor,[17] N_0 is Loschmidt's number (2.686763×10^{19} cm^{-3}), and λ is the wavelength. The King correction factor is given by

$$F_K = 1 + 2\left(\frac{\gamma}{3\bar{\alpha}}\right)^2 = \frac{6+3\rho_0^T}{6-7\rho_0^T} = 1 + \frac{2\epsilon}{9}. \quad (4)$$

The average polarizability can be determined from the relation

$$|\bar{\alpha}|^2 = \frac{(n-1)^2}{4\pi^2N_0^2}. \quad (5)$$

3. Molecular Parameters

A. Rayleigh Scattering Cross Sections

The major source of improved data for the indices of refraction of O_2, N_2, and air versus wavelength, the King correction factors, and the anisotropies of the polarizabilities is Bates.[16] He presented a comprehensive review of both measurements and theoretical calculations and derived a data set that was demonstrated to be better than 1% for all the data and parameterizations utilized in the this study.

Bates's Table 1 gives refractive indices, Rayleigh-scattering cross sections, and King correction factors versus wavelength for air from 200 to 1000 nm. We found that the following Edlén-type expression fits the index of refraction data to better than 0.1% for all values:

$$(n_{\text{air}} - 1) \times 10^4 = 0.7041 + \frac{315.90}{157.39 - \sigma^2} + \frac{8.4127}{50.429 - \sigma^2}, \quad (6)$$

where $\sigma(\mu\text{m}^{-1}) = 1/\lambda\ (\mu\text{m})$. The Rayleigh cross sections are reproduced to 0.3% rms (worst case, 0.5%) over the full 0.2–1-μm range by the expression

$$Q_R \times 10^{24}(\text{cm}^2) = \frac{3.9993 \times 10^{-4}\sigma^4}{1 - 1.069 \times 10^{-2}\sigma^2 - 6.681 \times 10^{-5}\sigma^4}. \quad (7)$$

Nicolet[18] gave an expression for fitting the data of Bates to 0.5% over the 0.2–0.55-μm range; the current expression is slightly more accurate and extends over a larger wavelength range (also see Bucholtz[19]). The King factor and depolarization ratio for any choice of wavelength within the 0.2–1.0-μm range can be accurately determined from the previous two equations.

B. Polarizability Anisotropies

The previous expansions are for air, including standard amounts of Ar and CO_2. For rotational Raman cross sections, we limit the calculations to O_2 and N_2. Bates gave segmented representations for the indices of refraction of O_2 and N_2 versus wavelength and expansions for the respective King correction factors. Tables giving the King correction factors, values of $\sqrt{\epsilon}$, index of refraction $\bar{\alpha}$, and γ for O_2 and N_2 have been derived in this study. Values of γ_{O_2} from these data are fitted to 0.6% rms over this wavelength range (1% worst case) by

$$\gamma_{O_2} \times 10^{24} = 0.07149 + \frac{45.9364}{48.2716 - \sigma^2}. \quad (8)$$

The γ_{N_2} values are fitted to 0.02% rms (0.04% worst case) by

$$\gamma_{N_2} \times 10^{25} = -6.01466 + \frac{2385.57}{186.099 - \sigma^2}. \quad (9)$$

These equations should be considered merely as phenomenological fits over a particular wavelength range, rather than trying to attach physical importance to, for example, the negative value of the constant term in the N_2 equation. They should not be extrapolated to outside the 0.2–1.0-μm range.

C. Basic Spectroscopy

The ground state of O_2 is $^3\Sigma_g^-$; it has significant electronic structure in both its magnetic dipole rotational spectrum and its rotational Raman spectrum. Rotational Raman spectra of both O_2 and N_2 have previously been approximated by simple expansions in the lowest rotational parameters (for positions) and by using T/c_2B_0 for the rotational partition functions. Precise data are now available for the term energies, allowing line positions and Boltzmann factors to be calculated accurately and rapidly. The use of term values from the current HITRAN listing[20] allows for calculations of line positions to 0.0001-cm^{-1} accuracy and for highly accurate calculation of statistical partitioning.

D. Placzek–Teller Coefficients

Cross sections for rotational Raman scattering are given by

$$Q_{N,N'}^W(\text{cm}^2) = \frac{256\pi^5}{27(\lambda')^4}\gamma^2 f_N c_{PT}(N, J, N', J'), \quad (10)$$

where f_N is the fractional population in the initial state. The quantum state-dependent factors in the cross sections $c_{PT}(N, J, N', J')$ are commonly known as Placzek–Teller coefficients from the initial derivations.[21] These factors are given for a molecule in a Σ electronic state with one electronic spin angular mo-

mentum in the Hund's case b coupling scheme (electron spin coupled to rotational angular momentum) by

$$c_{PT}(N, J, N', J') = (2N + 1)(2N' + 1)(2J' + 1) \times \begin{pmatrix} N & L & N' \\ 0 & 0 & 0 \end{pmatrix}^2 \begin{Bmatrix} N & L & N' \\ J' & S & J \end{Bmatrix}^2, \quad (11)$$

where J is the total angular momentum, S is the electronic spin angular momentum (1 for O_2 and 0 for N_2), and L is the component of the 2nd rank polarizability tensor responsible for the interaction. $L = 0$ for the isotropic part of the polarizability (the Cabannes component), and $L = 2$ for the anisotropic part of the polarizability (Raman scattering). The standard definitions for 3-j and 6-j coefficients are used. Two near equivalents to this equation give the formula for line strengths. These include the initial state degeneracy.[22,23] For $S = 0$ (i.e., N_2), Eq. (11) reduces to the result of Eq. (7) in Ref. 15:

$$c_{PT}(J \rightarrow J + 2) = \frac{3(J + 1)(J + 2)}{2(2J + 1)(2J + 3)},$$

$$c_{PT}(J \rightarrow J) = \frac{J(J + 1)}{(2J - 1)(2J + 3)},$$

$$c_{PT}(J \rightarrow J - 2) = \frac{3J(J - 1)}{2(2J + 1)(2J - 1)}. \quad (12)$$

This derivation gives correct Placzek–Teller coefficients for N_2 but approximates those for O_2 by treating it as a pure Hund's case b molecule. At low N and J, the departures from the pure coupling case that are due to the electron spin-rotation interaction are enough to affect the spectrum significantly.[22,24] In the classic study of the O_2 ground state, Tinkham and Strandberg[25] include the correct eigenvectors of the secular determinant for levels to as high as $J = 26$ in the case b basis set (their Table V and Eq. 54). Above this level, the molecule is described by case b behavior to a high degree of accuracy. For $J = 0$ and all odd J levels, the case b description is exact. For even J levels, $J \neq 0$, the transformation from case b basis functions $\phi_{N,J}$ to eigenfunctions $\Psi_{N,J}$ is given by

$$\Psi_{J-1,J} = b_J\phi_{J-1,J} - d_J\phi_{J+1,J}$$

$$\Psi_{J+1,J} = d_J\phi_{J-1,J} + b_J\phi_{J+1,J}. \quad (13)$$

The b_J and d_J values from Ref. 25 are used here to calculate correct Placzek–Teller coefficients for values to as high as $J = 10$, above which the corrections become completely negligible. An almost identical result was determined by Altmann *et al.*,[26] who calculated eigenvectors for the secular determinant and molecular parameters given in the slightly earlier work of Mizushima and Hill.[27] The database calculated with the corrected eigenvectors is prepared with an intensity cutoff to include all rotational Raman lines with intensities at 296 K within 0.1% of the strongest line. Because of the mixing of states, this now includes two $\Delta N = 4$ transitions. Figure 1 gives rotational Raman cross sections for N_2 and O_2 calculated for a temperature of 250 K and an excitation wavelength of 440 nm, appropriate to investigations of the effect of the Ring effect on retrievals of atmospheric NO_2 concentrations.

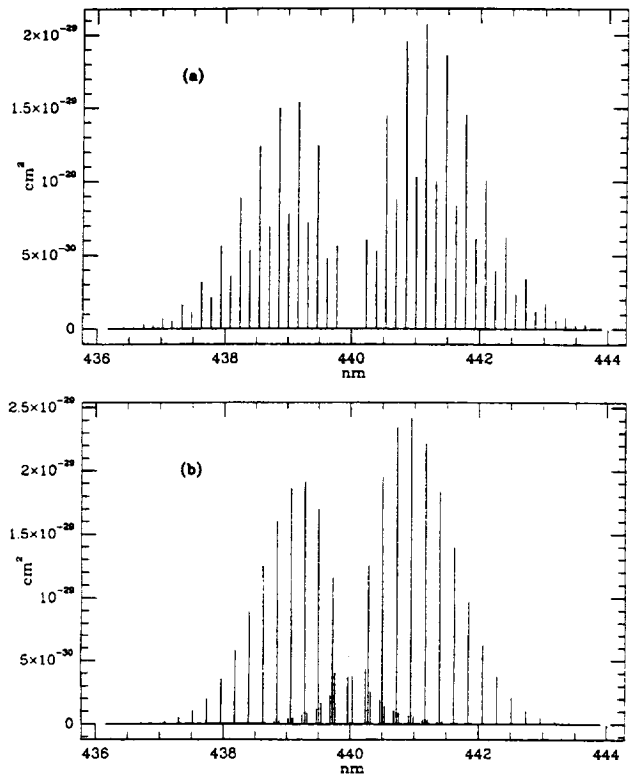

Fig. 1. Rotational Raman cross sections for (a) N_2 and (b) O_2 calculated for a temperature of 250 K and an excitation wavelength of 440 nm, appropriate to investigations of the effect of the Ring effect on retrievals of atmospheric NO_2 concentrations. The cross sections in this figure do not include the relative abundances of N_2 and O_2 in air.

E. Pressure-Broadening Coefficients

The capital letter Γ is used here to denote the half-width at half-maximum pressure-broadening coefficient to distinguish it from the γ used for anisotropy of polarizability. The best existing measurements of pressure broadening for the rotational Raman lines are from Jammu *et al.*[28] who noted some evidence that the unresolved Q branches of vibrational Raman bands seem to broaden less than lines caused by ordinary dipole transitions but that the rotational Raman lines broaden comparably to dipole transitions. They present self-broadening measurements for N_2, O_2, CO_2, and CO, as well as He and Ar broadening of N_2, O_2. All the measurements were made at room temperature. Given the experimental conditions (high pressures, modest spectral resolution) and the lack of air-broadening measurements, temperature dependences, and a tabulation of the J-dependent N_2 broadening coefficients, it was decided not to use

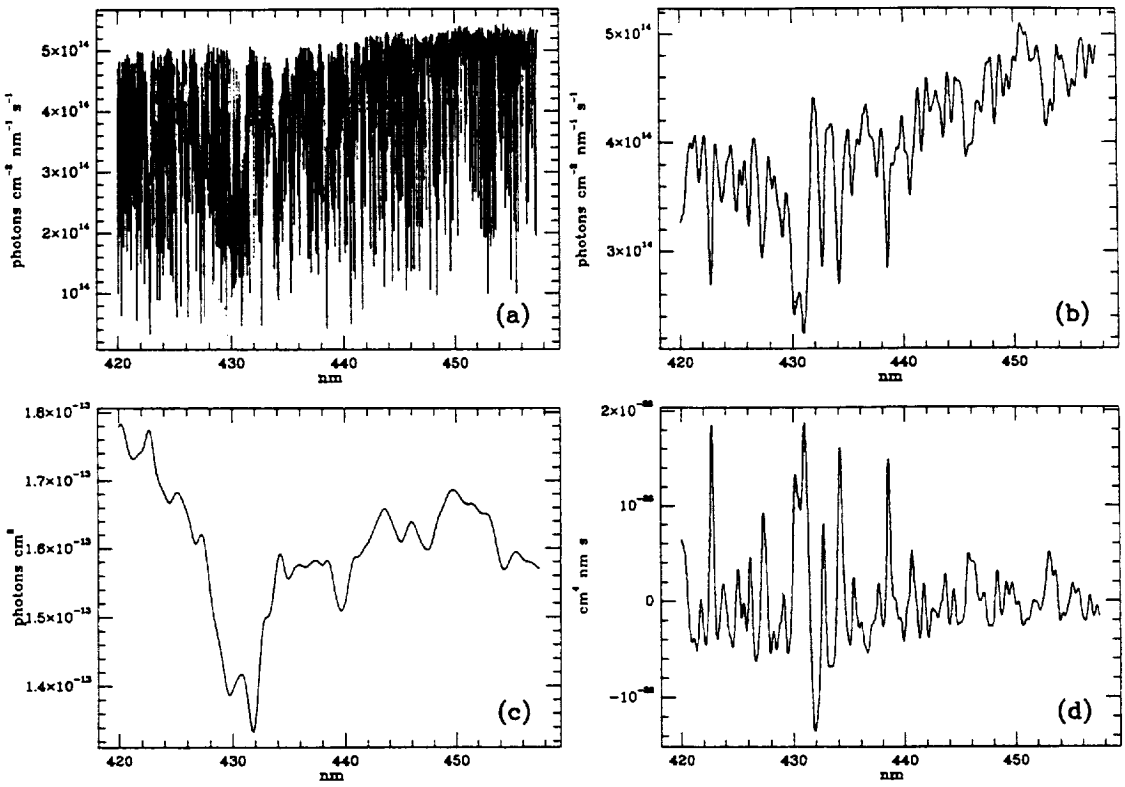

Fig. 2. (a) Sample of the Fraunhofer reference spectrum determined in this study. (b) The same Fraunhofer spectrum, convolved with a Gaussian slit function having a half-width at $1/e$ intensity of 0.212 nm, appropriate to the GOME instrument in this wavelength range. (c) The Fraunhofer spectrum of (b), convolved with the rotational Raman cross sections to create a Ring effect source spectrum. The units are those of cross section × photons, corresponding to the Ring effect scattering source per air molecule at 250 K. (d) The ratio of the Ring effect source spectrum given in (c) to the Fraunhofer spectrum of (b), with a cubic polynomial subtracted off. This spectrum closely corresponds to the Ring effect spectrum used in previous studies for atmospheric spectrum correction, as discussed in the text.

these measurements as the basis for broadening in the present data set.

For O_2, the HITRAN 92 values corresponding to rotational transitions of the same ΔN are initially adopted.[20] When multiple corresponding transitions exist, the pressure-broadening coefficients are averaged. For the two $\Delta N = 4$ transitions, the averages of the values for lines connecting the upper and lower states are taken. The resulting pressure-broadening coefficients are multiplied by 1.185, which is the average result for the ratio of measured air pressure-broadening coefficients for O_2 magnetic dipole rotational transitions to those given in HITRAN (see Ref. 29 for an explanation of this correction). For N_2, pressure-broadening values for the corresponding quadrupole lines of the vibrational fundamental are adopted. Values determined for the pressure-broadening coefficients of both O_2 and N_2 are at 296 K. The temperature dependence should be calculated using the recommended HITRAN 92 coefficient of $n = 0.5$ for N_2 lines[20] and a value of $n = 0.72$ for O_2 lines,[29] through the relation

$$\Gamma_T = \Gamma_{296}\left(\frac{296}{T}\right)^n. \tag{14}$$

4. Solar Reference and Ring Source Spectra

A solar reference spectrum for the range 230–800 nm, at 0.01 nm resolution, has been determined by combining ground-based measurements[30] and balloon measurements.[31] Both spectra were converted to vacuum wavelengths. The balloon data were recalibrated in wavelength using 20 selected atomic reference lines. The spectra were resampled at even 0.01-nm increments, employing a triangular filter of 0.01-nm half-width at half-maximum, and linearly merged over the 300–305-nm wavelength range. The result is a reference spectrum in vacuum wavelengths accurate to better than 0.001 nm above 305 nm and 0.002 nm below 300 nm. This spectrum was created specifically for GOME applications, in particular wavelength calibration studies and calculation of Ring effect contributions to GOME measurements. A sample of this Fraunhofer reference spectrum is given in Fig. 2(a); in Fig. 2(b), it has been convolved with a Gaussian slit function having a half-width at $1/e$ intensity of 0.212 nm, appropriate to the GOME instrument in this wavelength range. The solar spectrum, with GOME slit function, has been convolved with the rotational Raman cross sections described here to create a Ring effect source spectrum for fitting of GOME data. The same wavelength portion of this Ring effect source spectrum is shown in

Fig. 2(c). The units are those of cross sections times photons, corresponding to the Ring effect scattering source per air molecule at 250 K. In Fig. 2(d), the ratio of the Ring effect source spectrum to the Fraunhofer spectrum has been taken and a cubic polynomial, fitted to the region presented in the figure, has been subtracted off, for comparison with differential Ring effect spectra determined in previous studies. Atmospheric Ring spectra have been determined by several groups from polarized spectroscopic measurements of the zenith sky at high solar zenith angles. Measurements at polarizations parallel and perpendicular to the single-scattering plane are combined in similar formulations to obtain effective Ring effect cross sections.[6,7,12] For a single-scattering Rayleigh atmosphere, this procedure could yield the rotational Raman cross sections directly. In practice, because of Mie and multiple Rayleigh scattering, what is determined is the ratio of the rotational Raman spectrum to the solar Fraunhofer spectrum. This can be confirmed by comparing Fig. 2(d) with the results of the above studies. Atmospheric radiative transfer calculations of Ring spectra[7,12] also determine this quantity. It is distinct from the filling in calculated by Joiner *et al.*,[10] who include both the rotational Raman source term and the Cabannes loss term in their calculations. The use of the ratio of rotational Raman to Fraunhofer has proved useful in fitting atmospheric spectra for minor constituent abundances; it is a good approximation to the quantity needed for Ring effect correction in some fitting techniques and measurement geometries. However, its use has limitations because of the distortion of the rotational Raman spectrum and its constant ratio to the Fraunhofer spectrum. The rotational Raman spectrum and Fraunhofer spectrum determined in this study should be more generally applicable to fitting of atmospheric spectra obtained from various measurement geometries, including satellite-based measurements.

5. Conclusions

The complete Rayleigh with rotational Raman-scattering database as described in the previous sections is available from the authors. It includes N_2 and O_2 term values and statistical partitioning (tables including the quantum numbers and term energies for O_2 and N_2 up to states allowing for partitioning to better than 0.01% accuracy and Boltzmann factors with nuclear spin degeneracies g_N); tables giving the King correction factors, values of $\sqrt{\epsilon}$, where $\epsilon = (\gamma/\bar{\alpha})^2$, index of refraction $\bar{\alpha}$, and γ for O_2 and N_2; Placzek–Teller coefficients, with examples of cross sections; pressure-broadening coefficients; the solar reference spectrum derived above; and the convolved solar and rotational Raman spectrum (Ring effect source function cross section calculations). This database is a summary of the best available relevant data that were found in the literature and the calculations performed in this study. One item not included here is the additional broadening that is due to Rayleigh–Brillouin scattering.[4] For the rotational Raman lines, this will provide an extra source of broadening, although the extent of the broadening is within the uncertainties in the pressure broadening for scattering in the troposphere. The effect of Rayleigh–Brillouin scattering for the filling in of the central Cabannes line for narrow Fraunhofer lines might be significant for some satellite measurement conditions and will be a topic for future investigations.

This research was supported by NASA grant NAGW-2541 and by ESA contract 10996/94/NL/CN. We thank the University of Bremen group (M. Vountas, V. V. Rozanov, A. Richter, and J. P. Burrows) and D. Fish for helpful discussions. We are also grateful for the provision of results prior to publication by the Bremen group.

References

1. J. F. Grainger and J. Ring, "Anomalous Fraunhofer line profiles," Nature (London) **193,** 762 (1962).
2. J. Noxon and R. Goody, "Noncoherent scattering of skylight," Izv. Acad. Sci. USSR Atmos. Oceanic Phys. **1,** 163–166 (1965).
3. D. M. Hunten, "Surface albedo and the filling-in of Fraunhofer lines in the day sky," Astrophys. J. **159,** 1107–1110 (1970).
4. G. W. Kattawar, A. T. Young, and T. J. Humphreys, "Inelastic scattering in planetary atmospheres. I. The Ring effect, without aerosols," Astrophys. J. **243,** 1049–1057 (1981).
5. A. T. Young, "Rayleigh scattering," Appl. Opt. **20,** 522–535 (1981).
6. S. Solomon, A. L. Schmeltekopf, and R. W. Sanders, "On the interpretation of zenith sky absorption measurements," J. Geophys. Res. **92,** 8311–8319 (1987).
7. D. J. Fish and R. L. Jones, "Rotational Raman scattering and the Ring effect in zenith-sky spectra," Geophys. Res. Lett. **22,** 811–814 (1995).
8. K. V. Chance, J. P. Burrows, and W. Schneider, "Retrieval and molecule sensitivity studies for the Global Ozone Monitoring Experiment and the SCanning Imaging Absorption spectroMeter for Atmospheric CHartographY," in *Remote Sensing of Atmospheric Chemistry*, J. L. McElroy and R. J. McNeal, eds., Proc. SPIE, **1491,** 151–165 (1991a).
9. J. P. Burrows, K. V. Chance, A. P. H. Goede, R. Guzzi, B. J. Kerridge, C. Muller, D. Perner, U. Platt, J.-P. Pommereau, W. Schneider, R. J. Spurr, and H. van der Woerd, *Global Ozone Monitoring Experiment Interim Science Report*, T. D. Guyenne and C. Readings, eds. Rep. ESA SP-1151, (ESA Publications Division, ESTEC, Noordwijk, The Netherlands, 1993).
10. J. Joiner, P. K. Bhartia, R. P. Cebula, E. Hilsenrath, R. D. McPeters, and H. Park, "Rotational Raman scattering (Ring effect) in satellite backscatter ultraviolet measurements," Appl. Opt. **34,** 4513–4525 (1995).
11. J. Joiner and P. K. Bhartia, "The determination of cloud pressures from rotational Raman scattering in satellite backscatter ultraviolet measurements," J. Geophys. Res. **100,** 23,019–23,026 (1995).
12. Study of the Ring Effect, Final Report, ESA Contract 10996/94/NL/CN (*ESA*, Noordwijk, The Netherlands, 1996).
13. A. Kuze and K. V. Chance, "Analysis of cloud-top height and cloud coverage from satellites using the O_2 A and B bands," J. Geophys. Res. **99,** 14,481–14,491 (1994).
14. M. Bussemer, "Der Ring-effekt: Ursachen und einfluß auf die spektroskopische messung stratosphärischer spurenstoffe," Diplomarbeit, (Universität Heidelberg, Heidelberg, Germany, 1993).

15. C. M. Penney, R. L. St. Peters, and M. Lapp, "Absolute rotational Raman cross sections for N_2, O_2, and CO_2," J. Opt. Soc. Am. **64,** 712–716 (1974).
16. D. R. Bates, "Rayleigh scattering by air," Planet. Space Sci. **32,** 785–790 (1984).
17. L. V. King, "On the complex anisotropic molecule in relation to the dispersion and scattering of light," Proc. R. Soc. London Ser. A **104,** 333–357 (1923).
18. M. Nicolet, "On the molecular scattering in the terrestrial atmosphere: an empirical formula for its calculation in the homosphere," Planet. Space Sci. **32,** 1467–1468 (1984).
19. A. Bucholtz, "Rayleigh-scattering calculations for the terrestrial atmosphere," Appl. Opt. **34,** 2765–2773 (1995).
20. L. S. Rothman, R. R. Gamache, R. H. Tipping, C. P. Rinsland, M. A. H. Smith, D. C. Benner, V. M. Devi, J.-M. Flaud, C. Camy-Peyret, A. Perrin, A. Goldman, S. T. Massie, L. R. Brown, and R. A. Toth, "The HITRAN molecular database editions of 1991 and 1992," J. Quant. Spectrosc. Radiat. Transfer **48,** 469–507 (1992).
21. G. Placzek and E. Teller, "Die rotationnstruktur der Ramanbanden mehratomiger moleküle," Z. Phys. **81,** 209–258 (1933).
22. D. L. Renschler, J. L. Hunt, T. K. McCubbin, Jr., and S. R. Polo, "Triplet structure of the rotational Raman spectrum of oxygen," J. Mol. Spectrosc. **31,** 173–176 (1969).
23. M. Loëte and H. Berger, "High resolution Raman spectroscopy of the fundamental vibrational band of $^{16}O_2$," J. Mol. Spectrosc. **68,** 317–325 (1977).
24. N. H. Rich and D. W. Lepard, "Spin structure in the Raman spectrum of oxygen," J. Mol. Spectrosc. **38,** 549–551 (1971).
25. M. Tinkham and M. W. P. Strandberg, "Theory of the fine structure of the molecular oxygen ground state," Phys. Rev. **97,** 937–951 (1955).
26. K. Altmann, G. Strey, J. G. Hochenbleicher, and J. Brandmüller, "Simulation des intensitätsverlaufs im Raman-spektrum von sauerstoff unter berücksichtigung der spinaufspaltung," Z. Naturforsch. Teil A **27,** 56–64 (1972).
27. M. Mizushima and R. M. Hill, "Microwave spectrum of O_2," Phys. Rev. **93,** 745–748 (1954).
28. K. S. Jammu, G. E. St. John, and H. L. Welsh, "Pressure broadening of the rotational Raman lines of some simple gases," Can. J. Phys. **44,** 797–815 (1966).
29. K. V. Chance, W. A. Traub, K. W. Jucks, and D. G. Johnson, "On the use of O_2 spin-rotation lines for elevation angle calibration of atmospheric thermal emission spectra," Int. J. Infrared Millimeter Waves **12,** 581–588 (1991b).
30. R. L. Kurucz, I. Furenlid, J. Brault, and L. Testerman, *Solar Flux Atlas from 296 to 1300 nm* (National Solar Observatory, Sunspot, New Mexico, 1984) 240 pp.
31. L. A. Hall and G. P. Anderson, "High-resolution solar spectrum between 200 and 3100 Å," J. Geophys. Res. **96,** 12,927–12,931 (1991).